Aerodynamics of a Swept Wing With Simulated Scalloped Ice at Low Reynolds Number

Navdeep Sandhu

A thesis submitted in partial fulfillment of the requirements for the degree of

Master of Science in Aeronautics & Astronautics

University of Washington

2018

Reading Committee:

Michael B. Bragg, Chair

Christopher Lum

Program Authorized to Offer Degree:
William E. Boeing Department of Aeronautics and Astronautics

University of Washington

Abstract

Aerodynamics of a Swept Wing With Simulated Scalloped Ice at Low Reynolds Number

Navdeep Sandhu

Chair of the Supervisory Committee:
Frank & Julie Jungers Dean of Engineering, Michael B. Bragg
William E. Boeing Department of Aeronautics & Astronautics, University of Washington

This thesis studied the aerodynamic effects of a single high-fidelity scalloped ice accretion simulation and a low-fidelity simulation of the same shape. These data were compared to the aerodynamics of a clean 8.9% scale CRM65 semispan wing model at a Reynolds number of 1.6×10^6. The clean wing experienced an aggressive, tip-first stall and showed a small, strong leading-edge vortex at lower angles-of-attack while the iced cases showed larger, seemingly weaker leading-edge vortices at similar angles. The size of these vortices is larger for the low-fidelity ice shape. The stall pattern for the iced cases was also tip-first, but more gradual than the clean wing. The high-fidelity ice shape produced streamwise flow features over the upper surface of the wing likely due, in part, to flow moving through gaps that exist in the ice shape geometry that disrupted the formation of the leading-edge vortices. These features are thought to change the aerodynamics of the wing by impacting leading-edge vortex formation and delaying flow separation. These gaps do not exist in the low-fidelity shape, where leading-edge vortices are larger, are apparent at lower angles-of-attack, and flow separation occurs earlier over the wing. The low-fidelity scallop ice shape was non-conservative in its aerodynamic performance penalties compared to the full high-fidelity case.

TABLE OF CONTENTS

LIST OF FIGURES

LIST OF TABLES

NOMENCLATURE

α	Angle of attack
α_{stall}	Angle of attack at stall
δ	Boundary layer thickness
Λ	Wing sweep angle
C_D	Drag coefficient
C_L	Lift coefficient
C_m	Pitching moment coefficient
C_p	Surface pressure coefficient
$C_{L,max}$	Maximum lift coefficient
$C_{L,stall}$	Lift coefficient at stall
M_{cr}	Critical Mach number
Re_m	Reynolds number per meter
Re_{ft}	Reynolds number per foot
M	Mach number
Re	Reynolds number
b	Semispan
c	Local chord
CAD	Computer-aided design
CRM	Common research model
CRM65	65%-scale common research model

FAA	Federal Aviation Administration
IRT	Icing research tunnel
NASA	National Aeronautics and Space Administration
ONERA	Office National d'Etudes et de Recherches Aérospatiales
q	Dynamic pressure
x	Streamwise distance
y	Spanwise distance
z	Water line distance

ACKNOWLEDGMENTS

Several people must be acknowledged for their effort and support as I conducted this research. Foremost, my advisor, Dr. Michael Bragg, must be thanked for all that he has done. Dr. Bragg has been an amazing mentor and I have learned an immense amount from him. Dr. Christopher Lum and Dr. Reza Soltani both did the same. Dr. Lum brought me into this research group, thinking I would be a good fit, and I am very happy he did. He has also supported my research, helping me as I navigated my new research and my first year as a graduate student. Dr. Soltani worked very closely with me over the second year of my degree on this very research. His ideas and insight into the problems we faced were paramount to my learning.

I must also thank Kevin Ho, the lab manager for the Aircraft Icing & Aerodynamics Research Group at the University of Washington. Together, we worked on the fast-response five-hole probe, data reduction, and other design-and-build projects and I would not be where I am without his help. Mahda Soltani is also recognized and thanked for her contribution to data reduction.

This work was supported by the FAA, and I must thank all of our collaborators at the FAA, Boeing, NASA, and the University of Illinois Urbana-Champaign.

To all my friends in the program and out of the program who supported me through the stressful and gleeful times of my education, I sincerely thank you and hope I was able to do the same for you. I would also like to thank my girlfriend, Kathryn, for her love and support. Finally,I want to thank my adoring family for encouraging me and allowing me to flourish as I move onto the next steps of my life.

Chapter 1
INTRODUCTION

Modern research efforts in the field of aircraft icing has, among its many goals, an aim of simplifying certification of these vehicles by reducing the amount of costly flight testing needed to prove airworthiness. To that end, the study of iced leading-edge swept wings has focused heavily on the aerodynamic performance degradation caused by the ice formation when compared to a similar, non-iced wing. These studies are important to our understanding of iced wings, but they do not provide a complete picture of the flow phenomena associated with iced swept wings. Qualitative studies can provide an understanding of the underlying aerodynamic phenomena caused by leading-edge ice. Previous published research has mainly focused on 2D aerodynamic effects of ice accretion on airfoils and straight wings. Bragg et. al [1] reviewed the extensive 2D aerodynamic effects of ice accretion on airfoils and classified ice accretions by their aerodynamic effect. In this study, particularly in regards to the horn ice described by Bragg, it is shown that iced airfoils are dominated by large separation bubbles that are formed behind the ice itself. The bubble alters the pressure distribution over the upper surface of the wing, causing performance degradation. Lynch and Khodadoust [2] showed the effect of airfoil thickness on a 2D iced straight wing, concluding that adverse ice accretion effects are larger for thicker wings. They also concluded that multi-element wings incur lower penalties with ice than single-element wings.

More complex wing geometry with leading-edge ice have been studied well. Broeren et al [3] used a 72 in. span NACA 23012 at Re ranging from 4.5 million to 16 million and M ranging from 0.10 to 0.28. They found that, along with large performance penalties, leading-edge ice changes the stall type experienced by a wing. That is, a clean wing that has an abrupt

leading-edge stall type can experience characteristics of a more gradual trailing-edge stall. Papadakis et al [4, 5] showed that a finite swept wing with leading-edge glaze ice experienced a reduction in lift coefficient of 11.5% to almost 94% and an increase in drag of anywhere from 133% to over 3500%, depending on the specific configuration tested.

Some analysis of the underlying flow physics associated with leading-edge ice on a swept wing has been done. Kerho et al [6] showed using LDV flowfield measurements that phenomena generally associated with 3D clean wings, such as the development of leading-edge vortices, are also present with leading-edge ice configurations of the same 3D wing. Recent work by Broeren et al [7, 8] and Diebold et al [9] have shown the evolution of flowfield features for a small-scale version of the NASA Common Research Model (CRM) wing with leading-edge ice attached. These features include the development of the leading-edge vortex and the progression of separation over the wing.

Previous studies have focused heavily on the aerodynamic performance degradation associated with leading-edge ice. Research on more complex geometries has generally been limited to very low *Re*, or has not explored in-depth the analysis of flowfield phenomena occurring with a swept-wing with leading-edge ice. The research presented in this thesis intends to improve the understanding of the underlying physics associated swept-wing icing cases. This will be accomplished by analyzing data from recent wind tunnel tests for a clean swept-wing, a swept-wing with a high-fidelity simulated scalloped ice shape, and a low-fidelity simulated scalloped ice shape.

Background information and a literature review of clean and iced swept-wing aerodynamics will be presented in Chapter 2. This will also include background information into the generation of the simulated scalloped ice shapes. This will be followed by an overview of the swept-wing model, the wind tunnel facility at Wichita State University (WSU), and the various data types used for data collection. Results will then be presented for the clean leading-edge case, followed by the low-fidelity simulated scalloped ice shape, and then finally the high-fidelity shape.

Chapter 2
BACKGROUND

To understand the effect of leading-edge ice on a swept wing, the aerodynamic phenomena associated with a clean leading-edge swept-wing must be examined. This has been examined in some detail in previous studies. Wings are swept in an effort to allow for flight at higher M compared to straight wings. The classic limit for subsonic flight is M_{cr}, which is the freestream Mach number such that the peak M over the upper surface of the wing is 1. Wing sweep causes the flow to "see" a thinner local airfoil, as the effective chord of a given airfoil section on the wing is longer than the same wing without sweep [10]. Of course, this change in geometry has other effects. Those effects and their consequences will be explored in this chapter, for both clean and iced wings, including some background on ice shape generation.

2.1 Clean Swept-Wing Aerodynamics

Swept wings have been studied in detail for some time. One of the earlier studies was conducted by Furlong and Mchugh [11]. They describe the characteristics of a swept-wing at high Re, $Re = 6 \times 10^6$, observing several things for a wing with $\Lambda = 45°$. A pronounced leading-edge separation bubble forms over the wing. Though this can occur on straight wings as well, when coupled with a spanwise pressure gradient due to spanwise flow over the wing, spanwise vortical flow near the leading edge results. They found that this vortex effects the pressure distribution over the chord of the wing, decreasing the leading-edge pressure and shifting the center of pressure toward the trailing edge. The formation of this leading-edge vortex is also tied to the leading-edge radius of the local airfoil section. For a thin wing, the amount of sweep required to observe vortex flow is reduced compared to a thicker wing. Though this leading-edge vortex results from leading-edge separation, Furlong and Mchugh

also observed that both leading-edge and trailing-edge separation characteristics can be seen on the same wing. These separation categories are linked to stall types of the same name, that is leading-edge stall (characterized by sharp separation of flow over a majority of the chord of the wing) or trailing-edge stall (characterized by separation that occurs gradually from the trailing edge to the leading edge as α increases). There is a third type of stall described by McCullogh and Gault [12], called thin-airfoil stall, which is characterized by flow separation occurring at the leading-edge of an airfoil section, followed by reattachment that occurs further downstream as α increases. This type of stall incorporates characteristics from both other types, and as the name implies, has been observed for thin airfoils. According to Harper and Maki [13], leading-edge stall and trailing-edge stall are observed separately in the case of an uncambered airfoil. For some moderate thickness and camber, an airfoil will likely experience stall of the thin-airfoil type.

The phenomena seen for swept-wings are coupled with other factors, such as Re or geometric considerations like airfoil thickness. Thus, it becomes necessary to isolate some of thse effects. Poll [14] conducted experiments to determine the effect of leading-edge shape and sweep angle separately on the formation of spiral vortex flow for several Re_m between 0.9×10^6 per meter and 2.7×10^6 per meter. Poll focused on the phenomena occurring, as the primary diagnostic for his experiments was surface oil-flow visualization. At low sweep angles, Poll found no spiral vortex flow. For $\Lambda > 15°$, oil flows indicated the existence of spiral vortex flows. However, these flows changed based on Re, leading-edge radius, and Λ. Poll found three general mechanisms for the formation of spiral vortex flows over a swept wing. They are

1. A full-span vortex can form as the shear layer rolls up, leaving the surface at a location called the primary separation line. This flow looks similar to those of thin delta wings at finite α.
2. A vortex that only forms over part of the wing span can form when the shear layer from the primary separation reattaches, forming a short bubble on the inboard of the wing. The shear layer on the outboard of the wing, which experiences a higher load

than the inboard, does not reattach and instead rolls up to form the vortex.

3. A vortex that only forms over part of the wing span can form when the boundary layer downstream of a separation bubble separates at a location called the secondary separation line. The resulting shear layer rolls up and forms the vortex.

A figure showing oil flow contours and primary, secondary, and the attachment line is shown in Fig. 2.1. The formation of these vortex flows is an important concept to clean swept wings.

Something to note is that swept wings show a tendency for tip stall. This is observed by Furlong and Mchugh [11] as well as Harper and Maki [13]. Spanwise flow from root to tip, along with high loading on the outboard sections, cause the tip to stall prior to the inboard sections of the wing. Stalling in this manner will cause the center of pressure of the wing to shift toward the leading-edge. This is destabilizing, as it would cause pitching moment to increase. Geometry changes can be made to help alleviate these effects. An example of such a change is adding twist to the wing to alter the local α such that the root stalls prior to the tip.

Harper and Maki [13] also review some of the effects of Re on swept wings. They note that the spanwise flow of boundary layer fluid from root to tip creates a 'drain' effect from the inboard sections. For low Re, there is a tendency for an airfoil section to experience trailing-edge stall. This effect is overcome by the spanwise flow of the boundary layer. Thus, in a sense, this boundary-layer drainage is effectively increasing Re for the inboard sections of the wing. There is little effect of Re on stalled wing regions in terms of lift. The outboard portion of the wing stalls prior to the inboard. Because the maximum lift generated by a swept-wing will likely occur after the tip region stalls, it can be said that some of these Re differences disappear after the tip region stalls. Poll [14] notes that Re alone cannot determine what sort of vortex flow will be seen over a wing, but transition, turbulence levels, entrainment, and more affect the type of vortex flow that will be seen. Poll also observed that the larger the leading-edge radius of a wing, the greater that wing's dependence upon Re for determining the "critical" α. This critical freestream incidence angle determines at

which point, for a given Λ and other freestream conditions, a leading-edge vortex will appear on a wing.

In summary, clean swept-wing aerodynamics are characterized by several distinct flowfield features, based on the geometry of the wing such as leading-edge radius, sweep angle, and wing thickness. A separation bubble can form at the leading edge of the wing, which can form a leading-edge vortex when combined with a spanwise pressure gradient. For this to occur, the wing should have a moderate sweep angle. Several mechanisms exist for spiral vortex flow formation over the upper surface of a swept wing, each leaving a distinct footprint when using oil flow visualization techniques. Swept wings exhibit stall characteristics in line with thin airfoils, exhibiting some qualities from both leading- and trailing-edge stall types. They also have a tendency to stall tip-first due to spanwise flow and high loading conditions on the outboard of the wing. The effect of *Re* seems to be higher on the outboard of the wing, though *Re* alone will not be able to predict the flow over a swept wing.

2.2 Iced Straight-Wing and Swept-Wing Aerodynamics

Leading-edge ice is a variable that further complicates the aerodynamics of a swept wing. Some work has been done in this area. However, due to the complex nature of swept-wing aerodynamics, some of these effects are more well-understood for straight wings. Results are presented for both cases for leading-edge ice geometry.

2.2.1 Classification of Leading-Edge Ice

Prior to studying the effect of ice on swept wings, the different classification of leading-edge ice shapes will be briefly reviewed. In recent years, the classification of ice accretions on a swept wing has been broken down into four main categories: ice roughness, horn ice, streamwise ice, and spanwise-ridge ice [1, 7]. These divisions are based upon the distinct flowfield features produced. To this point, glaze ice has been mentioned in previous studies. This sort of leading-edge ice is marked by horns that protrude into the flow (see Fig. 2.3). Thus, there is an association between glaze ice and horn ice. Bragg et. al. [1] and Broeren et.

al. [7] define the four categories as follows:

- **Ice roughness** is the first portion of ice to accrete on a leading edge. The scale of boundary-layer separation in these icing situations is of the same order as the size of the roughness itself.
- **Horn ice** is large, protruding ice from the leading edge. Flow separation from the horns is seen in the flowfield, with this separation leading aiding in the formation of a spanwise-running leading-edge vortex for a swept wing. There are several stages of this sort of ice, sub-categorized as no-scallop, incomplete scallop, and complete scallop shapes. The data set that exists for the latter is limited, and the flowfield highly complex due to the highly three-dimensional nature of the ice.
- **Streamwise ice** forms in a manner that conforms to the leading-edge of a wing, though it may form small horn-like structures that extend in the flow direction. Some data has shown that this type of ice may increase maximum lift for a given configuration, though this is not expected to be the norm, and further study is required.
- **Spanwise-ridge ice** is associated with icing formed in the Supercooled Large Droplet (SLD) icing conditions with ice protection system operation. For this ice shape, the leading-edge is generally free of ice, and an ice ridge forms from 10-15% chord downstream.

Because it is more well-defined, and has been studied in more detail in the history of icing, the horn ice shape will be focused on for the scope of this exploration.

2.2.2 Aerodynamic Performance Degradation Due To Leading-Edge Ice Simulations

Though this thesis will not focus on aerodynamic performance degradation caused by leading-edge ice simulations, it is still prudent to review these results from previous studies.

Papadakis et. al. [4] studied the effect of ice accretions on the aerodynamic performance of a swept finite wing. The results of the complete scallop glaze ice compared to the clean wing will be summarized here. The wing tested was a 22% scale model of the 65%-semispan (35% to 100%) segment of a large business jet wing, with a constant GLC-305 wing section in the

streamwise direction. The airfoil section had a thickness-to-chord ratio of 0.087 at 38% local chord, $\Lambda = 28°$ leading-edge sweep, $\Lambda = 15.6°$ trailing-edge sweep, a 60-in. semispan, 7.35 ft^2 area, an aspect ratio of 6.80 (defined in terms of both left and right wing), a taper ratio of 0.4, and washout of $-4°$ from root to tip. The mean aerodynamic chord (MAC) was 1.56 ft, the root chord was 2.1 ft., and the tip chord was 0.84 ft. The clean wing was studied along with several glaze ice accretions, both ice accretion castings and simulated ice shapes generated via computational analysis, with horn heights ranging from 0.3 in. to 3 in. for these shapes. Ice simulations generated in via wind tunnel accretion are labeled beginning with the designation "IRT-", while other designations are used for smooth computationally-generated ice and roughness shapes. The ice shape castings are summarized in Fig. 2.5. Three-dimensional simulated ice shapes were generated with LEWICE 2.0 ice accretion code (further information for this code can be found in Wright [15], who wrote the user's manual for this code). To generate the simulated shapes, the following steps were taken:

1. Five spanwise stations were selected at which streamwise wing sections were taken (including both the root and tip of the wing). Four additional sections were taken at the same spanwise locations except for the root. These sections were taken normal to the leading edge of the wing.
2. 3D Navier-Stokes computations were performed on the clean wing to obtain the wing flowfield for $\alpha = 4°$ and $\alpha = 6°$ (matching with experimental data) and accounting for tunnel wall effects, showed good correlation to experimental data.
3. Pressure distributions were obtained for the 4 normal airfoil sections and the streamwise root section described in step 1.
4. 2D ice accretion analyses were performed using LEWICE 2.0 computer code. The angle of attack in LEWICE 2.0 was adjusted slightly such that the pressure field around the airfoil sections matched that of the Navier-Stokes analysis described in step 2.
5. The ice sections generated in step 4 were imported into a CAD software package, where spline surfaces and plane surfaces connected the sections to generated 3D LEWICE ice shapes.

Cross-sections at 3 spanwise stations for the IRT-CS22 and the corresponding smooth shape generated by LEWICE are shown in Fig. 2.6. It is seen that though care was taken to match conditions for the experimental and computed ice shapes, there is a large difference in resulting cross-sections. Tests were performed at $Re = 1.8 \times 10^6$, based on MAC. The clean wing stalled for $C_L = 0.87$ and $\alpha = 13.8°$, while C_D for the wing varied from 0.0063 at $\alpha = 1°$ to 0.15 at stall. A leading-edge vortex formed, causing the wing to undergo leading-edge stall that stretched from midspan to the tip of the wing, and then to the root as α increased.

General results for the six glaze ice accretions compared to the clean wing show that $C_{L,stall}$ was reduced by 11% to 93.6%, depending on the shape, while α at stall was reduced from 8% to 56.5% (effectively cutting stall angle in half). Minimum C_D was increased from 200% to over 3500%. Of note is the IRT-CS22 shape (ICE 5 in Fig. 2.5) as this case represents a highly-3D, severe icing condition for this exploration. Papadakis notes that the gaps between the scallops likely increased lift degradation, as there was probably flow leakage from the gaps. Stagnation-region flow leaking into the low-pressure flow region downstream of the ice shape would increase the pressure over the upper surface of the wing, harming aerodynamic performance.

The effect of the horn geometry itself on the aerodynamics was examined by Busch et. al. [16]. Note that this experiment was done with straight wings. Here, a casting of an ice accretion was tested against multiple "2-D smooth simulation" shapes with variable geometry. These 2D smooth shapes, as referred to by Busch, were created to model a horn-ice accretion on either a NACA 0012 or NACA 23012. Both models had a chord of 18 in., a span of 33.563 in., and a removable leading edge to place the simulated ice on the front of the wing. All testing was done for $Re = 1.8 \times 10^6$ and $M = 0.18$. The simulated ice shapes for the NACA 23012 model are shown in Fig. 2.7 and Fig. 2.8. The study by Busch et. al. is an exploration into the fidelity of ice shape simulations and their effectiveness in recreating the aerodynamics of an original ice accretion. The 2D smooth simulation and the nonperiodic single geometric simulation, Fig. 2.8b and Fig. 2.8d, were able to model the $C_{L,max}$ of the casting to within 1%, while the simple geometric simulation with periodic variation was able to model $C_{L,max}$

of the casting to within 2%. However, there was significant spanwise variation observed in the flowfield for the casting shape that was not observed in the 2D smooth simulation or the simple geometric simulation, but was observed in the simple geometric, nonperiodic simulation, which almost completely recreated the flowfield of the casting. It should be emphasized that Busch's test and analysis did not take place with a swept wing.

These studies show a clear deterimental effect of leading-edge ice on both straight and swept wings. They then attempt to rectify these degradations with observed flow phenomena. However, these studies do not address the increased complexities for a more complicated wing geometry, such as a swept wing with washout, that would be more indicitive of a commercially used wing model. Thus, an extension to these studies including a similar analysis technique but with more complex wing geometry is required, and is presented as a part of this thesis.

2.2.3 Roughness Effects

The roughness of ice shapes has an effect on the resulting wing aerodynamics. Thus, in addition to studying the effect of geometric variation of ice shapes, it is necessary to quantify and document the effect of small roughness elements and compare to smooth cases of the same shape. Again, consider the study done by Papadakis [4]. The IRT-CS22 shape had several features not present in the smooth shape, namely the roughness and complex scallop features. To study the effect of roughness, 36-grit size (average height of 0.0211 in.) was added to the smooth LEWICE2.0 shape. Compared to the clean wing, the IRT-CS22 shape, the smooth shape formed with cross-sections normal to the leading-edge (referred to by Papadakis as the LS-CS22N), and the same smooth shape with roughness (LR-CS22N) showed lift degradations of 93.6%, 44%, and 53%, respectively. The roughness shape had a considerably higher effect on the clean-wing aerodynamics than the smooth shape. The increase in the minimum C_D for each shape was 3533%, 2033%, and 2933%, while the reduction in α at stall was 57%, 2%, and 17%, respectively. The grit roughness shape compared better to the IRT-CS22 shape than the smooth shape, however neither compared particularly well. The other icing cases studied by Papadakis showed relatively good comparison between the three cases. However,

for the IRT-CS22 case presented here, that is not true. This case was chosen as it shows the imperfect nature of fidelity and grit studies for simulated ice testing.

Though Papadakis shows the numerical effect of roughness, it is research compiled by Bragg et. al. [1] that delves into why these effects occur. Here, Bragg goes into the underlying flow physics that describe roughness on a leading-edge ice shape for a 2D airfoil. Consider a single roughness element on a leading-edge ice shape in some flow. This roughness element is inherently 3D, and thus will produce 3D separation features. A view of resulting 3D flowfield for an isolated roughness element is shown in Fig. 2.9. The system of interacting vortices is highly complex. For roughness elements of height k that are larger than the boundary layer thickness δ, each roughness element acts like an isolated flow obstruction. Thus, roughness must be characterized by its height, the density of the roughness, and its location on the surface. Brumby [17] studied the effect of location of roughness. Some of those results are given in Fig. 2.10. It is seen that roughness near the leading edge has the highest effect for surface roughness location. However, Bragg argues that this is dependent upon roughness size and airfoil geometry. Bragg cites Bowden [18], who shows that surface roughness has the largest effect when placed in the region of highest velocity (or minimum pressure), explaining why surface roughness on the leading edge of a wing has a larger effect than other locations. In terms of the aerodynamic effect of roughness, Bragg [1] states that roughness affects boundary-layer transition and separation due to its affect on the shear force and pressure. These roughness elements can act as boundary-layer trips, causing early onset of a turbulent boundary layer when compared to a smooth airfoil. This would promote trailing-edge separation and increase pressure drag, thus reducing lift and increasing drag. This result is not inherently general, as it depends on the airfoil geometry, which is even further complicated when extended into 3D. There are aerodynamic complexities added by extending roughness analysis to 3D, swept-wing geometries and leading-edge ice that changes with span. Thus, the effects of roughness are best derived experimentally as differet icing and model combinations will show different results.

2.2.4 Re and M Effects

The effect of Re and M are not well-understood, as all experiments have limits as to what tests can be performed, whether the limit be time, financial burden, testing facility, or likely some combination of all three. However, some analysis of these effects has been done. Diebold et. al. [9] used a 2.1 ft. semispan scale NASA Common Research Model (CRM) wing. This wing had a leading-edge sweep of 35°, an aspect ratio of 8.3, a MAC of 0.5167 ft., and a taper ratio of 0.296. In this study, the goal was to use a simple ice shape that had a substantial impact on the aerodynamics, where the accretion of the shape was well-documented along with the ice shape simulation generation process. These processes are given given by Diebold. Three cross-sections for the resulting ice shape are given in Fig. 2.12. The tests were run for $Re = 0.3 \times 10^6$, $Re = 0.6 \times 10^6$, and $Re = 0.78 \times 10^6$. The results from this study show that the clean wing exhibited classic swept-wing effects, including tip-first stall and the formation of a small leading-edge vortex. With the ice shape attached, the wing exhibited similar phenomena, but the leading-edge vortex grew to a size comparable to the local chord before being swept off of the wing near midspan. Both the clean and iced wing experienced a gentle stalling process. For the clean wing, as Re doubled from 0.3×10^6 to 0.6×10^6, α_{stall} and $C_{L,stall}$ were increased by 12.2% and 11.4%, respectively. This trend continued as Re increased to 0.78×10^6, as both values increased by 5.6% and 5.1%. With the ice shape attached, this effect decreased. The iced wing showed an increase of $C_{L,stall}$ by 5.6% for an increase of Re from 0.3×10^6 to 0.6×10^6, and only a 1.7% increase for an increase of Re from 0.6×10^6 to 0.78×10^6. Diebold [9] and Bragg [1] observe that this decrease in effect is from the ice shape fixing the separation point. However, this change is observed for very low Re. The work done by Lee [19] extends the range of Re, but was completed for 2D airfoils. Lee's study compared the Re effects for the NLF 0414 airfoil at $Re = 0.5 \times 10^6$, 1.0×10^6, and 1.8×10^6 for both a clean airfoil and simulated leading-edge glaze ice accretion. Lee found that the clean airfoil experienced an increase in $C_{L,max}$ of 20% for an increase of Re from 0.5×10^6 to 1.8×10^6. With the leading-edge glaze ice simulation, this change was

reduced to 3% and occurred between $Re = 0.5 \times 10^6$ and 1.0×10^6, with $C_{L,max}$ for $Re = 1.8 \times 10^6$ showing no variation from the lowest *Re*. This decrease in sensitivity was seen for C_D and C_m as well. Note that this exploration, along with the exploration done by Diebold [9] also does not account for *M*, as the tunnel used was an atmospheric type and thus *M* could not be held constant.

Bragg [1] explored the independent effect of *Re* and *M* on a leading-edge glaze ice accretion. Consistent with previous studies, Bragg shows that the effect of *Re* is relatively small with leading-edge ice. More interesting, however, is that there is an effect of *M*. The general tendency of increasing *M* on an iced airfoil is to decrease lift and increase drag. Bragg states that for an increase of *M* from 0.12 to 0.28, $C_{L,max}$ can decrease as much as 0.2 for an iced airfoil. The C_p distribution and streamline reattachment for a 2D airfoil with a leading-edge glaze ice accreiton is shown in Fig. 2.2. The suction peak on the upper surface of the wing decreases with increasing *M* but not increasing *Re*, while the separation bubble behind the ice accretion increases size with increasing *M*, with a much smaller change with increasing *Re*. Broeren [20] used a NACA 23012 airfoil with an iced leading-edge and found similar results for both the *Re* and *M* effects. However, Broeren also concludes that compared to the aerodynamic degradation caused by the existence of the ice shape, the changes with *Re* and *M* are small. There also seems to be a critical *Re* (dependent upon size of ice accretion or roughness elements) such that increasing *Re* beyond this point has very little effect on the aerodynamic performance of iced airfoils, leading to the conclusion that small-scale iced can be applied carefully to higher *Re*. [1, 20]

2.2.5 Comparison Between 2D and 3D Results

Bragg et. al. [21] used a 21 in. chord NACA 0012 airfoil with a removable leading-edge to study the effect of simulated leading-edge ice in 2D. The model had interchangeable tip and root sections to allow for 30° sweep for the wing. The 3D model was a semispan wing with the same NACA 0012 airfoil, a span of 37.5 in., and chord of 15 in. The swept wing had $\Lambda = 30°$. All data were taken for $Re = 1.2 \times 10^6$. The ice studied was glaze ice, which is

characterized by ”horns” that protrude from the leading-edge of the wing. Bragg et. al. used the NASA Icing Research Tunnel (IRT) to accrete the ice on the model at given freestream conditions, and then simulated this ice shape for repeatable experiments. Figure 2.3 shows a cross-section of both the IRT-measured glaze ice and the corresponding simulated ice shape. Both 2D and 3D results are considered. For $\alpha = 4°$, flow separation on the upper surface was observed using split hot-film in the 2D model from a region of x/c = -0.02 (over the ice shape itself) to x/c = 0.16. The boundary layer traces generated by the split hot-film are shown in Fig. 2.4. They also noticed a separation bubble in a region from the leading-edge to x/c = 0.08. In this region, the pressure taps showed nearly-constant pressure. This bubble greatly alters the aerodynamics of the 2D wing. In 3D, both straight-wing and swept-wing configurations were tested. In the straight-wing case, a spanwise separation bubble is seen near the leading edge. However, this seems to be the only 3D effect seen. For the swept-wing case, a leading-edge vortex forms due to the influence of spanwise flow. As α increases, the size of the vortex grows. This flow, Bragg et. al. concludes, is highly three-dimensional. Comparison between 2D airfoils and 3D swept-wings is difficult given the large aerodynamic differences. The aerodynamics of 2D iced airfoils is well-documented both numerically and with regard to physical flow phenomena. The data is more limited for 3D wings with ice accretions, and moreso for swept wings.

The research conducted in this thesis takes this a step further and analyzes a swept wing with twist. This configuration is closer to a commercially used geometry than previous studies and combines the aerodynamic intricacies of the leading-edge ice accretion simulations with the natural complexities of a swept wing with washout.

2.3 Ice Shape Generation

Some overview of the generation of full-span leading-edge ice shapes was provided in Chapter 2.2.3. However, this methodology has been updated as the software and technology available has become more advanced and the wing geometry has become more complex. As this complex wing geometry is the focus of this research, the generation of the corresponding

full-span leading-edge ice shapes will be provided here. The process of generating these ice shapes for a swept-wing with taper is complicated due to the spanwise variation of the geometry of the wing. Camello [22, 23] provides a summary of the process used to generate these leading-edge ice shapes. Using the NASA IRT facility, ice was accreted on inboard (y/b = 0.2), midspan (y/b = 0.64), and outboard (y/b = 0.83) section models of the 65% scale Common Research Model (CRM65) wing first described in Chapter 2.2.4. These models had full-scale leading-edge geometry to reduce the amount of scaling required [24] on the resulting ice shapes, but had a redesigned aft section with truncated chords. The design of this hybrid wing is given in more detail by Fujiwara [25]. The three sections of the model and the airfoils at these sections are shown in Fig. 2.13 and Fig. 2.14. After ice was accreted on these models, it was laser scanned such that the geometry could be digitized in a point cloud. This laser scanning method was developed by Lee et. al. [26]. This point cloud was used to create a water-tight mesh that retained the complex icing geometry of the original ice accretion [23]. The creation of a high-fidelity, full-span leading-edge ice shape involved the use of the software program Geomagic Studio and its weighted average function. This function uses multiple copies of a given shape and combines it with some amount of copies of another shape. In the context of creating full-span leading-edge ice shapes, this becomes useful as the ice accretions gathered were only for small sections at three spanwise stations. Figure 2.15 shows a visualization for this interpolation process. Note that the weighted averaging function changes the weights based on the location of the interpolated ice. For example, Interpolated Ice 1 in Fig. 2.15b was created using 5 copies of the original midspan ice accretion and 1 copy of the original outboard ice accretion. This process is repeated, using Interpolated Ice 1 and the outboard ice accretion in the same 5:1 ratio to form Interpolated Ice 2. This process was repeated until a full-span leading-edge ice shape was created. To extrapolate to the wing root and the wing tip form the inboard and outboard ice accretions, respectively, LEWICE3D code was used to generate ice accretion point cloud data at the root and tip of the CRM65, as experimental data did not exist for these areas.

Low-fidelity ice shapes are ones that do not retain the complex, 3D features of a high-

fidelity shape, but do maintain the general form of the original ice shape. These low-fidelity models are easier to rapid prototype and work with, reducing time spent in creating ice shapes and cost. Thus, it is beneficial to use them, however experimentation had to be done to examine if these low-fidelity shapes created similar flowfields to their high-fidelity counterparts. These low-fidelity shapes are referred to as "2D smooth" shapes by Camello, but in this thesis, will be referred to as "3D smooth" ice shapes. To create these shapes, Camello [22] took groups of three 2D cuts at various points along the span of the high-fidelity shape to capture the variation of the high-fidelity ice shape. The cuts were space 1 in. apart in each grouping of three. The outer contour of one group of cuts was taken and formed a local, smooth section. Using approximately 30 of these smoothed contours, a lofted, low-fidelity ice shape was created. An example of these cuts and their resulting smooth contour is shown in Fig. 2.16, while a small portion of a high-fidelity horn ice shape is shown compared to its corresponding low-fidelity shape in Fig. 2.17.

2.4 Current Work

One of the main research efforts in the field during the last decade has been led by NASA, the FAA, ONERA, and their academic partners using the 8.9% scale CRM model as a base for low *Re* testing of the aerodynamic effects of leading-edge ice on a finite swept-wing. Woodard [27] provides a comprehensive review of this low *Re* research effort up to the end of 2017. The tests performed as part of this effort, which provided the data used in this study as well, were done at the Walter H. Beech Memorial Wind Tunnel at Wichita State University (WSU). Force balance, surface pressure, and mini-tuft flow visualization data were collected for each of the three *Re* and *M* combinations on all the model and ice shape configurations. This thesis will focus on results from this low *Re* campaign in an effort to extend the collective knowledge on the effect of a leading-edge scalloped ice shape simulation and its low-fidelity counterparts on the aerodynamics of a scale CRM wing. This will be done by focusing on qualitative results moreso than quantitative results in an effort to bridge the gap between the underlying flow physics experimental aerodynamic performance data.

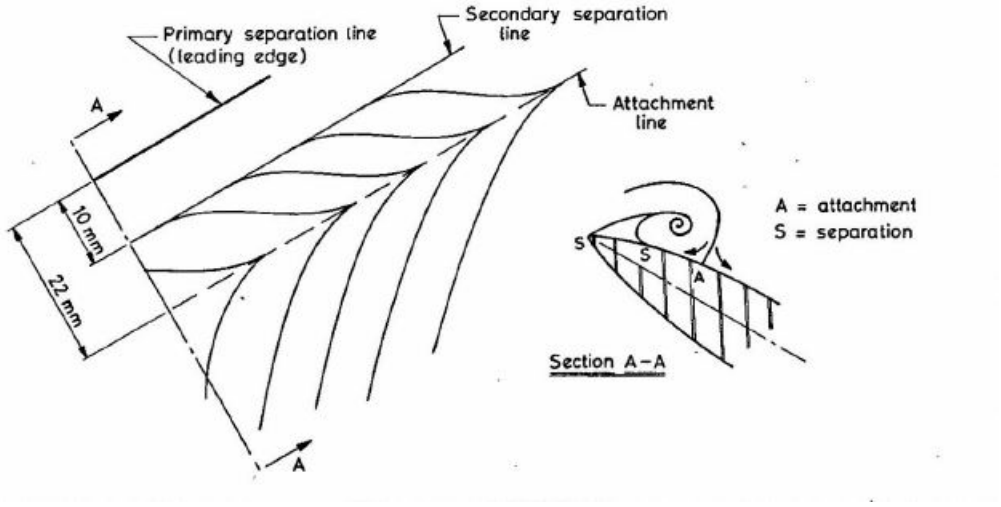

Figure 2.1: Contours of oil flow showing flow close to a sharp leading edge for a wing with $\Lambda = 30°$, $\alpha = 4°$, and $Re = 1.7 \times 10^6$. Adapted from Poll [14].

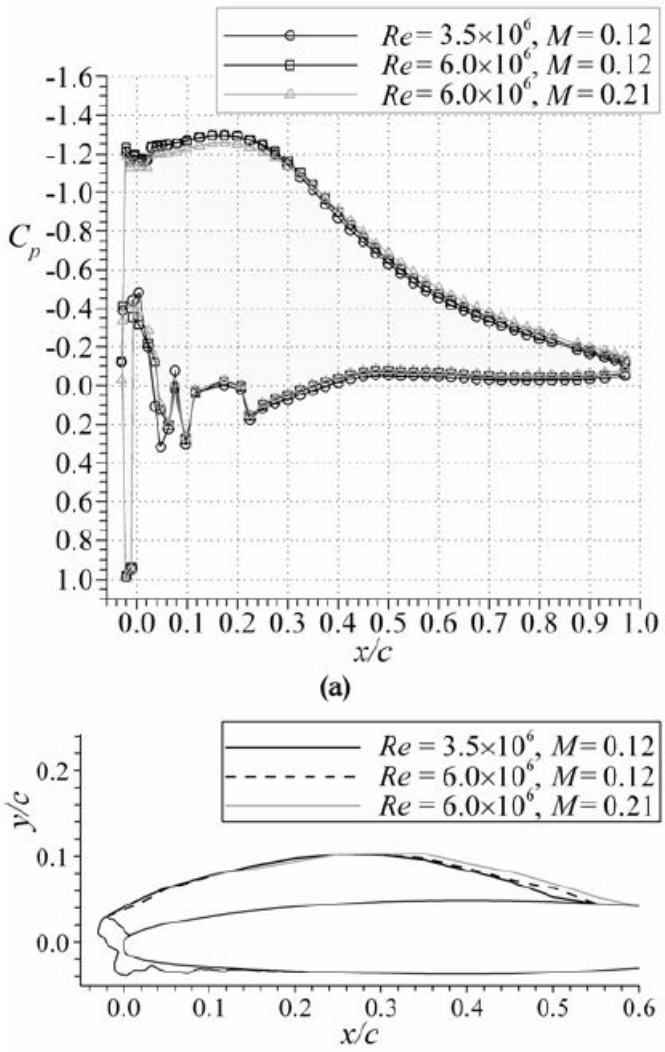

Figure 2.2: Plots of C_p vs. x/c (top) and streamline reattachment (bottom) are shown with changing Re and M for a 2D airfoil with glaze ice accretion. Adapted from Bragg et. al. [1].

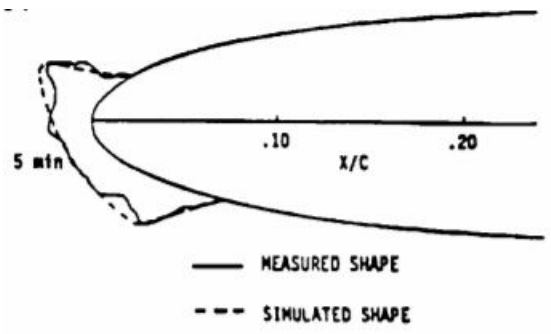

Figure 2.3: A cross-section view of the measured glaze ice shape from the IRT as well as the corresponding simulated ice shape. Adapted from Bragg et. al. [21]

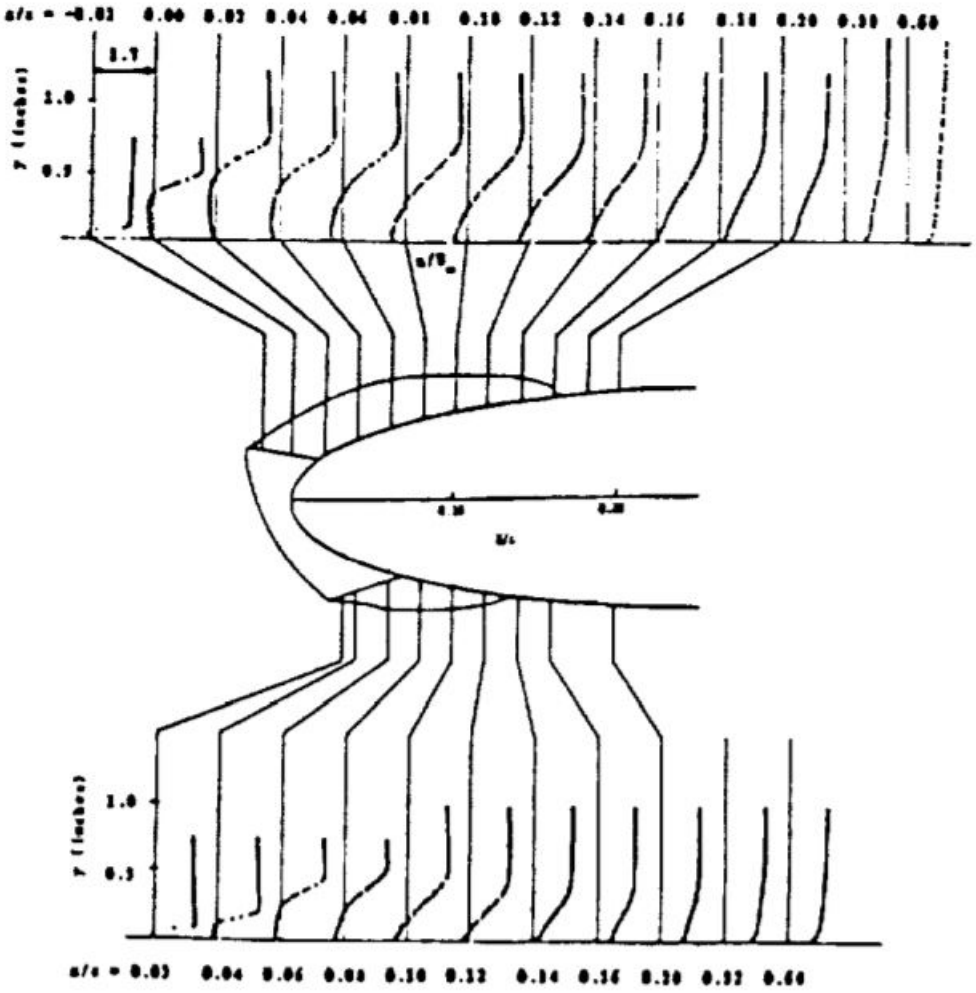

Figure 2.4: Boundary layer traces are shown for different x/c locations over a 2D NACA 0012 airfoil with a simulated glaze ice accretion. Adapted from Bragg et. al. [21]

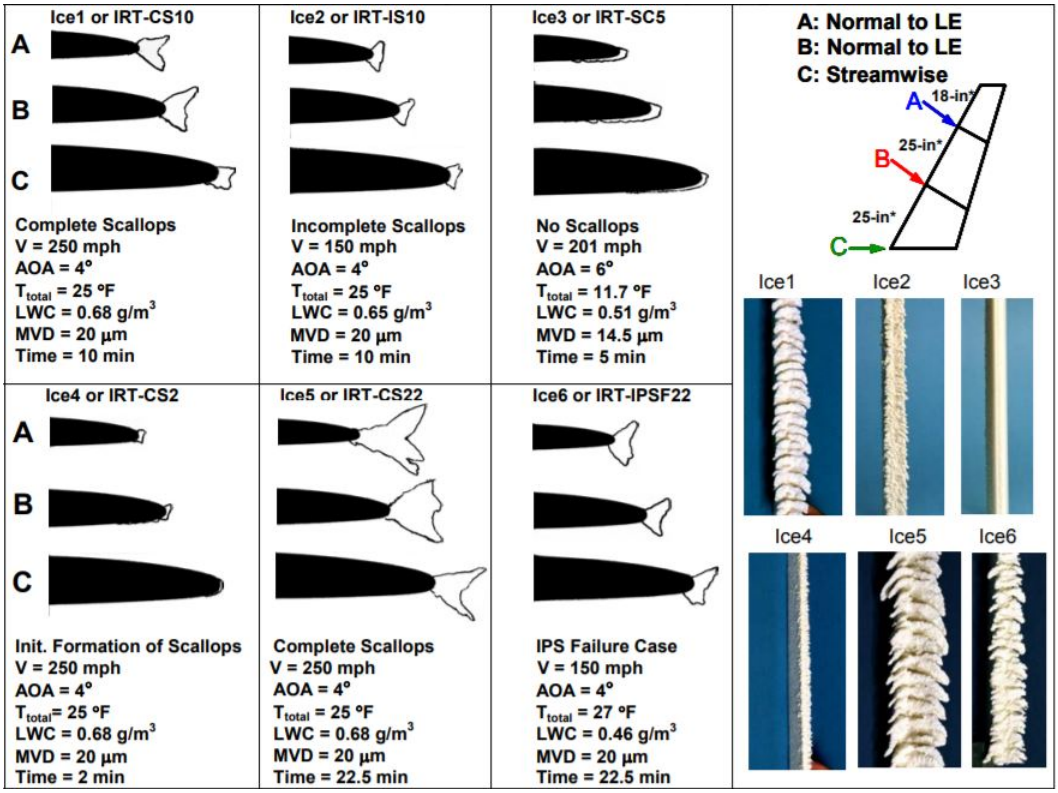

Figure 2.5: Six different glaze ice accretions were tested by Papadakis, and are summarized here with accreition conditions and cross-sections. Adapted from Papadakis et. al. [4].

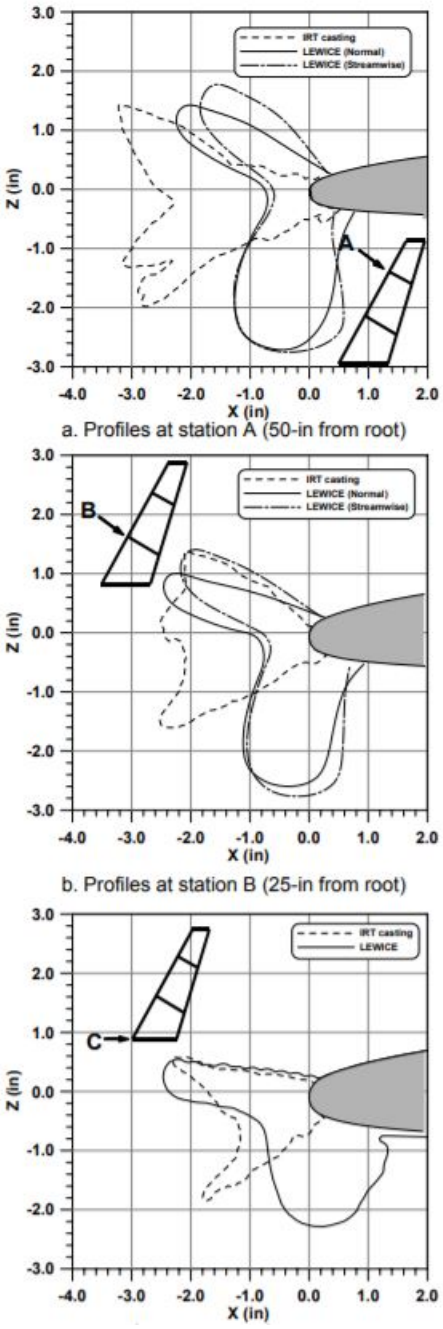

Figure 2.6: Cross-sections at 3 spanwise stations for both the IRT-CS22 ice shape and its corresponding "smooth" configuration created in LEWICE. Adapted from Papadakis et. al. [4].

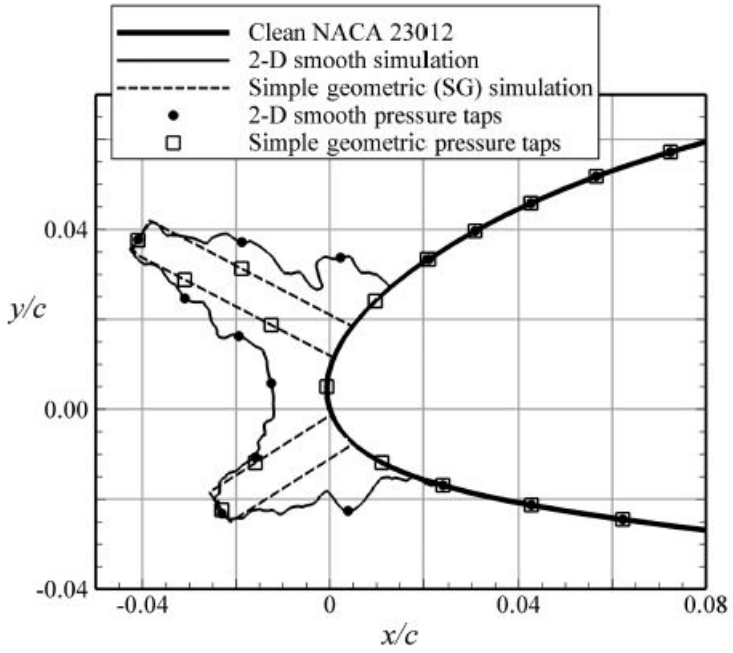

Figure 2.7: Cross-sections of the 2D smooth simulation ice is shown, along with pressure tap locations. Adapted from Busch et. al. [16].

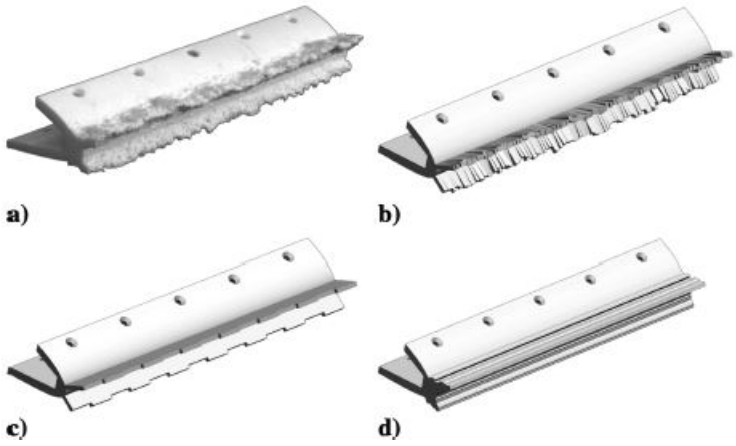

Figure 2.8: Geometric renderings of four simulations of a horn-ice accretion are shown for a NACA 23012 model: a) a casting, b) simple geometric with nonperiodic spanwise variation, c) simple geometric with periodic spanwise variation, and d) 2D smooth simulation. Adapted from Busch et. al. [16].

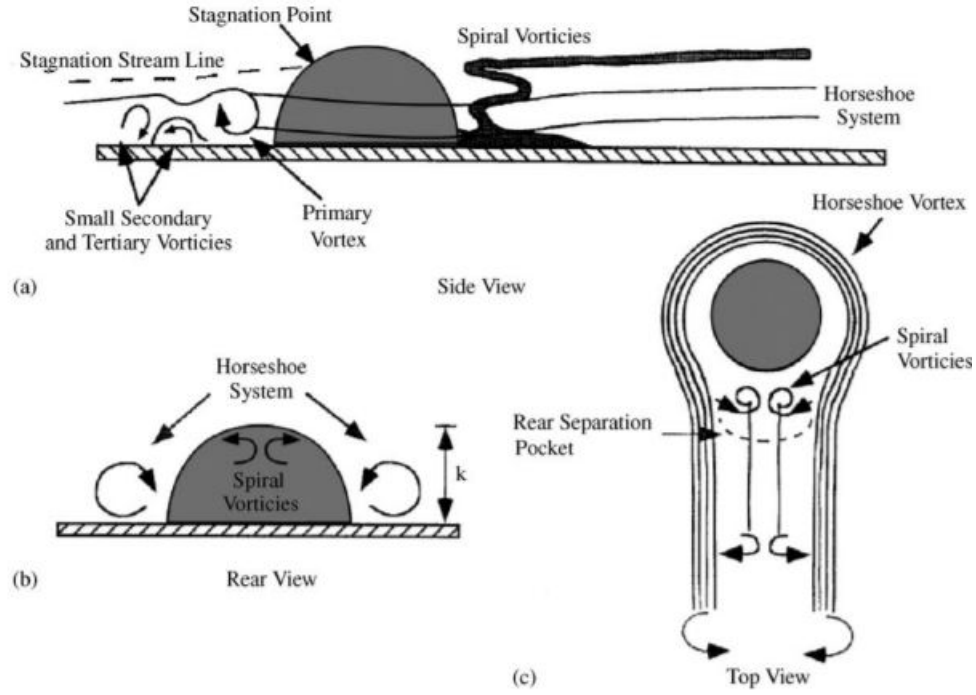

Figure 2.9: The flow around a single hemispherical roughness element on a surface is shown in a) side view, b) rear view, and c) top view. Many interacting vortices can be seen, making this flowfield highly 3D. Adapted from Bragg et. al. [1].

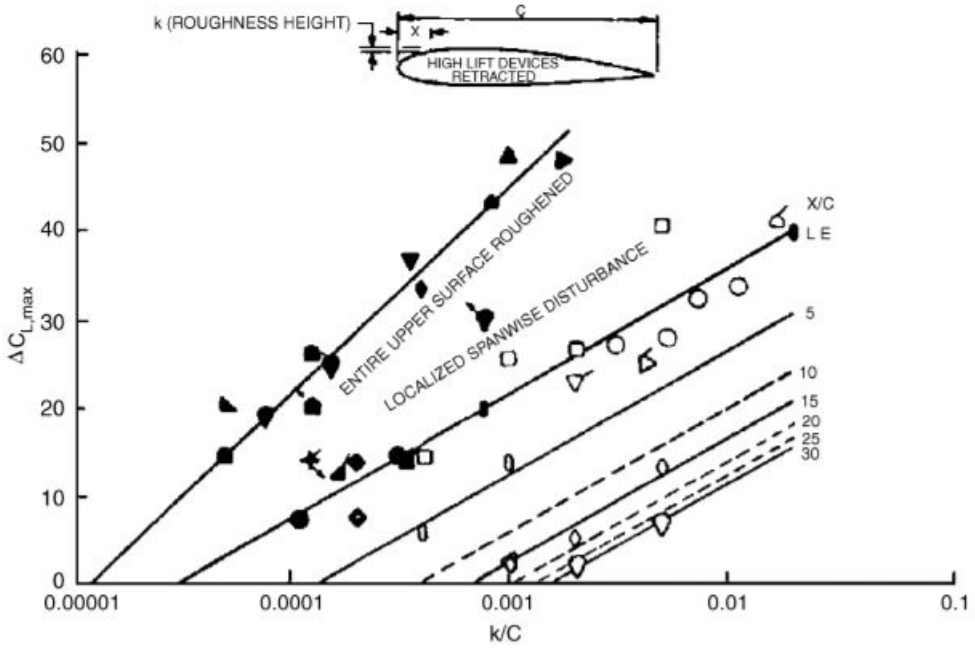

Figure 2.10: Reduction in $C_{L,max}$ due to surface roughness as a funtion of roughness location. Adapted from Brumby [17].

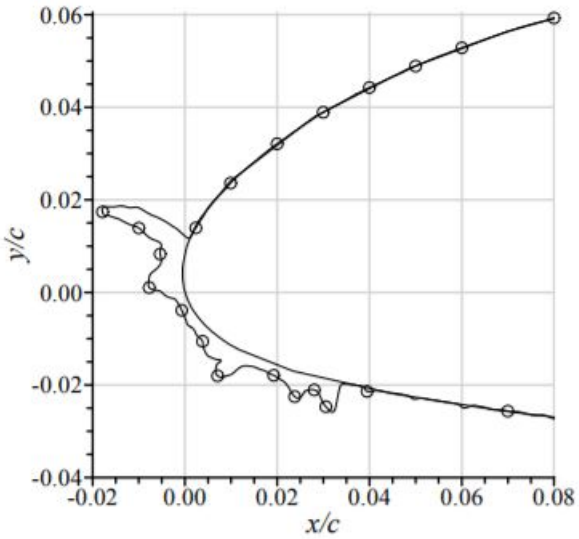

Figure 2.11: A cross-section view of the horn ice used, referred to as the EG1164 shape by Broeren. Adapted from Broeren [3].

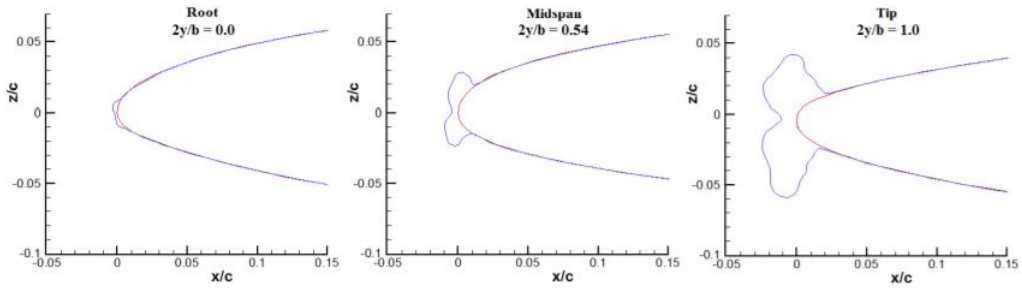

Figure 2.12: Three cross-sections of the ice shape used by Diebold are given. Adapted from Diebold [9].

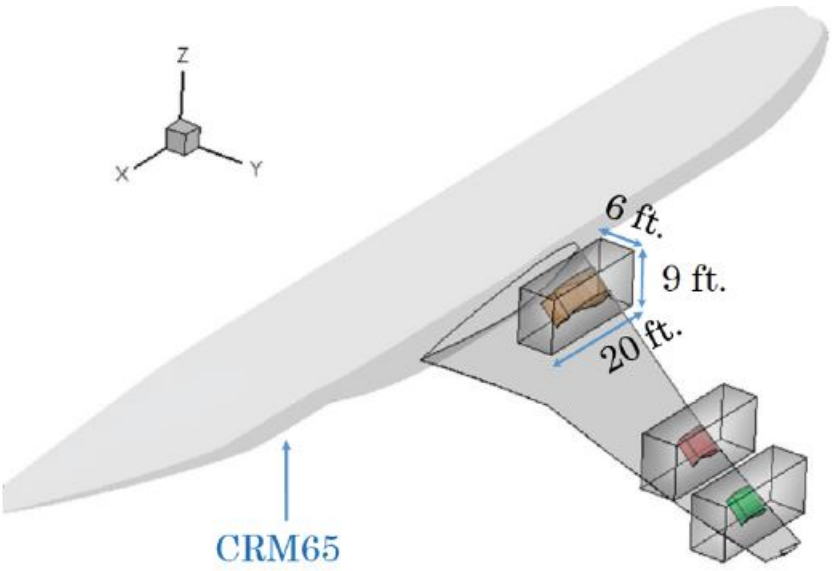

Figure 2.13: The CRM65 model is shown with the test section of the IRT bounding each tested section. Adapted from Fujiwara [28].

Figure 2.14: The resulting hybrid airfoils are shown compared to the full-scale at selected spanwise stations. Adapted from Fujiwara [25].

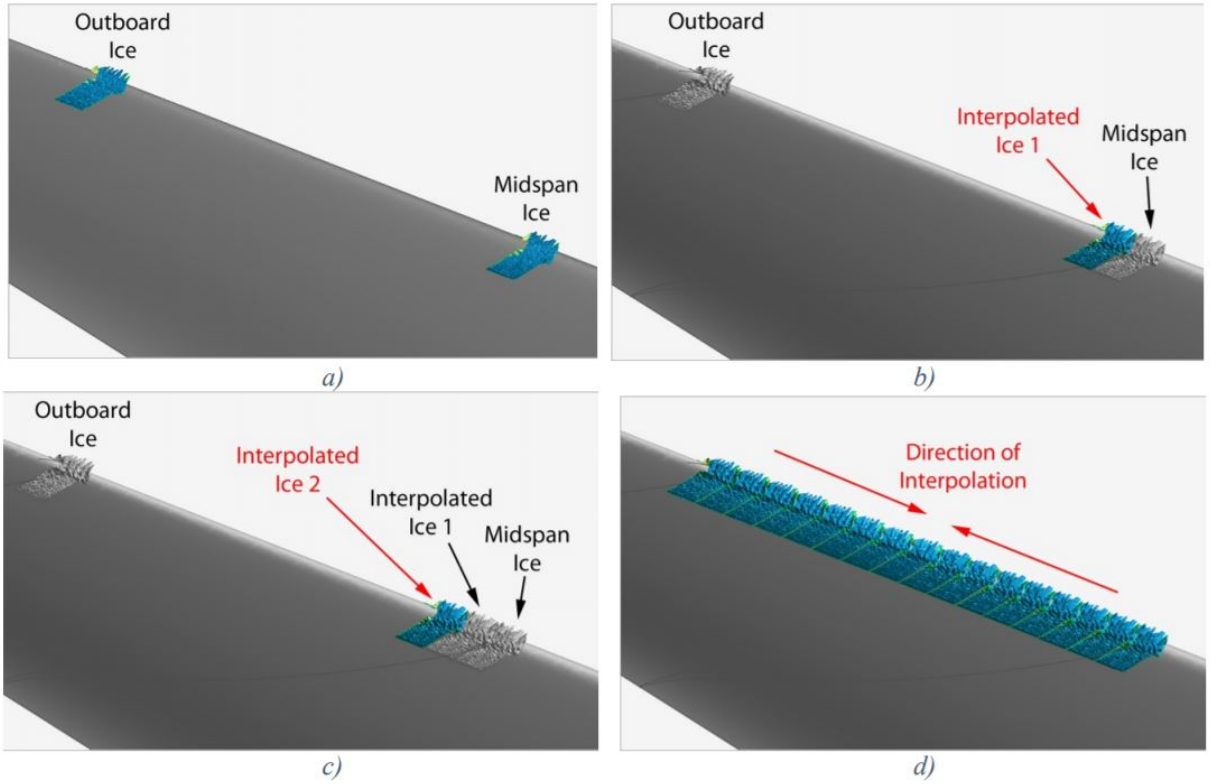

Figure 2.15: Ice accretion interpolation methodology is shown in four steps: a) Take two ice accretions between two adjacent sections (inboard and midspan or midspan and outboard), b) use the weighted averaging function favoring the nearer original accretion in Geomagic studio to form interpolated ice, c) repeat this process using the new interpolated ice shape as the accretion to average, d) stitch accretions and interpolations together to form a single, solid ice shape. Adapted from Camello [22].

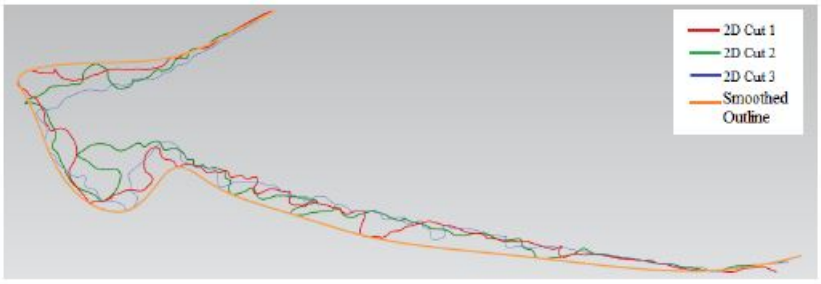

Figure 2.16: One group of three cuts of a high-fidelity ice shape overlaid with the resulting smooth outer contour. Adapted from Camello [22].

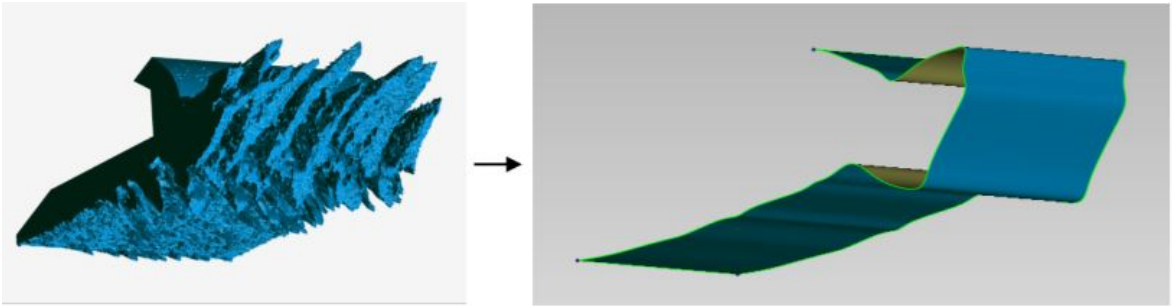

Figure 2.17: A small portion of a high-fidelity horn ice shape is shown compared to its corresponding low-fidelity shape. Adapted from Camello [22].

Chapter 3
EXPERIMENTAL METHODS

There have been several extensive test series that have served to gather the data used for this analysis. The wind tunnel facility, the wind tunnel model, and the various modes of data acquisition will be explored in this chapter.

3.1 Wind Tunnel Facility & Wall Corrections

The wind tunnel used in this test campaign was the 7×10 ft. Walter H. Beech Memorial Wind Tunnel at WSU. This tunnel is a subsonic, atmospheric, closed-return tunnel. Basic specifications for this tunnel can be found in Table 3.1 [27]. A schematic of the wind tunnel is shown in Fig. 3.1. The tunnel uses a six-component truncated pyramid balance built by Aerotech ATE, Ltd [29]. The balance does not measure lift, drag, and moment directly, but instead measures normal force and axial force. The moment reference was fixed in the balance and it was necessary to change the moment reference in data processing; these changes are covered in more detail by Woodard [27]. The load ranges, resolution, and accuracy of the balance is given in Table 3.2.

Wall corrections were applied to all aerodynamic data that was gathered. These corrections were outlined by Pope et. al. [30], implemented by WSU [31], and are summarized by Woodard [27]. That summary is given here for convenience. The four corrections considered are buoyancy, solid blockage, wake blockage, and streamline curvature. Applying these corrections, and understanding their limitations, is key in comparing data gathered at different wind tunnel facilities or comparing results with computational results. These corrections change based on wind tunnel test section and model geometry.

A boundary layer will develop on the test section walls of a wind tunnel, which will

thicken from the front of the test section to the rear. This boundary layer thickness is finite and non-negligible, as the effective cross-sectional area of the test section will decrease. This will cause the subsonic freestream flow to accelerate, causing freestream static pressure to decrease. This increases the effective drag of the model. Accounting for this effect is called the buoyancy correction. The gradient for the pressure in the WSU wind tunnel test section is known [31] and is corrected for using the methods outlined by Pope [30].

Along a similar vane, placing a model in a test section with a finite cross-sectional area effectively decreases that area as seen by the flow. The flow is forced to turn and accelerate around the model, increasing freestream dynamic pressure. This effect is called solid blockage. Wake blockage is a similar effect, but is induced by low-speed flow in the wake of the model. Whereas solid blockage is a function of the model geometry and test section geometry alone, wake blockage is influenced by the geometry and resulting drag of the model. Both blockage corrections are applied to the freestream velocity and dynamic pressure.

Lifting bodies induce curvature in the surrounding flow, which is constrained by the walls of a test section. Thus, the flow is not allowed to move naturally. Corrections must be applied to account for the curvature of the streamlines in the flow. These corrections normally apply to α, pitching moment, and induced drag [27, 30].

3.2 Wind Tunnel Model

The wind tunnel model used was an 8.9% CRM65 wing (a 65% scale CRM wing model) with the 1-g loading removed such that there was no "shear" on the model and the leading-edge was straight. This was done to simplify the design, manufacture, and installation of removable leading-edge ice shapes. A summary of the dimensions of the wing is given in Table 3.3, while an image of the planform of the wing as well as the wing in the test section at WSU is shown in Fig. 3.2. Note that the aspect ratio is calculcated based on a full airplane configuration and not a single wing, that is, the aspect ratio is equal to $\frac{2 * semispan^2}{2 * area\ of\ one\ wing}$. Details on the original design of the CRM model are given by Vassberg et. al. [32] and Rivers et. al. [33].

The wind tunnel model was designed with a removable leading-edge for quick installation and removal of leading-edge ice shapes. A computer-generated render of this division is shown in Fig. 3.3. The ice shapes themselves were rapid prototype models made of Somos® NeXt material [34]. The removable clean leading-edge, along with the rest of the model, were machined from aluminum.

3.3 Data Acquisition Methodology

Data was collected for the clean wing and several ice shapes at α ranging from $-6°$ to $16°$. There were three *Re* and *M* conditions for the freestream. These are summarized in Table 3.4. Note that these Reynolds numbers are not per foot and are based on the mean aerodynamic chord of the model.

3.3.1 Force Balance & Surface Pressure Data

Force balance data was collected using the six-component pyramidal-style external balance discussed in Chapter. 3.1. The normal and axial forces were converted to lift and drag using a coordinate rotation [27]. The uncertainty for these data are described in Chapter 3.3.5. The model also contained 10 rows of pressure taps. These taps are shown on the upper surface in Fig. 3.4. The ESP-32HD electronic pressure scanning module from Esterline was used to collect surface pressures from these taps taps.

3.3.2 Fluorescent Mini-Tufts

Two flow visualization methods were used. Fluorescent mini-tuft data were collected during aerodynamic performance sweeps for many of the model configurations. 0.0019-inch diameter fluorescent monofilament tufts were attached to the model surface with cyanoacrylate adhesive in streamwise rows. The tufts were illuminated by a remote flash with an ultraviolet black light filter so they could be photographed at select angles of attack.

3.3.3 Oil Flow Visualization

The second visualization method used was surface-oil flow visualization. A mixture of motor oil and fluorescent dye was applied to black contact paper on the wing surface with sponge paint rollers. The tunnel was then ramped up to the desired speed for a total run time of two minutes from fan-on to fan-off. Again, the test section was illuminated by a remote flash with a UV black light filter so the model could be photographed with the surface oil. These visualization methods can be used to detect three-dimensional flow characteristics present such as separated flow and vortices. A detailed process for applying the oil to the model is given by Woodard [27].

3.3.4 Wake Survey

The wake survey system uses an array of three five-hole probes from Aeroprobe Corp to collect pressure data in the wake of hte model. The wake survey is unique in that it provides a visualization of the wake of the model, but is also numerical in nature contrary to other visualization techniques. It also provides data that can be reduced to spanwise force distributions, which no other data method used in this study can provide. This is useful as it allows for a numerical comparison between the local aerodynamics over the wing as opposed to the whole. It is also non-invasive to the model for data collection. The drawback is that generating a full-model flowfield from the wake survey system takes significantly longer than any other data collection scheme.

The pressure data collected by the probes can be reduced to sectional lift coefficient, sectional vortex-induced drag coefficient, and sectional profile drag coefficient [35, 36, 37, 38]. Note that vortex-induced drag is slightly different from the more commonly used induced drag coefficient. This term represents the drag due to streamwise vorticity that is shed into the wake, which does not necessarily require lift [38]. A computer-generated render of the probe array used and an image of the array in the tunnel are shown in Fig. 3.5 and Fig. 3.6, respectively. More detailed information on the wake survey system can be found in Appendix

A. Note that these probes are considered "standard response" probes, which collect data at a frequency on the order of Hertz. Thus, there are some time-dependent effects, such as turbulence, that affect the results of these probes. Some of these effects, as well as preliminary work done on implementing a fast-response five-hole probe with iced swept-wing testing, is given in Appendix B.

3.3.5 Data Uncertainty

The uncertainty of the measured data is provided in this section. The accuracy of the balance in the WSU tunnel was 0.02% of full-scale. The uncertainty in the measured dynamic pressure was approximately ±0.1 psf. Two models of pressure tap were used for collecting surface pressure data. Near the leading edge, miniature electronic pressure scanning modules developed by Esterline were used (model ESP-32HD). These modules had a range of ±10.0 psi. The remaining pressure taps used modules with a range of ±2.0 psi. The accuracy of the modules was ±0.03% and ±0.06% for the ±10.0 psi and ±2.0 psi modules, respectively. The uncertainty of the modules is ±0.003 psi for the ±10.0 psi module and ±0.0012 psi for the ±2.0 psi module. Uncertainties in experimental data for an example data point ($\alpha = 4°$, $Re = 2.4 \times 10^6$, and $M = 0.27$) are given in Table 3.5, courtesy of Broeren et. al.[8]. The root-sum-square method outlined by Coleman and Steele [39] and developed by Kline and McClintock [40] was used to determine these uncertainties. This uncertainty analysis is described in more detail by Broeren and Woodard [8, 27].

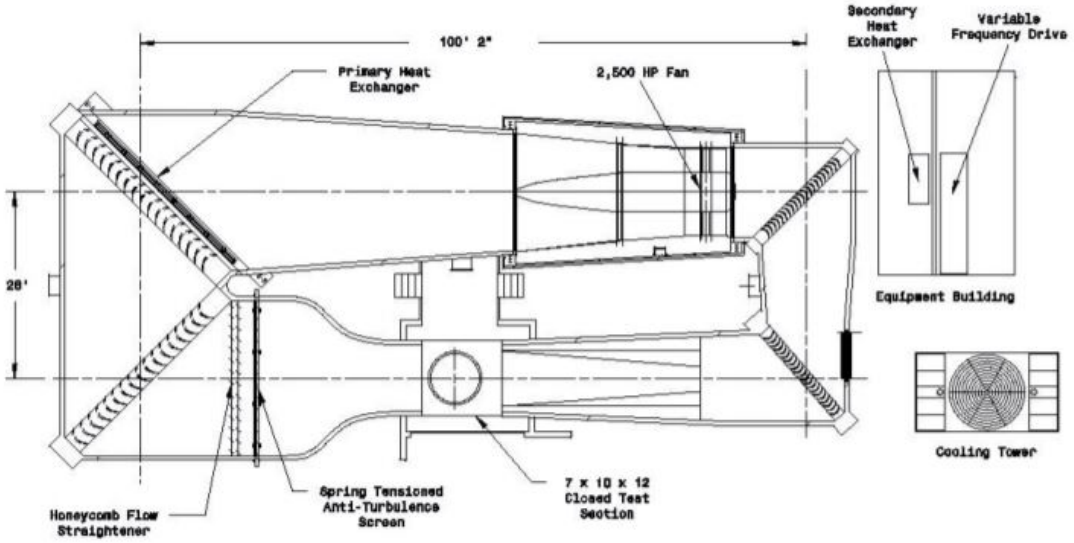

Figure 3.1: A schematic overhead view of the wind tunnel at WSU. Adapted from Irani [29].

Table 3.1: Basic specifications for the WSU wind tunnel.

Measurement	**Value**
Maximum Speed (ft/s)	350
Maximum Re_{ft} (1/ft.)	1.8×10^6
Maximum q (psf)	125
Freestream Turbulence Intensity (% freestream)	0.07

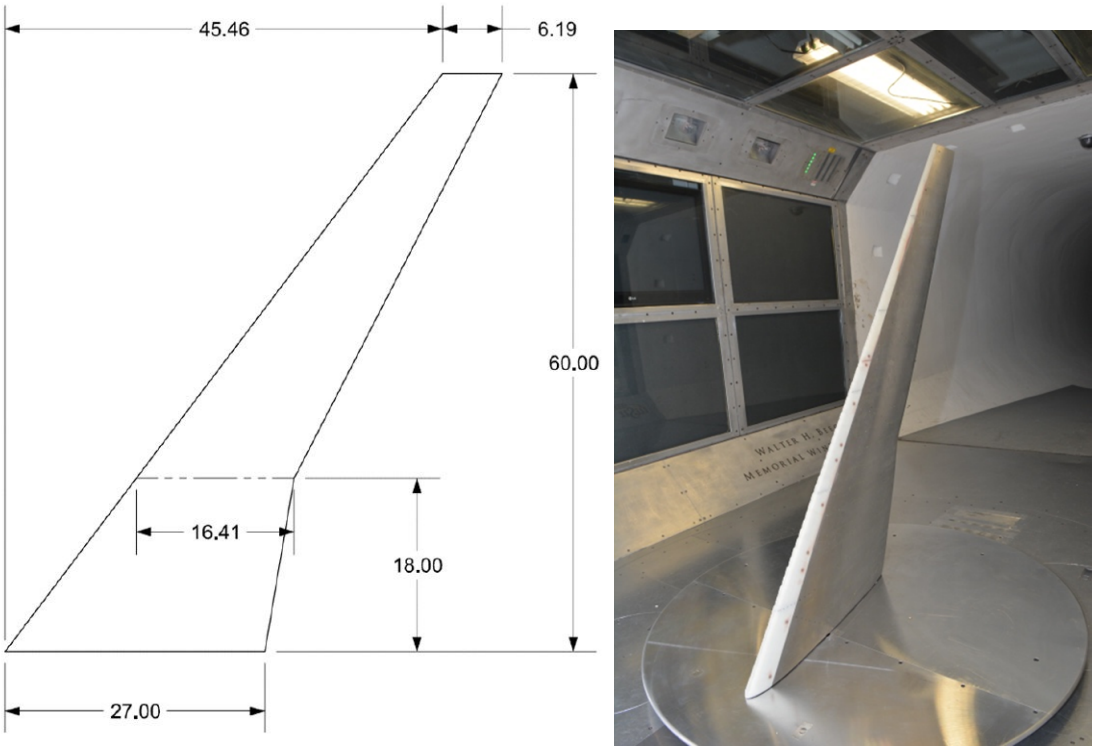

Figure 3.2: Summary of 8.9% CRM65 model dimensions (left) and the model in the wind tunnel at WSU (right). Adapted from Woodard [27].

Table 3.2: WSU six-component pyramidal-style external balance specifications. Adapted from [29].

External Balance WSU/NIAR AeroTech	± Range	Total Range	Full Scale Resolution (0.002%)	Full Scale Accuracy (0.02%)
Lift (lb)	1984	3968	0.079	0.794
Drag (lb)	794	1587	0.032	0.317
Side Force (lb)	1984	3968	0.079	0.794
Pitch Moment (lb-ft)	839	1678	0.034	0.336
Yaw Moment (lb-ft)	818	1635	0.033	0.327
Roll Moment (lb-ft)	4195	8390	0.168	1.678

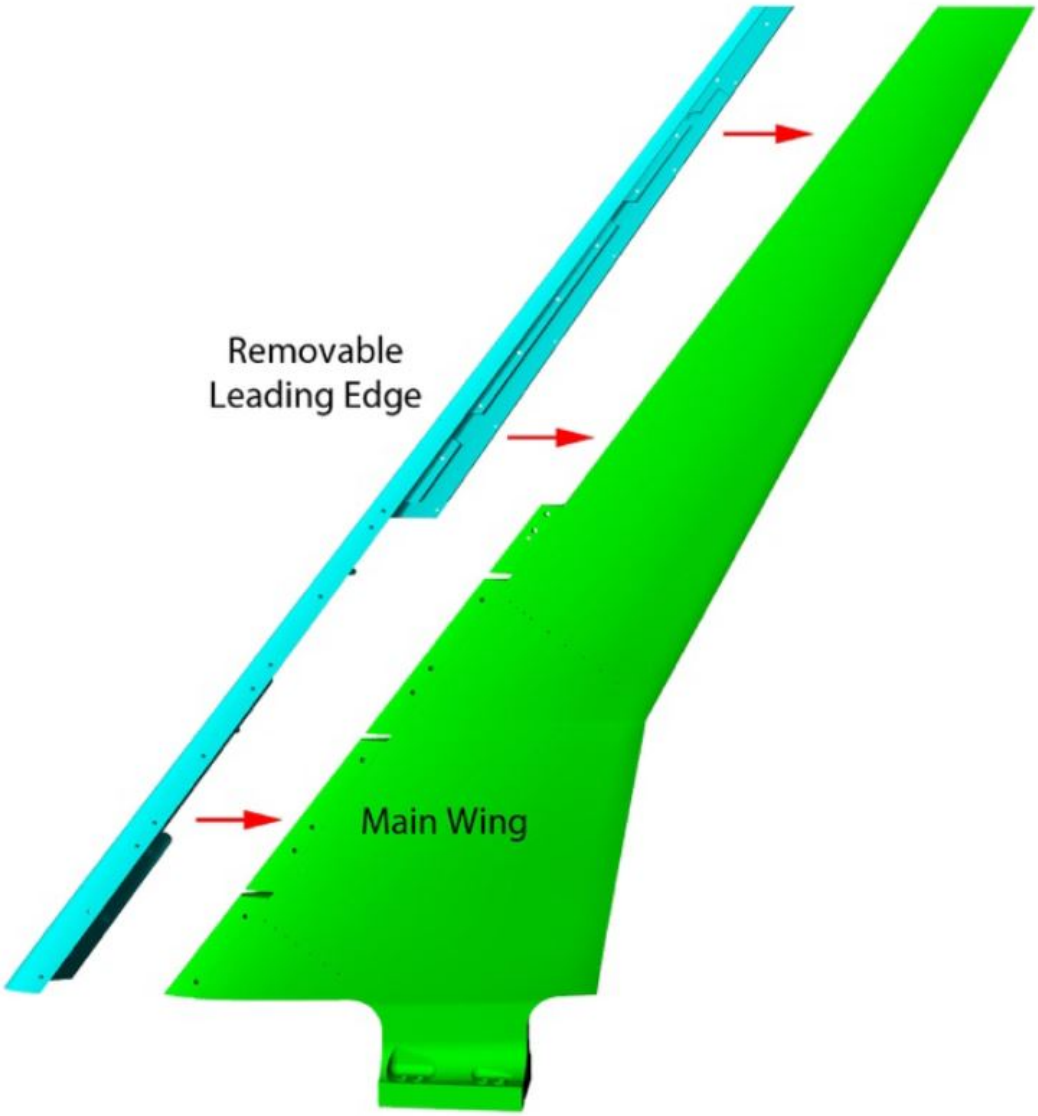

Figure 3.3: A computer-generated render of the removable leading-edge separated from the main wing. Adapted from Camello [22].

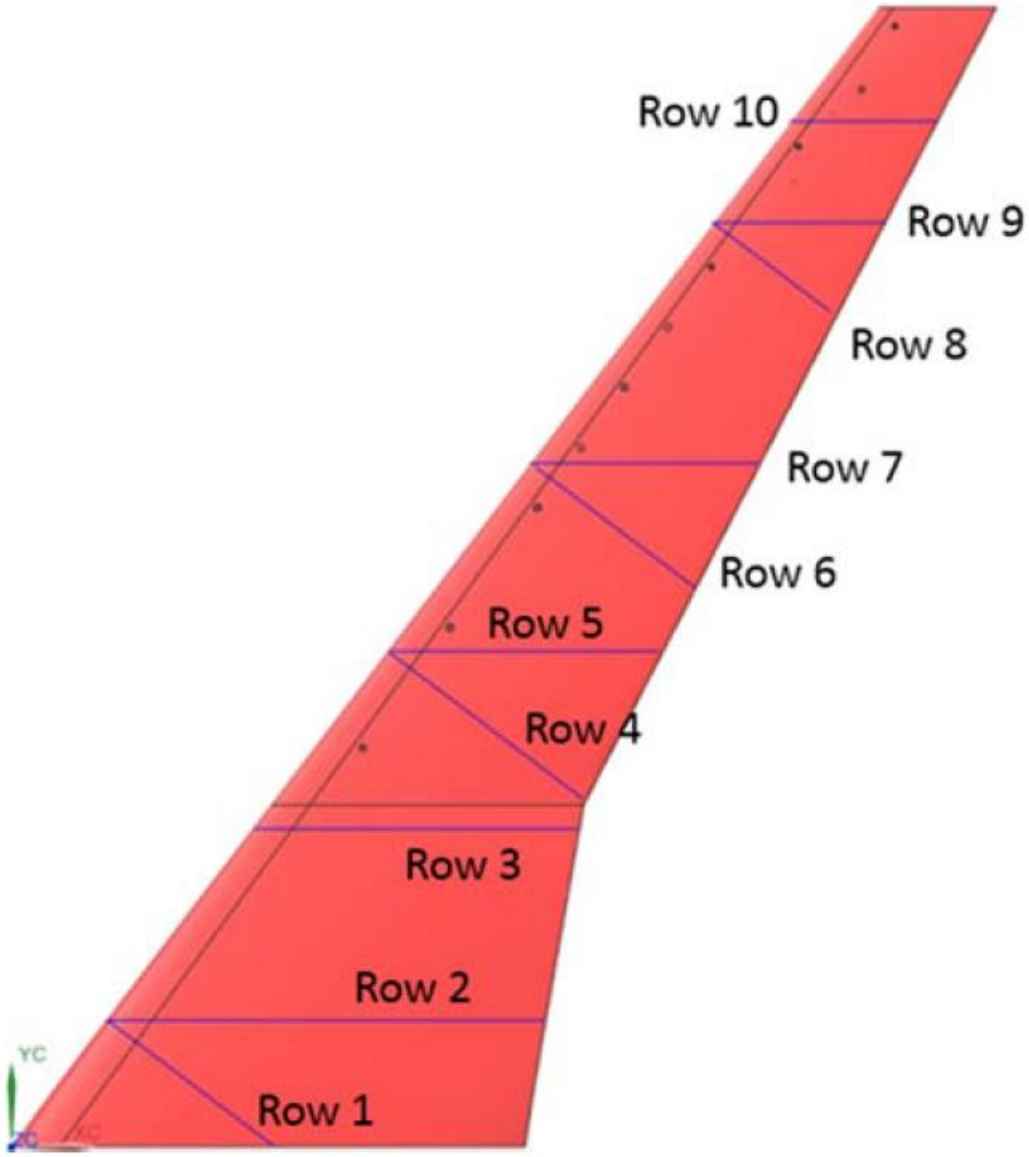

Figure 3.4: Location of pressure taps on the top surface of the wing. Adapted from Woodard [27].

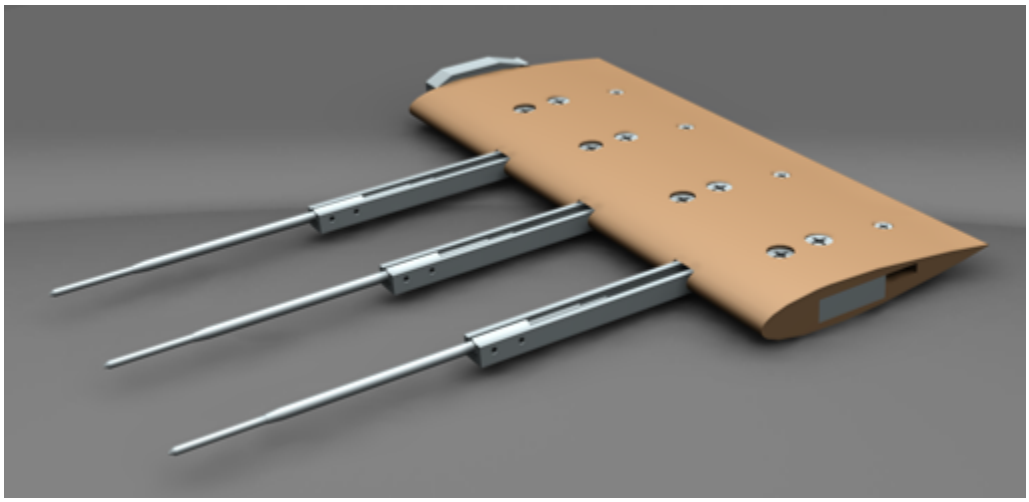

Figure 3.5: A computer-generated render of the probe array used to collect wake data.

Table 3.3: Summary of 8.9% scale CRM65 semispan wing model parameters.

Wing Parameter	**Value**
Span	5.00 ft.
Mean Aerodynamic Chord	1.39 ft.
Area	6.01 $ft.^2$
Aspect Ratio	8.30
Taper Ratio	0.23
Root Chord	2.25 ft.
Tip Chord	0.52 ft.
Washout	8.2°
1/4-chord sweep angle	35°
Leading-edge sweep angle	37.2°

Figure 3.6: An image of the wake survey probe array in the tunnel. Note that this image does not show the aerodynamic fairing. Adapted from Lum [41].

Table 3.4: The Re and M combinations used for the freestream for this series of tests.

Re	***M***
0.8×10^6	0.09
1.6×10^6	0.17
2.7×10^6	0.27

Table 3.5: Absolute and relative uncertainties for example data point for $Re = 2.4 \times 10^6$ and $M = 0.27$.

Variable	**Reference Value**	**Absolute Uncertainty**	**Relative Uncertainty**
α	4.00°	±0.05°	±1.25%
C_L	0.5029	±0.00137	±0.27%
C_D	0.0215	±0.00068	±3.15%
C_m	-0.0067	±0.0006	±9.01%

Chapter 4
DISCUSSION OF RESULTS

A summary of the lift, drag, and moment results for the clean wing for the Re and M combinations tested is shown in Fig. 4.1. The results on the clean model show very similar results at the two higher Re and M combinations while the lower Re and M data deviate more significantly at higher α. The iced data show even less Re and M dependence in this range. Data comparing the aerodynamic performance of the high-fidelity maximum scallop ice shape are shown in Fig. 4.2. As discussed in Chapter 2, the effect of changing Re and M for an iced swept wing was found to be low by Diebold [9] at very low Re due to the ice shape forcing separation at a given point. It should be noted that the data presented here as well as by Diebold [9] is for coupled Re and M. An analysis of the independent effect of Re and M for this wing geometry is given by Broeren et. al. [42]. Lee et. al. [43] are also examining these effects for this wing geometry and show that the effect of both Re and M for the high-fidelity maximum scallop shape is smaller than that for the clean wing, which shows a greater difference in aerodynamics with a change in Re than a change in M.

This thesis will focus on the results for a single combination of Re and M, $Re = 1.6 \times 10^6$ and $M = 0.17$, as the primary goal of this paper is to better understand the swept-wing aerodynamics with ice accretions and how this is affected by ice shape fidelity as opposed to Re and M effects. The ice shape that will be studied, nominally, is the maximum scallop ice shape. This ice shape represents a severe horn ice accretion and provides a good basis for analyzing ice shape aerodynamics as the differences in the geometry between its various fidelities are large. A comparison of the aerodynamic data for the high-fidelity maximum scallop ice shape to the two low-fidelity maximum scallop ice shapes as well as the clean wing is summarized in Fig. 4.3. In this plot there are significant aerodynamic performance

differences between the high-fidelity ice shape and the two 3D smooth representations, with and without grit roughness. The effect of adding the grit roughness on the 3D smooth low-fidelity roughness is small overall, as the aerodynamic performance data between the two 3D smooth representations compare quite well. As these compare so well, this paper will focus on the clean wing, the 3D smooth maximum scallop ice shape without grit (hereafter referred to as the 3D smooth maximum scallop shape or simply the 3D smooth shape), and the high-fidelity maximum scallop ice shape.

Cross-sections for the leading-edge geometry for the 3D smooth maximum scallop ice shape and the high-fidelity maximum scallop ice shape are shown in Fig. 4.4. The geometry for the 3D smooth maximum scallop ice shape is based on the high-fidelity maximum scallop shape. The process of creating the 3D smooth shape from the high-fidelity shape was detailed in Chapter 2.3. The geometry for both ice shapes changes with span. For the 3D smooth ice shape, there is a change in the angle of the local scallop section as well as the 'divot' behind it. These features change progressively across the span. The high-fidelity shape has scallops that extend out from the leading edge. The scallops are the three-dimensional ice features that repeat in the spanwise direction and result in gaps for airflow to move between in primarily a streamwise direction. Figure 4.5 shows the ratio of the width of the scallop features to the width of the gaps between them as a function of span, as measured on the high-fidelity maximum scallop shape. For inboard and outboard sections of the wing, the ratio of scallop width to gap width oscillates around the ratio 1.2. This ratio increases rapidly inboard of midspan, around y/b = 0.36, to almost 2. Evidence will be presented that this variation in the scallops and the resulting gaps likely impacts the flowfield.

4.1 Clean Wing

4.1.1 Force Balance Data

The force balance data in Fig. 4.3 shows several key differences between the aerodynamics for the clean wing and the iced cases. The most notable is the sharp drop in C_L that occurs

for the clean wing at approximately $\alpha = 13.5°$. This sharp drop in C_L, considered to be the stall point for this wing, is accompanied by a large increase in C_m and C_D. At stall, there are massive amounts of separation over a wing. This separation has several effects, including an increase of pressure over the top surface (decreasing lift), a change in the location of the center of pressure (altering C_m, in this case having a negative impact), and an increase in pressure drag (in turn increasing total drag).

Figure 4.6 shows $\frac{\delta C_L}{\delta \alpha}$ as a function of α for all considered cases. Though the slope of the lift-curve for the clean wing looks linear in Fig. 4.3, it is not. For the clean wing, there are two major points of change for positive α according to this plot: at approximately $\alpha = 3.5°$ and $\alpha = 13.5°$. The second point clearly corresponds to stall. However, the first is more intriguing. For low α on the clean wing, there is most likely no major separation. The sudden increase in the lift-curve slope after decreasing steadily from approximately $\alpha = -3.5°$, therefore, must be attributed to something more subtle. This and other effects will be explored in this section.

Note that C_m is with respect to the quarter-chord of the wing. There is a nose-down pitching moment, quantified as a negative $\frac{\delta C_m}{\delta \alpha}$, until just before stall at $\alpha = 12°$. This is an inflection point in the C_m curve that Furlong and Mchugh [11] define as the point at which a significant shift in the aerodynamic center occurs such that increasing α beyond this point will require active stall control. The lift coefficient that corresponds to this inflection point is called the "usable lift" and is a point of comparison among different configurations.

4.1.2 Mini-Tuft Imagery

The progression of 3D effects and flow separation with increasing α is seen clearly using flow visualization. Figure 4.7 shows mini-tuft imagery for the clean wing for $\alpha = 4.31°$, $\alpha = 8.50°$, $\alpha = 10.57°$, and $\alpha = 12.63°$. The clean swept wing flowfield at increasing angle of attack is characterized by the formation of a leading-edge separation vortex, strong spanwise flow that develops on the upper surface near the trailing edge, and eventually large-scale flow separation. These features are well known and are described by Poll [14] and have been

identified for this geometry in several earlier papers [8, 9, 44].

At $\alpha = 4.31°$ the mini-tufts are in the streamwise direction across the span. There is no motion-blur of the tufts to indicate any unsteady or separated flow. As α increases to 8.50°, there is some outboard movement of the tufts near the trailing edge of the wing. The tufts indicate a spanwise flow direction, from the wing root to the wing tip. This spanwise flow is a classic swept-wing phenomenon. For $\alpha = 10.57°$, the mini-tufts show spanwise flow near the trailing edge from root to tip. On the outboard section of the wing, there are reversed mini-tufts near the wing tip identifying separation occurring near the wing tip. This was also seen by Broeren [8]. While this wing has significant washout (over 8°) intended to reduce the tendency of swept wings to experience tip stall, the wing tip Re is low for these tests and well below the design value. There is also a large amount of loading in the outboard of the wing compared to the inboard. The classic explanation for tip stall involves the boundary layer over the outboard sections of the wing thickening due to spanwise flow, coupled with the adverse pressure gradient from the heavy loading to cause early tip separation. An interesting byproduct of the spanwise flow causing the tip to stall is that it has the opposite effect near the root. As boundary layer fluid moves from the wing root toward the wing tip, a low-pressure region is created at the root that helps keep the boundary layer in the inboard sections attached. Thus, while the tip stalls early, the inboard of the wing becomes harder to stall. This is also seen in these tuft images as the root region of the wing does not ever show reversed tufts indicating flow separation and stall. The mini-tuft imagery for $\alpha = 12.63°$ shows that separation continues to occur from the outboard to the midspan region of the wing. Though the change in α is small (approximately 2°), the separation progresses quickly, and continues to do so until $C_{L,max}$ occurs at approximately $\alpha = 13.5°$. The sharp stall progression is seen very clearly in the change in mini-tuft imagery from $\alpha = 12.63°$ to $\alpha = 13.58°$. The mini-tuft imagery from the latter case is shown in Fig. 4.8, and separated flow is seen from the wing tip to just inboard of the Yehudi break. This massive increase in separation corresponds to the stall point seen in the force balance data. Intriguingly, stall begins to set in between $\alpha = 10.57°$ when it is first seen and $\alpha = 12.63°$ when it progresses

beyond just the tip. This range of α may correspond to the "usable" lift coefficient described by Furlong and Mchugh [11]. Stall in this outboard region would cause loss of authority of outboard control surfaces for aircraft as well as a shift forward of the center of pressure (an unstable phenomenon) which coincides with the definition of Furlong and Mchugh that the inflection point of the C_m curve denotes the maximum usable lift before stall control is required.

4.1.3 Oil Flow Visualization

In Fig. 4.9 and Fig. 4.10, surface oil flow is shown for $\alpha = 4.31°$, $\alpha = 8.50°$, $\alpha = 10.57°$, and $\alpha = 12.63°$. The oil flow visualization at lower α in Fig. 4.9 shows a leading-edge separation vortex. The vortex is small and not visible in the mini-tufts. Primary separation occurs on the leading edge, the flow reattaches a short distance downstream, and the reverse flow experiences a second, secondary separation, downstream of the initial separation point. These features are identified in the oil downstream of the leading edge, where in this upper surface view separation occurs but cannot be easily seen, followed by a bright spanwise pooling of oil, which is the secondary separation, and then a black region relatively void of oil, which is just ahead of reattachment where the oil is scrubbed forward to form the bright secondary separation line. This type of flowfield has been extensively studied in 2D and described by many authors including for the icing case by Bragg et al. [1]. The primary difference here, due to the spanwise gradients, is the rolling up of this separation into a spanwise vortical, or vortex flow. Kerho et. al. [6] show this feature clearly on a swept iced wing using laser Doppler velocimetry flowfield measurements and helium bubble flowfield tracers. Note that there are also very small regions of tip separation, even for these low α cases. This separation is an effect of the wing tip vortex causing oil to scrub off from this region of the wing and is a separate phenomenon to the extended wing tip separation and stall seen at higher α.

The oil flow imagery shows both types of the tip separation at $\alpha = 10.57°$. The tip separation caused by spanwise flow, away from the wing-tip vortex, grows in extent at $\alpha = 12.63°$. The leading-edge vortex in this α range expands rapidly near the wing tip. This

expansion likely contributes to the separation occurring in this region, along with the spanwise flow. This separation region grows large for $\alpha = 12.63°$. This data mirrors the mini-tuft imagery, showing the large amounts of separation as α approaches $\alpha_{stall} = 13.5°$.

4.1.4 Surface Pressure Data

Figure 4.11 shows the upper-surface C_p distributions for the clean wing at $\alpha = 4.31°$, $\alpha = 8.50°$, $\alpha = 10.57°$, $\alpha = 12.63°$, and $\alpha = 13.58°$ for the six streamwise rows on the wing. The root C_p distributions are on the right side of each the plot and the tip on the left. For low α, the pressure coefficient peaks (low pressure) near the leading edge, indicating a large amount of suction on the upper-surface leading edge of the wing. The pressure coefficient distributions show suction on the upper surface continuing to increase as α increases to 8.50°. For $\alpha = 10.57°$, separation is seen near the wing tip. However, there are no pressure taps in this region (for y/b > 0.9), and thus this separation is not seen clearly in the C_p distribution. The tip-most pressure row shows a slight pressure increase near the leading-edge, which may be an effect of the separation in this region. For $\alpha = 12.63°$, there is separation seen covering most of the outboard region of the wing. This is seen in the C_p distribution clearly. The outer two pressure rows show C_p has increased and is relatively flat along the local chord for these regions, indicating the same flow separation seen in the flow visualization. These two rows correspond to y/b $= 0.81$ and y/b $= 0.9$. $C_{L,max}$ for the clean wing occurs at approximately $\alpha = 13.5°$. At this point, the lift coefficient drops sharply, the drag coefficient increases rapidly, and the change in C_m with α becomes positive. The change in pitching moment with α becoming positive is a classic effect of swept wings experiencing tip stall and approaching $C_{L,max}$. As α increases to 13.58°, which is just past the stall point noticed in the force balance data, there is a large amount of separation seen in the C_p distribution. The outboard four pressure rows show almost constant pressure along the local chord. There is also a lack of a pressure peak near the leading edge for these rows, indicating that the suction over the upper surface in these regions has been drastically reduced. This all agrees with both the flow visualization imagery and the force balance data.

4.1.5 Wake Survey Data

The data shown in Fig. 4.12 and Fig. 4.13 shows data collected by the wake survey system. Figure 4.12 shows a contour plot of the streamwise velocity deficit, $\frac{u}{U_\infty}$, in the wake of the wing. Note that the wake has some jaggedness associated with its edge. This is due to the technique used to isolate the wake from the freestream, which is explained in more detail by Lum et. al. [41]. The dark red seen near the edge of the wake indicates that the wake streamwise velocity is almost equal to the freestream velocity. As the color changes from red to yellow, the streamwise velocity decreases based on the scale given in the figure. Larger velocity deficits are marked by blue colors. The figure also shows flow direction in the cross-flow plane as vectors. These vectors show the rotation of the flow.

There is a strong similarity in the wake data for $\alpha = 4.31°,\ 6.41°$, and $8.50°$. The wake is relatively thin with a band of yellow in the middle region, indicating a streamwise velocity that is approximately 92% to 95% of the freestream. The wing tip vortex is clear near y/b = 1 for these three α as well. As α increases to $10.57°$, a secondary region of low streamwise velocity is seen just inboard of the wing tip, near y/b = 0.92. This region likely corresponds to the separation seen at the wing tip in the flow visualization. There is some vorticity associated with this separated flow, and that may manifest as stronger cross-flow components, seen as vectors in the figure. However, vorticity associated with the separated flow is likely dominated by the vorticity associated with the wing-tip vortex and is thus hard to distinguish.

One advantage of the wake survey technique over other data collection techniques is the ability to reduce the data collected to spanwise variations in lift coefficient and drag coefficient. These sectional coefficients give insight into the local aerodynamics at a given point on the wing. The process of this reduction is covered in more detail by Lum et. al. [41] and Diebold [37]. Figure 4.13 shows the sectional lift coefficient and sectional drag coefficient as a function of span at the same α. The distribution of lift is generally quite smooth, with the inboard sections showing lower relative loading due to larger local chord. The spanwise trend of sectional lift coefficient does not change with α for the cases shown. Note that wake

survey data was not taken for higher α than what is shown here. Sectional drag coefficient, though more jagged in its spanwise distribution, has a general trend of increasing from inboard to outboard for all α. Sectional drag coefficient is comprised of both profile drag and vortex-induced drag. Thus, in regions of high vorticity (which tend to be, but are not restricted to, regions of high lift) and in regions with separation, sectional drag coefficient will increase. This effect is noticeable for $\alpha = 10.57°$, as near the wing tip, there is separation that is seen in the flow visualization. In this same outboard region, sectional drag coefficient is very high for y/b > 0.9. This region likely corresponds to the separation region seen in the flow visualization, as well as the small region of decreased streamwise velocity seen in the wake contour plot in Fig. 4.12.

4.1.6 Clean Wing Aerodynamics Summary

The data seems to agree with respect to the phenomena occurring on the clean wing as α increases, but of course not all data types can pick up on all phenomena. The clean wing shows signs of spanwise flow near the trailing edge and leading-edge separation, which begin at low α. These trends give way to tip separation and the formation of a leading-edge vortex as α approaches stall. The wing tip stalls prior to the inboard and midspan sections of the wing. This tip stall moves aggressively inboard, leading to $C_{L,max}$ at approximately $\alpha = 13.5°$. This point is also marked by a large drag rise and an unstable pitching moment. The change in separation over the wing is rapid, with separation progressing from the outboard of the wing to the Yehudi break with an increase of α of approximately 1°. Prior to this stall, a leading-edge vortex forms along the span of the wing that later diffuses rapidly, contributing to separation of the flow at the wing tip. Flow separation is also likely caused by the spanwise flow moving from the root of the wing to the tip thickening the boundary layer and creating a strong adverse pressure gradient.

4.2 3D Smooth Maximum Scallop

Two low-fidelity versions of the maximum scallop shape were tested as part of this wind tunnel program. They are both geometrically based on the high-fidelity maximum scallop ice shape. One of the shapes had 60-grit roughness manually applied to simulate roughness effects associated with the high-fidelity ice shape. Figure 4.3 shows the change in C_L and C_D with α for both shapes. Aside from a small shift in magnitude, the smooth and rough shapes have nearly identical aerodynamic performance. Thus, for this *Re* and *M*, the effect of roughness is considered negligible, and only the 3D smooth maximum scallop shape without grit will be considered for comparison to the high-fidelity maximum scallop shape and the clean wing.

4.2.1 Force Balance Data

Examining Fig. 4.3 more closely for the 3D smooth maximum scallop shape, the aerodynamic performance of the iced versus the clean wing shows a lift-curve slope that is generally lower than for the clean wing and reduced maximum lift. Note that there is no sharp change in the lift-curve for the 3D smooth shape as there is for the clean wing at $\alpha = 13.5°$, indicating that there is likely not a sharp stalling process for this iced wing configuration. The slope of the pitching moment curve is larger than that of the clean wing, implying that this configuration is less stable. The inflection point of this curve occurs sooner than the clean wing at approximately $\alpha = 7.5°$, which is about 4.5° less than the clean wing. With the definition of usable lift from Furlong and Mchugh [11], this means that the usable lift for the 3D smooth shape is significantly lower than the clean wing, approximately $C_L = 1$ versus $C_L = 0.68$. For α less than 6°, the drag coefficient is for the 3D smooth shape is significantly higher than the clean wing. At low α, a large portion of the drag would come from profile drag, as lift at these angles is relatively low. Thus, it is likely the existence of the ice shape alone that is causing this increase in drag in this regime. The disparity between C_D for the 3D smooth shape and the clean wing increases with α from 6° to approximately 13.5° when

stall for the clean wing occurs. At this point, C_D jumps up for the clean wing, and the drag coefficient for the 3D smooth shape and the clean wing is much closer. At these higher α, much of the flow is separated over the clean wing. Based on this plot, this must also be true for the 3D smooth shape, as there would otherwise continue to be a large disparity between the two cases.

Note that in Fig. 4.6, the lift-curve slope for the 3D smooth shape is smoother than the clean wing case, implying a more gradual change in the aerodynamics with increasing α. This difference is likely attributed to different separation regimes for the iced wing case and the clean wing case. That is, the clean wing experiences leading-edge separation while the iced wing may experience traits of both leading-edge and trailing-edge separation. Note the large change in the lift-curve slope for the 3D smooth shape between approximately $\alpha = 6°$ and $\alpha = 10.5°$. This region exists as there is a large change in the aerodynamics around these α. This will be explored in more detail in following sections.

4.2.2 Mini-Tuft Imagery

The differences in the aerodynamics between the 3D smooth shape and the clean case can be examined in more detail using flow visualization data. Mini-tuft imagery for the 3D smooth maximum scallop ice shape at $\alpha = 4.30°$, $\alpha = 6.40°$, $\alpha = 8.46°$, and $\alpha = 10.50°$ is shown in Fig. 4.14. Note that some of these α are different than the clean case. At $\alpha = 4.30°$, evidence is seen in the tufts of leading-edge separation and leading-edge vortex formation in the midspan region, seen as reversed mini-tufts in this region. At a comparable α, the clean wing mini-tuft data (Fig. 4.7) saw no separation or vortex present. There is also some motion blur of the tufts near the leading edge of the wing just outboard of y/b = 0.5, which is evidence of unsteady flow over the surface of the wing. Similar to the clean wing, however, this is almost no spanwise flow seen at this low α. As α increases to 6.40°, the tufts for the 3D smooth shape show that the separation region has grown rapidly over the outboard section of the wing and has also spread more inboard. The spanwise flow near the trailing edge is extensive. Note that near y/b = 0.5, two regions of leading-edge separation are seen divided

by a row of mini-tufts near the midspan of the wing that is aligned with the freestream, which seems to be a region of reduced separation. This midspan region of reduced separation is possibly due to a change in the 3D smooth ice shape geometry. The curvature of the ice shape changes with span, as seen in Fig. 4.4 for the 3D smooth shape in the top image. This figure shows the cross-section of the ice shapes at three spanwise locations. There is a change in the local horn shape that extends from the leading-edge, though it should be reiterated that this shape is smooth when seen in three dimensions. The iced geometry sees a change in the angle made by the local horn shape with respect to the freestream as well as a change in the extent of the "divot" just downstream of the horn tip, which is a result of the ice shape merging with the wing's leading edge. These changes will alter the local aerodynamics. The ice shape near the midspan region becomes slightly more streamline compared to the inboard shape and outboard shape with the ice "blending in" to the leading-edge shape of the wing more closely than the other two cross-sections. This may have reduced the effect of separation in this region. However, without more detailed data in this region (such as off-body flow visualization) nothing can be said for certain regarding this spanwise change in geometry and its local aerodynamic effect. It may also be argued that 3D effects are not being considered, but it should be noted that the region where flow separation is reduced does not cover just a single spanwise location, but has a spanwise "sweep" toward the wing tip as well. Thus, it is possible that the local, seemingly more streamline leading-edge shape at y/b = 0.5 is creating a region of reduced separation that affects not only the y/b = 0.5 section, but spanwise stations slightly further outboard from this point as well. There is some spanwise flow seen in the tufts in the reduced separation region as well, which is more evidence of this theory.

For the higher α cases, $\alpha = 8.46°$and $10.50°$, separation dominates the wing from just inboard of the Yehudi break to the wing tip. The region of reduced separation seen for $\alpha = 6.40°$ has disappeared. These large amounts of separation are similar to the clean wing at higher α, indicating that the 3D smooth ice shape can cause stall-like aerodynamics to occur at lower α than is natural for this wing at these Re and M conditions. This α range for

an increase of separation coincides with Fig. 4.6, which shows a large change in aerodynamics between $\alpha = 6°$ and $\alpha = 10.5°$. Based on the mini-tuft imagery, the separation regions expand steadily between $\alpha = 6.40°$ and $\alpha = 8.46°$. The inflection of C_m occurs at approximately 7.5°, which falls almost exactly in the middle of this range of separation expansion. Thus, the mini-tuft imagery seems to agree with the force balance data in terms of the phenomena occurring and when they occur.

4.2.3 Oil Flow Visualization

The oil flow visualization for $\alpha = 4.30°$ and $\alpha = 6.40°$ is given in Fig. 4.15. The oil flow imagery for $\alpha = 4.30°$ shows a distinct reattachment line that results due to the separation and formation of the leading-edge vortex and corresponds well to the tuft data. Due to the higher "resolution" of the oil flow visualization compared to the mini-tufts, more of the leading-edge separation and vortex can be seen, though the small region of separation seen in the tufts for $\alpha = 4.30°$ seems to manifest as a thicker portion of the leading-edge vortex. The separation region for this α is much larger than that of the clean wing at a comparable α. For $\alpha = 6.40°$, the oil flow visualization confirms the significant separation seen in the tuft data. There is a region of oil accumulation near of y/b = 0.5 that is followed by a dark, oil-scrubbed region slightly outboard of this point. This correlates with a region of streamlined tufts seen for the same α. Note, though, that this is the same region in which there is a physical seam on the ice shapes as the ice shapes were built in two halves and then attached to the model. Thus, this may be a product of the assembly of the wing and not a property of the iced wing itself. The large recirculation regions seen in the oil flow visualization for $\alpha = 6.40°$ mirror the large separation regions seen in the mini-tuft data. Note that $\alpha = 6.40°$ also corresponds to the rapid increase of C_D seen for the 3D smooth shape in Fig. 4.3. After approximately 6°, C_D increases steadily and more quickly than for the clean case. This is an effect of the increasing separation that occurs over the wing with the 3D smooth shape attached at a similar α. Note that no oil flow visualization data was collected for $\alpha = 8.46°$ and $\alpha = 10.50°$

4.2.4 Surface Pressure Data

The flow separation pattern is seen in the C_p distribution data shown in Fig. 4.16 for $\alpha = 4.30°$, $\alpha = 6.40°$, $\alpha = 8.46°$, and $\alpha = 10.50°$. Note that there are no pressure taps in the ice shape itself, and thus the pressure coefficient data point closest to the leading edge is further downstream than in the clean case. For the clean case, the first pressure tap is located at a local x/c station of 0 for each pressure row. For both ice cases, the streamwise pressure row nearest the root begins at local x/c = 0.0075. The streamwise pressure row nearest the tip begins at local x/c = 0.05. All other streamwise pressure rows begin at local x/c = 0.015.

The pressure coefficient distribution for the 3D smooth maximum scallop ice shape at $\alpha = 4.30°$ is similar to the clean wing at comparable α. The suction peaks are slightly lower in the iced case, but this is likely explained by the lack of a leading-edge tap. This lack of taps near the leading-edge also prevents the surface pressure data from capturing the separation near the leading edge. The surface pressure data otherwise shows high pressure gradients in the streamwise direction for all pressure rows, similar to the clean wing at a comparable angle. As α increases to 6.40°, the pressure coefficient slightly increases in magnitude. That is, the pressure coefficient decreases and there is lower pressure over the upper surface of the wing. The suction peak increases on the two inboard stations while the center pressure row sees reduced suction compared to its neighbors. This is not in accordance with the flow visualization imagery, as this region near midspan showed reduced separation, which would manifest as a higher suction peak for this row. It is possible that this increased peak was not collected due to a lack of a leading-edge pressure tap. No firm conclusion can be made for either case with the data presented here.

As α increases to 8.46° and 10.50°, the pressure coefficient over the four outboard pressure rows shows the effect of flow separation (reduced suction and little variation in C_p with chordwise location). The effect is most prominent for $\alpha = 10.50°$. However, the pressure coefficients in the root-most row show continued increase in suction and local lift as α increases. The changes that occur with increasing α are more gradual than the clean case. As the wing

begins to unload at high α due to separation on the outboard wing, it is seen in Fig. 4.3 that the change in C_m with α becomes positive at approximately $\alpha = 7.5°$. Again, this coincides with the onset of separation seen in the surface pressure coefficient data, which would suggest the effects of separation setting in between $\alpha = 6.40°$ and $\alpha = 8.46°$. In this regard, the surface pressure coefficient data agrees very well with the flow visualization and force balance data.

4.2.5 Wake Survey Data

The streamwise velocity deficit data were gathered using the wake survey technique on the swept wing with the 3D smooth ice shape at $\alpha = 4.30°$ and $6.40°$. Overall, these wakes are much thicker than for the clean wing. There are also several distinct features seen in the wake for the 3D smooth shape case that is not seen in the clean wake. For $\alpha = 4.30°$, for a spanwise region of y/b = 0.5 to y/b = 0.6, the wake is noticeably thinner than the rest of the wake. This region corresponds to the region of reduced separation seen in the flow visualization data at the same α. There is a larger velocity deficit in the middle of the wake compared to the clean wing as well. This larger deficit, combined with a thicker wake, accounts for the increased drag of the 3D smooth shape compared to the clean wing.

At $\alpha = 6.40°$, two large wake features are observed at spanwise stations just outboard and inboard of y/b = 0.6, corresponding to the separation regions seen in the oil flow visualization and thus interpreted to be large vortices shed in to the wake. The wake in these regions has grown very thick, and the cross-flow vectors show an appreciable amount of cross-flow in these regions. There is a possible link between the changing geometry of the ice shape, seen in Fig. 4.4, and these features. The local-cross section becomes more streamline from y/b = 0.3 to y/b = 0.5, but slightly less streamline from y/b = 0.5 to y/b = 0.7. A change in the leading-edge geometry will alter the local flowfield considerably, but without more detailed data directly behind the ice shape, nothing can be said for certain regarding the effect of local geometry on local aerodynamics over this wing.

The spanwise lift and drag coefficients for $\alpha = 4.30°$ and $\alpha = 6.40°$ for the 3D smooth

maximum scallop ice shape are shown in Fig. 4.18. There is waviness in the spanwise distribution for both the sectional lift and sectional drag coefficients. These features coincide with the large vortices shed into the wake seen in the streamwise velocity deficit data for $\alpha = 6.40°$, as well as with the separation regions seen in both the mini-tuft and oil flow visualization data. For y/b less than 0.5, there is little correlation between local sectional drag coefficient maxima and local sectional lift coefficient. This is because most of the drag in this region is caused by profile drag. However, for y/b greater than 0.5, there are peaks in the local sectional lift and drag coefficients near the same y/b. The increased vorticity in this region due to higher relative loading of the outboard section of the wing would increase both induced drag and lift. Thus, the sectional induced drag coefficient in these regions is non-negligible, and the increase in total sectional drag coefficient is caused by both profile drag and vortex-induced drag and thus correlates more closely to the changes in sectional lift coefficient.

4.2.6 Evolution of Leading-Edge Vortices

Figure 4.19 shows a composite image of the growth of the leading-edge vortices for the 3D smooth maximum scallop ice shape for several α. At $\alpha = 2.20°$, there is a small vortex near the leading-edge in the midspan and outboard regions of the wing. The incoming flow separates around the ice shape and reattaches further downstream. On the upstream side of the reattachment line, particles move toward the leading-edge where they encounter a high pressure gradient region and form a weak vortex. This vortex moves toward the wing tip due to spanwise flow over the wing. The particles downstream of the attachment line move slightly toward the wing tip due to the spanwise component of velocity, but then the streamwise component of free stream velocity overcomes the spanwise component and the particles flow almost parallel to the chord. As α increases to 4.30°, the attachment line is moved further downstream, increasing the radius of the leading vortex. In addition, the leading-edge vortex is formed closer to the wing root, but its termination is similar to that of the vortex formed at $\alpha = 2.20°$. The vortices formed over the wing surface at $\alpha = 6.40°$

are different than those at lower α. There are four different vortices over the wing surface at this α and only one terminates near the wing tip. The other three terminate over the wing surface inboard of the wing tip likely due to the large pressure gradient over the wing surface caused by spanwise flow. At $\alpha = 6.40°$, the flow over the wing surface is on the verge of complete separation, as seen by the sporadic vortices and their termination over the surface. The radius of the vortices at this angle is quite large. For $\alpha = 7.44°$, the attachment line has moved to mid-chord and vanishes prior to reaching the wing tip. Total flow separation occurs for most of the midspan and outboard regions of the wing.

4.2.7 3D Smooth Maximum Scallop Aerodynamics Summary

For this *Re* and *M* combination, the 60-grit roughness did not have a large effect on the aerodynamic performance of the wing with the 3D smooth maximum scallop ice shape attached. Force balance data showed gradual changes in the aerodynamics up to approximately $\alpha = 6°$, after which the changes became more drastic. C_L decreased nonlinearly and C_D increased nonlinearly for α greater than 6°. The inflection point on the C_m curve, indicating usable lift, was about 4.5° lower for the 3D smooth shape than the clean wing. Mini-tuft imagery and oil flow visualization imagery showed multiple regions of flow separation at much lower α than for the clean wing. This separation begins at $\alpha = 6.40°$ for the 3D smooth shape. This gives way to massive amounts of separation over, approximately, the outboard 70% of the wing at $\alpha = 8.46°$ and continues to move inboard for higher α. This trend is backed by the upper-surface C_p data and wake survey data. The wake survey data shows large vortices being shed from this separation regions into the wake as well. The evolution of the leading-edge vortices for the 3D smooth shape showed thin vortices at low α give way to multiple, larger vortices at moderate α until separation begins to dominate around $\alpha = 7.44°$.

4.3 High-Fidelity Maximum Scallop

The high-fidelity maximum scallop ice shape has 3D features that significantly alter the aerodynamics of the wing, even compared to the 3D smooth maximum scallop shape. These

horn shapes protrude from the leading-edge and are not constant across the span of the wing. Note that the interpolation process used to create the full-span leading-edge ice shape does cause the ice shape to have some repetition in its general shape, though this is not a perfect replication with span. This geometry variation combined with the aerodynamic complexity of the clean swept wing causes the high-fidelity maximum scallop shape (hereafter referred to as the high-fidelity shape) to be one of the more detrimental icing cases investigated in this research effort.

4.3.1 Force Balance Data

The aerodynamic performance shown in Fig. 4.3 is now considered for the high-fidelity shape. The high-fidelity maximum scallop shape lift performance is dissimilar to the 3D smooth shape and the clean wing. The lift coefficient is lower for the high-fidelity shape than all other cases for α greater than 2°. The lift curve becomes nonlinear significantly earlier than the 3D smooth shape, diverging from the 3D smooth shape lift-curve at approximately $\alpha = 2°$. C_L changes gradually, similar to the 3D smooth shape case. It does not experience a sharp peak like the clean wing case. The trend for C_m for the high-fidelity shape matches the trend for C_L; the C_m curve for the high-fidelity shape diverges from the 3D smooth shape curve at approximately $\alpha = 2°$. An interesting feature of the curve is that the minimum of the C_m curve is at higher α than the 3D smooth shape by about 1°. However, because the total C_L for the high-fidelity shape is lower than for the 3D smooth shape, this does not equate to a higher usable lift for the high-fidelity shape. In fact, the usable lift coefficient in each case is similar (approximately 0.68 for the 3D smooth shape versus 0.65 for the high-fidelity shape). The drag coefficient is much higher for the high-fidelity shape as compared to the 3D smooth for an α range of $-6°$ to 6°. For α between 6° and 11.5°, the drag for the high-fidelity shape is lower than the 3D smooth shape. At these higher α, lift-induced drag becomes more important when compared to profile drag or lower α. In this range, the 3D smooth shape experienced large amounts of separation near the leading edge. This separation causes a large amount of drag on the wing. Thus, it is likely that the high-fidelity shape is not experiencing

the same amount of separation, and overall must produce different aerodynamic phenomena, compared to the 3D smooth shape. This notion will be explored in the following sections.

4.3.2 Mini-Tuft Imagery

Mini-tuft imagery for the high-fidelity maximum scallop ice shape case at $\alpha = 4.27°$, $\alpha = 6.35°$, $\alpha = 8.42°$, and $\alpha = 10.47°$ is shown in Fig. 4.20. These are nominally the same angles of attack as for the 3D smooth mini-tuft images. At $\alpha = 4.27°$, the high-fidelity shape flow is somewhat similar to the 3D smooth shape at $\alpha = 4.30°$. The tufts are all aligned with the freestream in this case, whereas there was some separation effect was seen near the midspan of the wing, though the rest of the wing showed flow aligned with the freestream for the 3D smooth shape, as it is here for the high-fielity shape. As α increases to 6.35°, the differences between the mini-tuft data for the high-fidelity maximum scallop ice shape and the 3D smooth maximum scallop ice shape are more apparent. On the high-fidelity maximum scallop ice shape, tufts near the midspan leading-edge of the wing are indicative of the initiation of separation in this region. However, the 3D smooth maximum scallop ice shape has many more moving tufts, as the separation at a comparable α is much larger for that case. There are also multiple, distinct separation regions seen in the 3D smooth case, whereas for the high-fidelity shape, there is only a single separation region near the midspan. The mini-tuft data for the high-fidelity shape at $\alpha = 6.35°$ is very similar to the 3D smooth shape at $\alpha = 4.30°$.

The mini-tuft imagery at $\alpha = 8.42°$ shows separation has occurred over a large portion of the outboard section of the wing. The separation region covers from a spanwise station of approximately y/b = 0.2 to the wing tip. Note that the inboard separation is near the trailing edge of the wing, while the outboard portion has separation over the entire local chord of the wing. There is also strong spanwise flow in the inboard section of the wing as well. The high-fidelity shape is exhibiting characteristics from both types of stall. This is unique for the high-fidelity shape. For $\alpha = 10.47°$, most of the flow over the wing separates. This is similar to the 3D smooth shape. In this flow regime, the ice shapes have less influence

over the flow. This is likely why the high-fidelity ice shape and the 3D smooth ice shape converge in C_D and C_m for near this α.

4.3.3 Oil Flow Visualization

Figure 4.21 shows oil flow visualization for $\alpha = 4.27°$ and $\alpha = 6.35°$ for the high-fidelity shape. The oil flow visualization looks very different than the 3D smooth images in Fig. 4.15. Extensive streamwise features, which Camello et al. [44] identified as streamwise vortices, are seen. These features are not present on the 3D smooth shape or the clean wing. While the features likely contain some streamwise vorticity, a different theory for these features is proposed here. The high-fidelity maximum scallop shape is highly 3D and contains ice scallops that repeat spanwise and are separated or connected by regions of thinner ice accretion. Cross-sections of these ice scallops at three spanwise locations are shown in Fig. 4.4. The ratio of the scallop width to the gap width as a function of span is given in Fig. 4.5. Regions where the ratio is greater than 1, such as between y/b = 0.36 and y/b = 0.5, is where the streamwise features disappear in the oil flow visualization for $\alpha = 6.35°$. For y/b less than 0.36, this ratio oscillates around approximately 1.2, and for y/b greater than 0.5, the ratio of scallop width to gap width is near or below 1. In these regions, the ice shape is not as "solid" to the oncoming flow as is the 3D smooth shape that was formed from the maximum extent or thicknesses on the measured scallop shape. As described by Camello et. al. [22] and in Chapter 2.3, the maximum scallop ice simulation tested was generated from three measured accretions of limited span and then interpolating was used to generate a shape between these stations. Thus, the pattern of scallops and valleys repeats across the span, changing slowly as it moves spanwise due to the interpolation process. The dark streamwise regions correspond to these valleys between some of the scallop protuberances and likely allow relatively high-velocity air to flow through the ice shape and, due to the high shear, scrub off the oil exposing the black wing surface below. Thus, they act something like "jets" generated through the ice simulation. The bright streamwise regions are regions of reduced shear between the jets. There is some evidence of the oil streaks merging as they flow downstream that may well be

the result of streamwise vortices, though more research is needed to fully characterize this very complex 3D flow in this region. There is also possible high-pressure air that stagnates underneath the ice shape just before the leading-edge of the wing that then moves through this gap. This high-pressure air would prevent the streamwise jets from mixing until far downstream of the ice shape. This flow feature partly responsible for the differences in the swept-wing aerodynamics of the high-fidelity shape versus the simpler 3D smooth shape. As α increases to 6.35°, oil flow visualization data indicates that the jet features are diminished near the midspan of the wing. This effect is possibly due to the change in geometry of the ice shape itself. Near the midspan of the high-fidelity maximum scallop ice shape, the ratio of scallop width to gap width increases to approximatley 2. This is plotted in Fig. 4.5. This geometry change, coupled with increased α, would reduce the flow through the gaps in the ice in favor of moving around the leading-edge ice accretion instead. This is evidenced by the existence of a flow separation region in the area where the jets disappear. The oil flow visualization shows a clear reattachment line from the separation region downstream of the ice shape. It is likely that the jets closer to the wing tip and near the root are preventing the flow from separating, as they would re-energize flow in this region by injecting higher energy flow. However, this energization would also make the boundary layer thick in these areas, increasing drag. It is possible as well that the added vorticity over the top surface of the wing from these jets is increasing the average pressure over the top surface of the wing, causing a decrease in lift. These effects would explain why, even though there is less leading-edge spearation for the high-fidelity maximum scallop shape compared to the 3D smooth shape, there is higher drag and lower lift for the high-fidelity shape. However, given the complexity of the wing geometry, there are likely several other factors at play beyond the jets alone. Further evidence of the flow separation and reattachment near midspan is the apparent beading and concentration of oil just aft of the ice shape and ahead of the reattachment line in Fig. 4.21 for $\alpha = 6.35°$. This beading represents the secondary separation line inside the overall leading-edge separation vortex. Indicative of the complex flow in this region, the line appears to be interrupted periodically, possibly by some small flow through the ice shape.

4.3.4 Surface Pressure Data

Figure 4.22 shows the C_p distribution data for $\alpha = 4.27°$, $\alpha = 6.35°$, $\alpha = 8.42°$, and $\alpha = 10.47°$ for the high-fidelity shape. Note that there is no pressure data taken within the ice shape itself, similar to the 3D smooth shape case. For $\alpha = 4.27°$, the magnitude of the peak pressure coefficient aft of the leading edge is lower than both the clean case and the 3D smooth shape case. This coincides with C_L data that show a lower lift coefficient for the high-fidelity maximum scallop shape than either the 3D smooth shape or the clean wing. The magnitude of the pressure coefficient increases as α increases to 6.35°. As there are no pressure taps in the ice shape, the small leading-edge separation that exists at this α is not picked up by the C_p distribution data.

The pressure coefficient for $\alpha = 8.42°$ shows reduced leading-edge suction on the outboard sections foreshadowing the coming tip stall. At this α the 3D smooth shape showed significantly reduced lift and constant pressures over the tip section indicating tip stall as seen in the tufts. The inboard sections for the high-fidelity shape still retian some of the suction peak seen at lower α. This is similar to to the 3D smooth shape. The root of the wing is harder to stall likely because of the boundary-layer suction effect caused by spanwise flow moving from root to tip as well as a larger leading-edge radius at the root of the wing decreasing the local pressure gradient near the leading edge. For $\alpha = 10.47°$, the pressure coefficients between the two fidelities of the maximum scallop shape are nearly identical in the outboard and midspan regions. The pressure coefficients nearest the root still have a distinct peak in the 3D smooth case that does not exist for the high-fidelity shape case, which is likely why the 3D smooth shape case has a higher lift coefficient at this α and above. As the outboard and midspan sections of the wing are already experiencing stall for both the 3D smooth shape and the high-fidelity shape, the difference in aerodynamic performance is likely a function of the phenomena at the wing root. The increased suction peak at the root for the 3D smooth shape compared to the high-fidelity shape also explains the why the change in $\frac{\delta C_L}{\delta \alpha}$ is more positive for the 3D smooth case than it is for the high-fidelity case, as seen in Fig. 4.6. As

there is larger lift on the inboard of the 3D smooth shape, the center of pressure for this case shifts more toward the leading-edge, causing an unstable shift in pitching moment.

4.3.5 Wake Survey Data

The streamwise velocity deficit in the wake of the wing for the high-fidelity maximum scallop ice shape is shown in Fig. 4.23. For $\alpha = 4.27°$, the wake of the wing is consistent and thick, in contrast to the 3D smooth ice shape wake where the wake varied in thickness at different spanwise locations. The 3D smooth wake has a clear discontinuity near y/b = 0.6 possibly due to the change in ice shape geometry discussed earlier. There are vortices on either side of this discontinuity, evidenced by the cross-flow vectors that surround regions of low streamwise velocity. In general, the 3D smooth wake varies widely spanwise. The high-fidelity shape wake is very uniform spanwise and may be a result of the stabilizing tendencies of the jet/vortex flow produced by the scallops. The jets and vorticity would work to mix the flow over the wing and downstream of the trailing-edge, causing the flow uniformity seen in the wake survey data. The high-fidelity wake has more low-velocity flow in the wake as compared to the 3D smooth, reflective of the higher drag especially for the $\alpha = 4.27°$ case. At lower α, the losses the flow experiences moving through the scallop protuberances explain the lower wake velocity and higher drag. At higher α, this is probably balanced by the overall flow separation that eventually dominates the drag. At $\alpha = 4.27°$, but especially at $\alpha = 6.35°$, closely placed and periodic regions of high velocity loss are seen in the center of the wake. They appear in the middle of the wake from a spanwise station of approximately y/b = 0.5 to 0.9 for the low α wake and from approximately y/b = 0.7 to 0.95 for the higher α wake. It is attractive to explain these regions as a result of the streamwise features seen in the oil flow. However, the data presented in this study is not sufficient to resolve these features. This is an unfortunate restriction of test time, as increasing the spatial resolution of the wake survey would dramatically increase the time required to collect data. This is not generally economically feasible.

The spanwise distributions for sectional lift and drag coefficients for $\alpha = 4.27°$ and

$\alpha = 6.35°$ are shown in Fig. 4.24. These spanwise distributions are much less jagged than that of the 3D smooth case, similar to the difference in the streamwise velocity deficit data. There is slight jaggedness in these distributions at y/b = 0.55 for $\alpha = 6.35°$, which is not seen in other data. It is possible that this jaggedness, along with the periodic regions of high velocity loss seen in the streamwise velocity deficit data, are artifacts created by limitations of the wake survey system, chiefly spatial resolution of the data collected as well as unsteady effects that are unaccounted for in this analysis. The unsteady effects can be accounted for if a fast-response five-hole probe is used to collect this data. Some work in this vain has been done. This discussion is presented in Appendix B. There is also some jaggedness in the distribution for sectional drag coefficient for $\alpha = 6.35°$ near y/b = 0.9. This jaggedness is most likely due to the influence of the wing-tip vortex.

4.3.6 Evolution of Leading-Edge Vortices

A composite image of the growth of the leading-edge vortices for high-fidelity maximum scallop ice shape for several α is shown in Fig. 4.25. The first separation vortex forms at $\alpha = 6.35°$ and it is similar to the 3D smooth shape, except that it extends further toward the wing root. The leading-edge vortex first forms at higher α than both the clean wing and the 3D smooth case. This is possibly due to the existence of valleys between the ice scallop protuberances. These gaps create a high-energy, jet-like flow that prevents separation and vortex formation at low-to-moderate α by re-energizing the boundary layer fluid. Though these gaps may prevent vortex formation and may delay flow separation, there is likely a loss of total pressure associated with flow moving through these gaps. There is some evidence of this in the streamwise velocity deficit diagram in Fig. 4.23, as these losses would likely cause a thicker wake at low-to-moderate α compared to the 3D smooth shape, which is generally the case. For $\alpha = 7.39°$, the leading-edge vortex increases in size, however no additional chord is covered by the vortex. The leading-edge vortex does not extend as far outboard as the vortex at $\alpha = 6.35°$. Tip separation also becomes apparent at this α, extending from the wing tip to a point on the span near where the leading-edge vortex at $\alpha = 6.35°$ swept off

the wing. This suggests a complex interaction between the leading-edge vortex and the wing tip vortex. The vortex likely does not extend inboard any further because of the streamwise jet features that are still present near the root of the wing. For $\alpha = 8.42°$, the vortex has extended inboard of the Yehudi break and sweeps off the wing near y/b = 0.45, much more inboard than the leading-edge vortices at lower α. This corresponds well to the mini-tuft imagery for the high-fidelity shape at the same α, shown in Fig. 4.20. In the mini-tuft imagery, separation is seen over the entire chord of the wing for y/b > 0.5 at $\alpha = 8.42°$.

4.3.7 Summary of High-Fidelity Maximum Scallop Aerodynamics

The flowfield associated with the high-fidelity maximum scallop ice shape differs greatly from the flowfield of the clean wing and the 3D smooth maximum scallop ice shape. The existence of the ice shape causes a decrease in lift coefficient, an increase in drag coefficient, and a nose-up pitching moment coefficient compared to the clean case. The high-fidelity case generates larger penalties in lift and in drag below $\alpha = 10°$. When comparing changes with α, the changes that occur in the high-fidelity maximum scallop ice shape case are more gradual than the clean case. Flow separation on the wing occurs from outboard to inboard as α increases. The gaps that exist in the high-fidelity maximum scallop ice shape cause the aerodynamics to differ from that of the 3D smooth maximum scallop ice shape. These gaps seem to cause streamwise jets to form over the entire wing at low α, and in the outboard and inboard regions at moderate α. These jets likely delay leading-edge separation relative to the 3D smooth case. When these jets disappear near the midspan at moderate α and above, possibly due to a change in the ice shape geometry, a leading-edge separation region forms. There is some evidence that these jets are manifesting in the wake as small pockets of decreased streamwise velocity perhaps from generated vortices. Thus, the 3D smooth ice shape is not conservative in the aerodynamic penalties experienced by the wing relative to the very complex, high-fidelity case. This is explained by the result of the flow through the valleys or gaps in the ice scallop shape that influence the overall aerodynamics. However, this is one comparison, on one wing geometry, at low *Re* and thus extrapolation to other cases

is not possible. Future tests are planned to explore this using simple ice shape geometries modeling various gap sizes and spacing at low and moderate Re to better understand this effect.

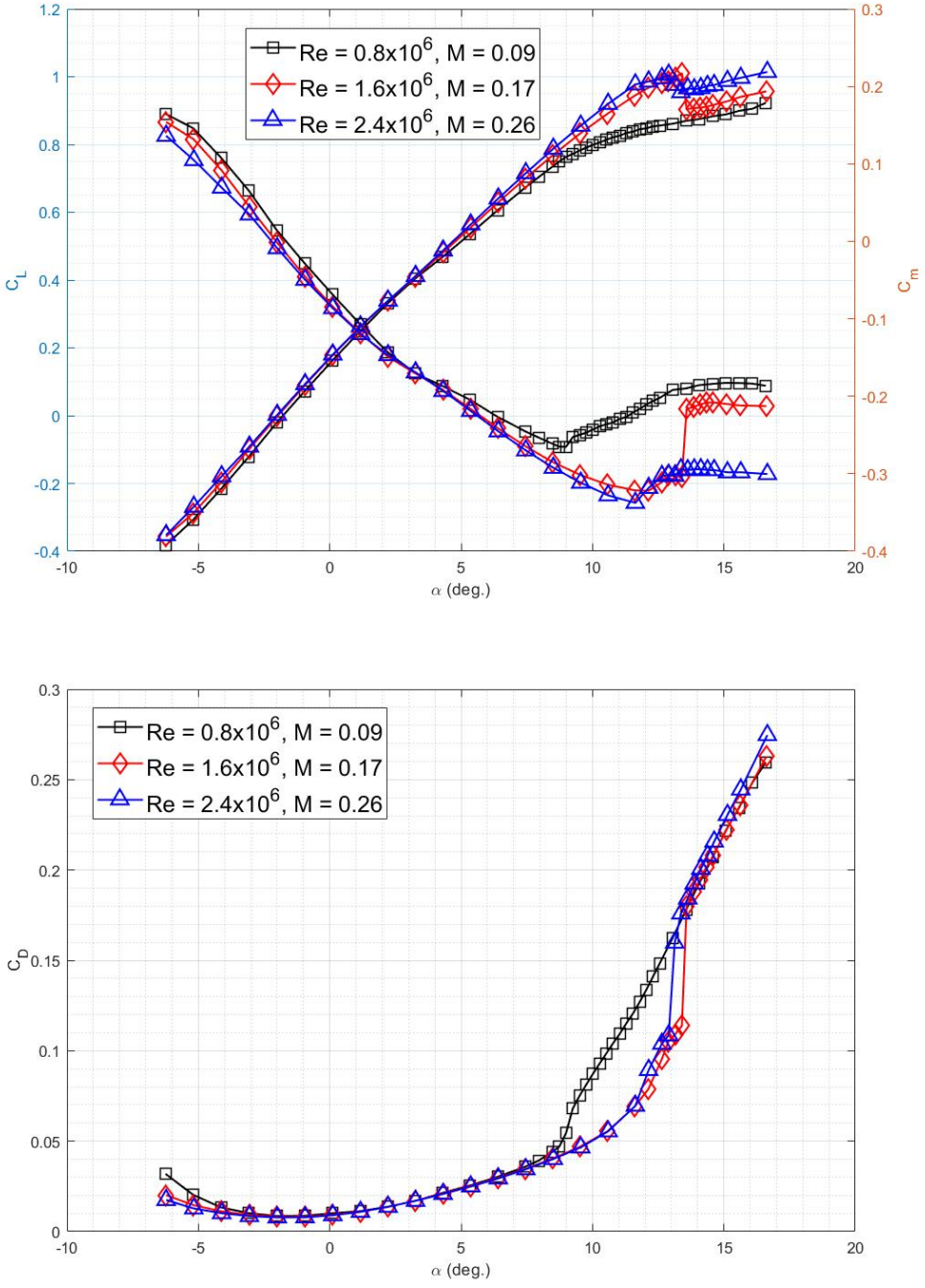

Figure 4.1: Comparison of C_L and C_m (top) as well as C_D (bottom) versus α for the clean wing for the three Re and M combinations tested.

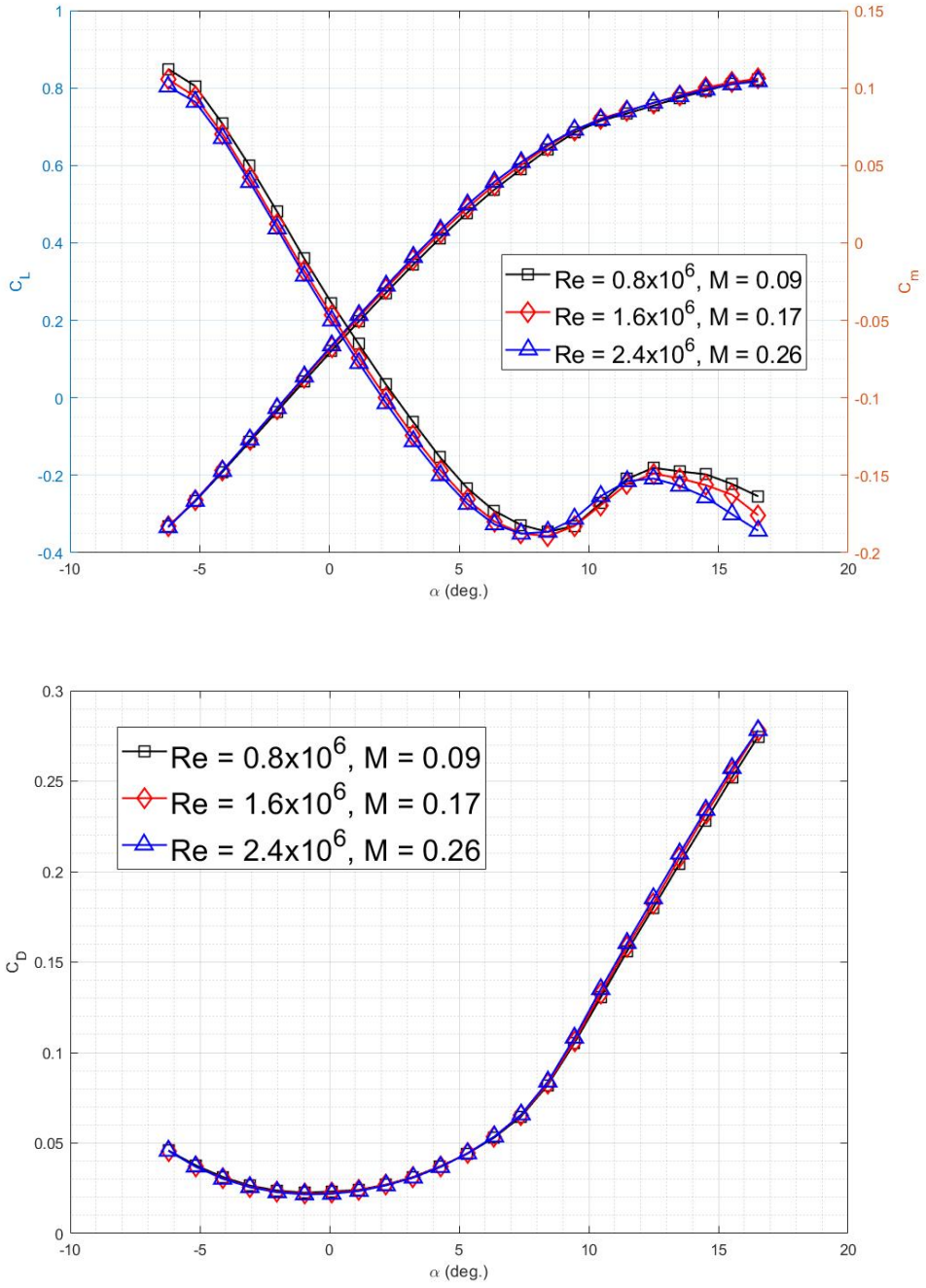

Figure 4.2: Comparison of C_L and C_m (top) as well as C_D (bottom) versus α for the high-fidelity maximum scallop shape for the three Re and M combinations tested.

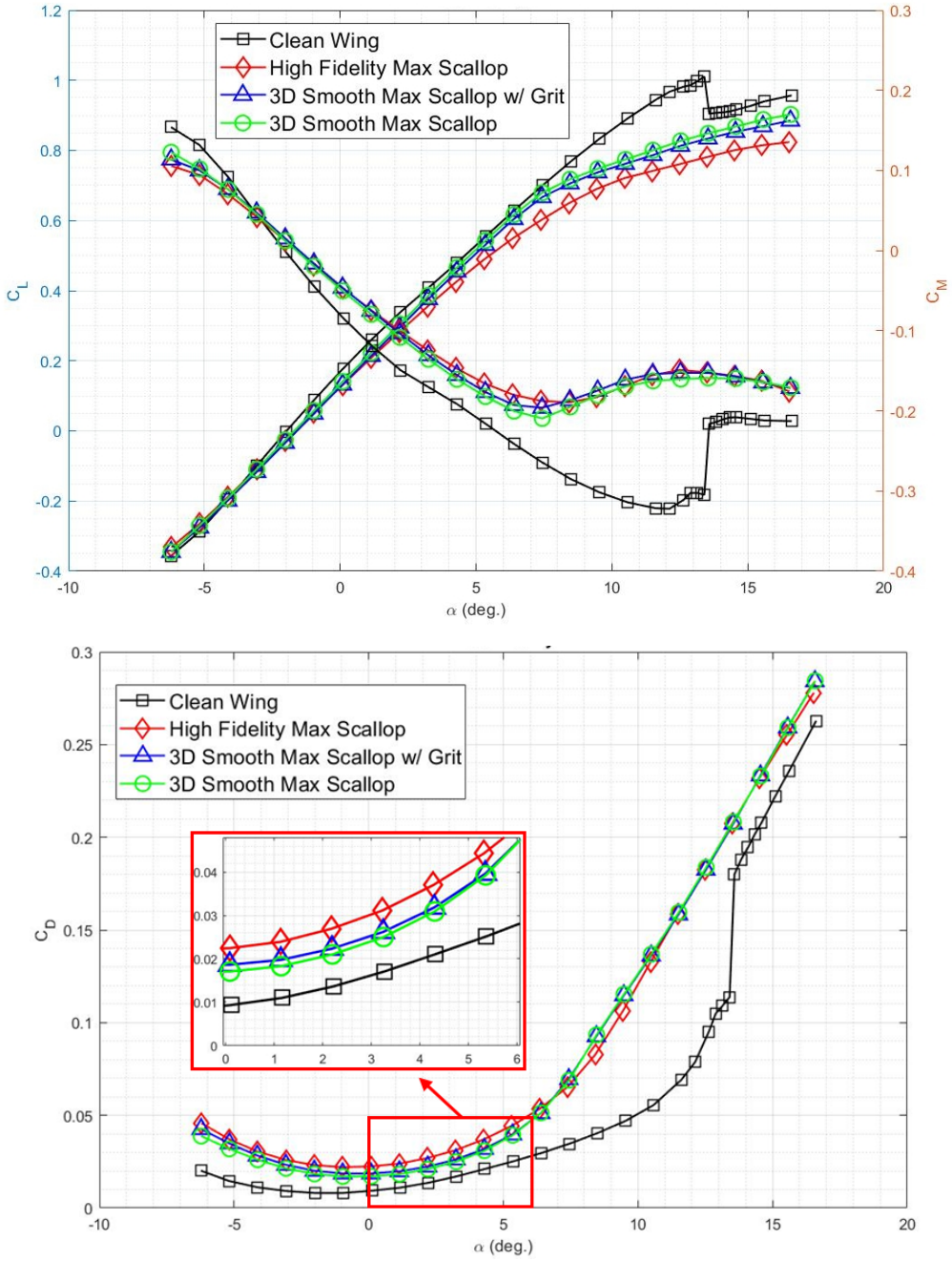

Figure 4.3: Comparison of C_L and C_m (top) as well as C_D (bottom) versus α for the clean wing and all tested fidelities for the maximum scallop shape for $Re = 1.6 \times 10^6$ and $M = 0.17$.

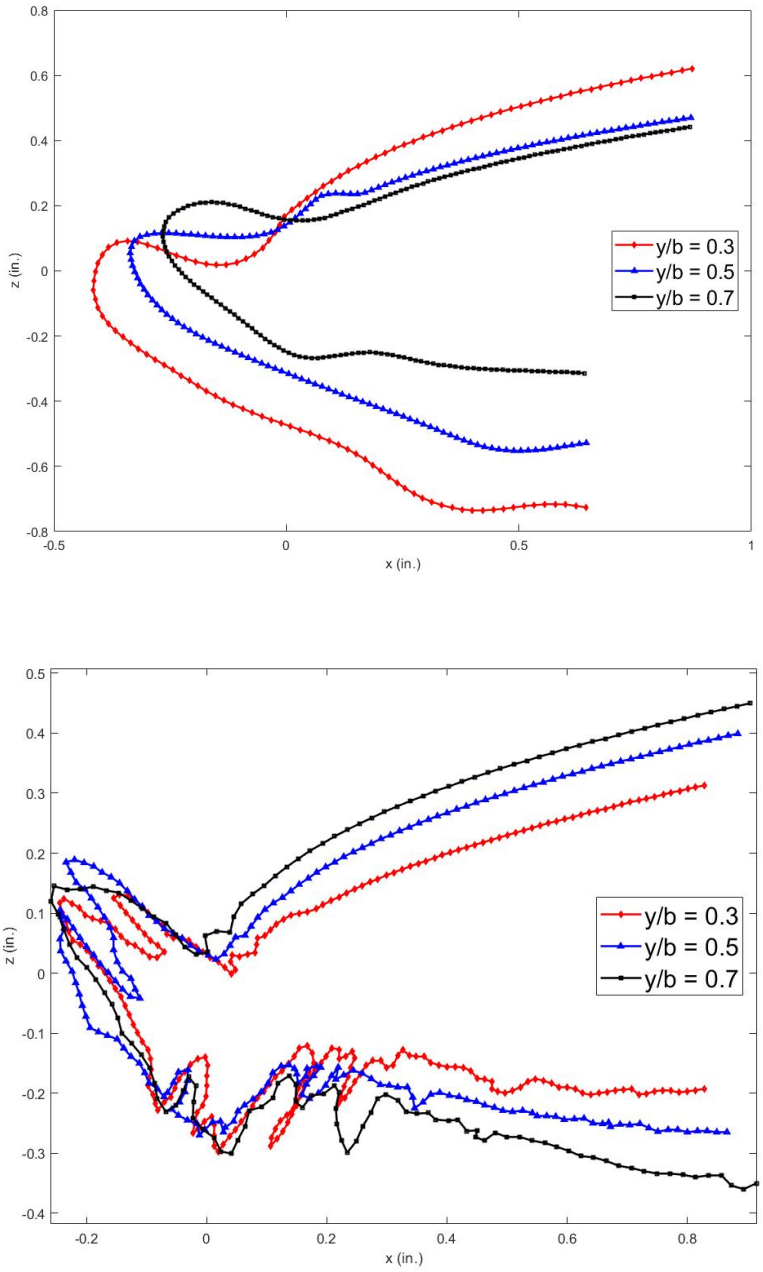

Figure 4.4: Cross-sections of the leading-edge including leading-edge ice for three spanwise stations is shown for the 3D smooth maximum scallop shape (top) and the high-fidelity maximum scallop shape (bottom).

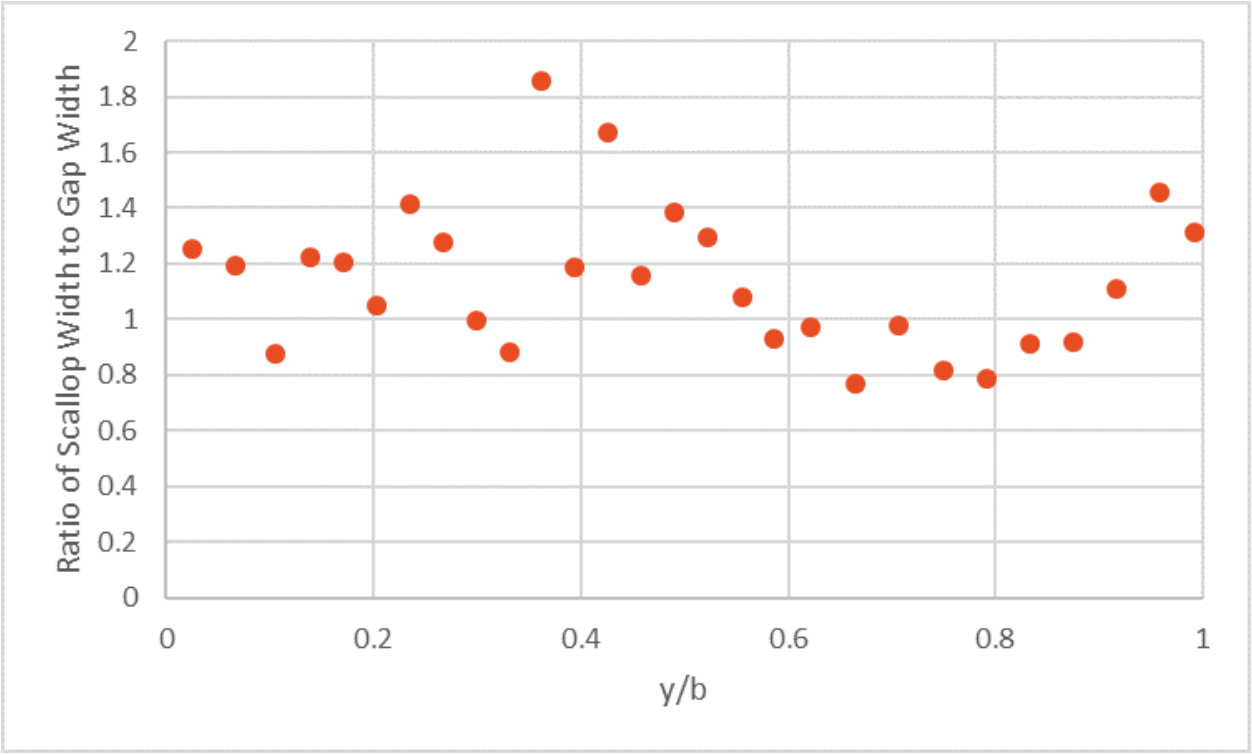

Figure 4.5: The ratio of scallop width to gap width between the scallop features on the high-fidelity maximum scallop shape is plotted versus span.

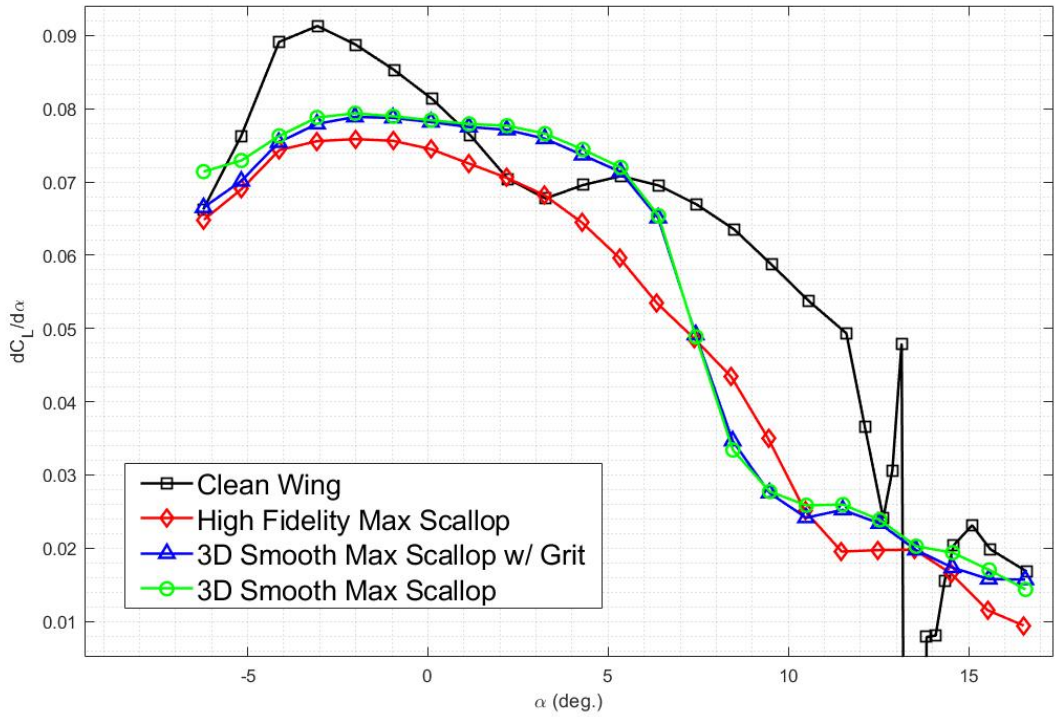

Figure 4.6: $\frac{\delta C_L}{\delta \alpha}$ is shown as a function of α for all maximum scallop icing cases and the clean wing, $Re = 1.6 \times 10^6$, $M = 0.17$.

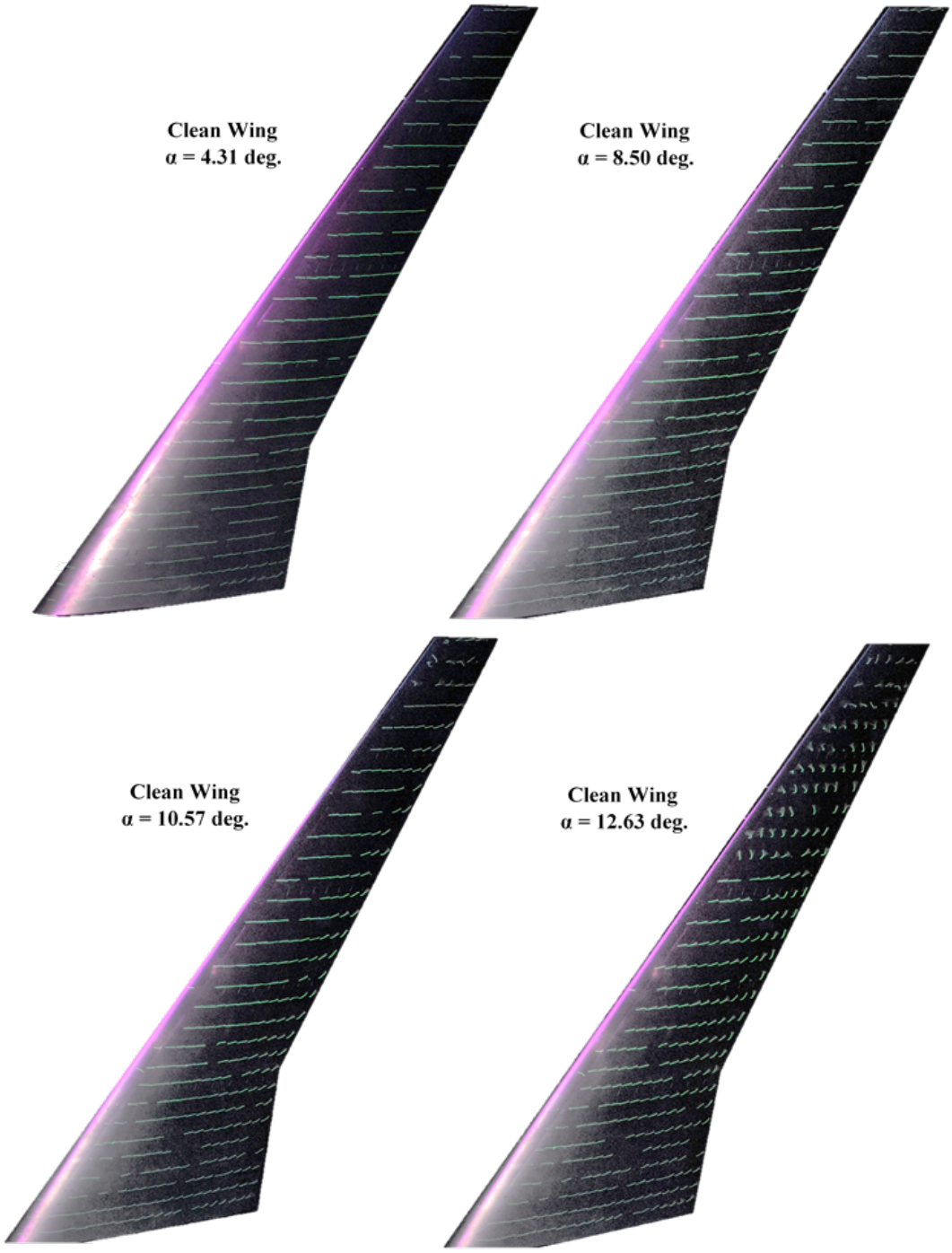

Figure 4.7: Mini-tuft imagery for the clean wing for $\alpha =$ 4.31°, 8.50°, 10.57°, and 12.63°, Re $= 1.6 \times 10^6$, $M = 0.17$.

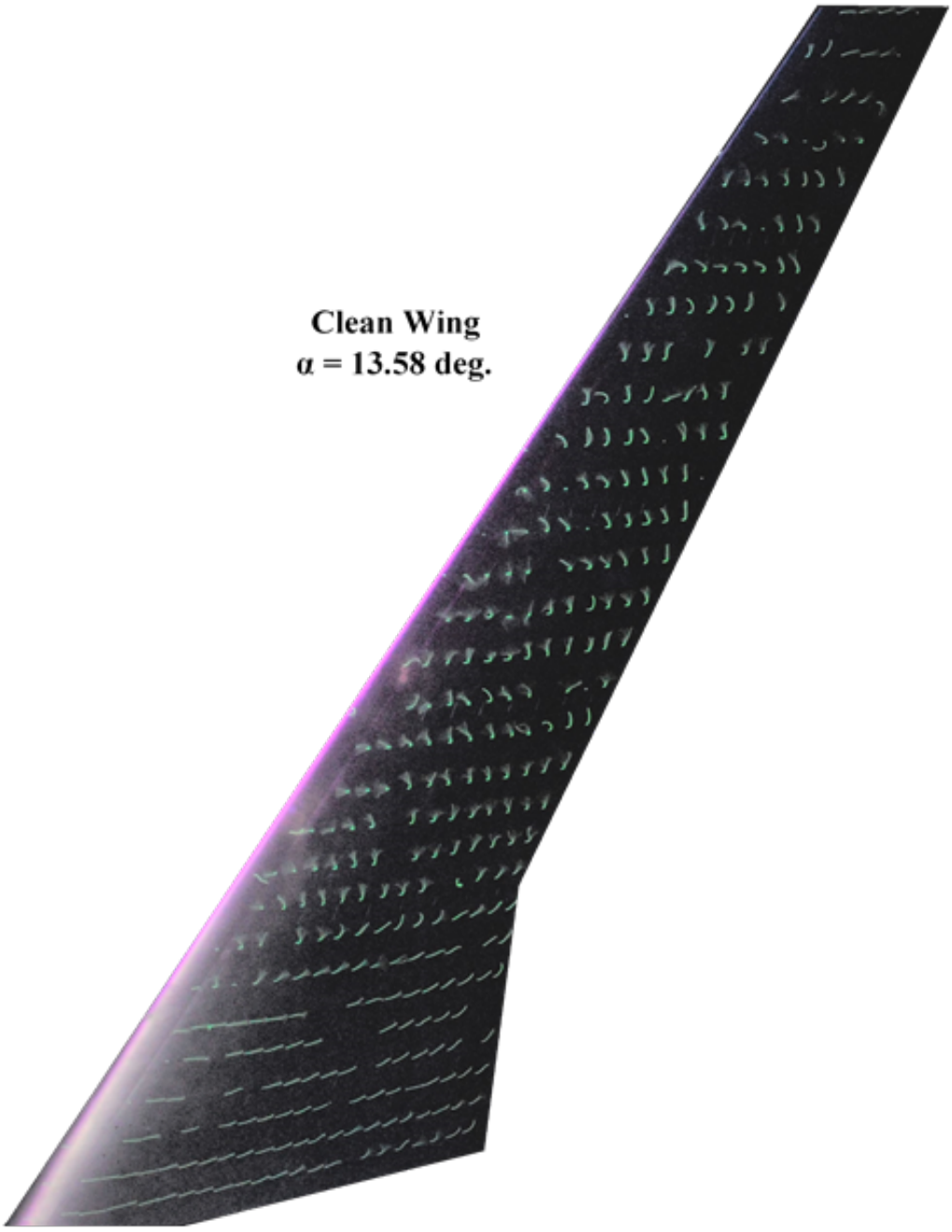

Figure 4.8: Mini-tuft imagery for the clean wing for $\alpha = 13.58°$, $Re = 1.6 \times 10^6$, $M = 0.17$.

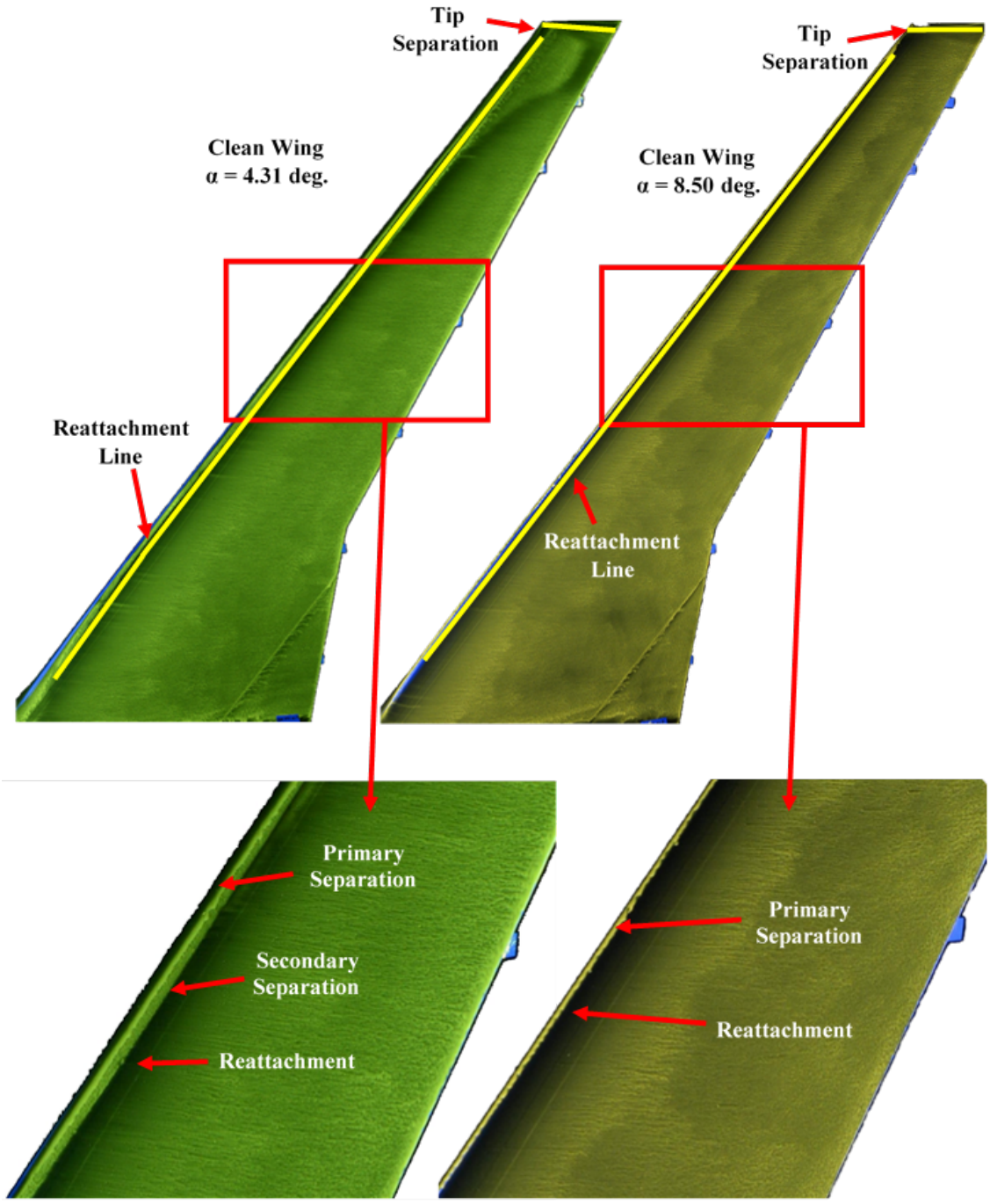

Figure 4.9: Oil flow visualization imagery is shown for the clean wing for $\alpha = 4.31°$ and $8.50°$, $Re = 1.6 \times 10^6$, $M = 0.17$.

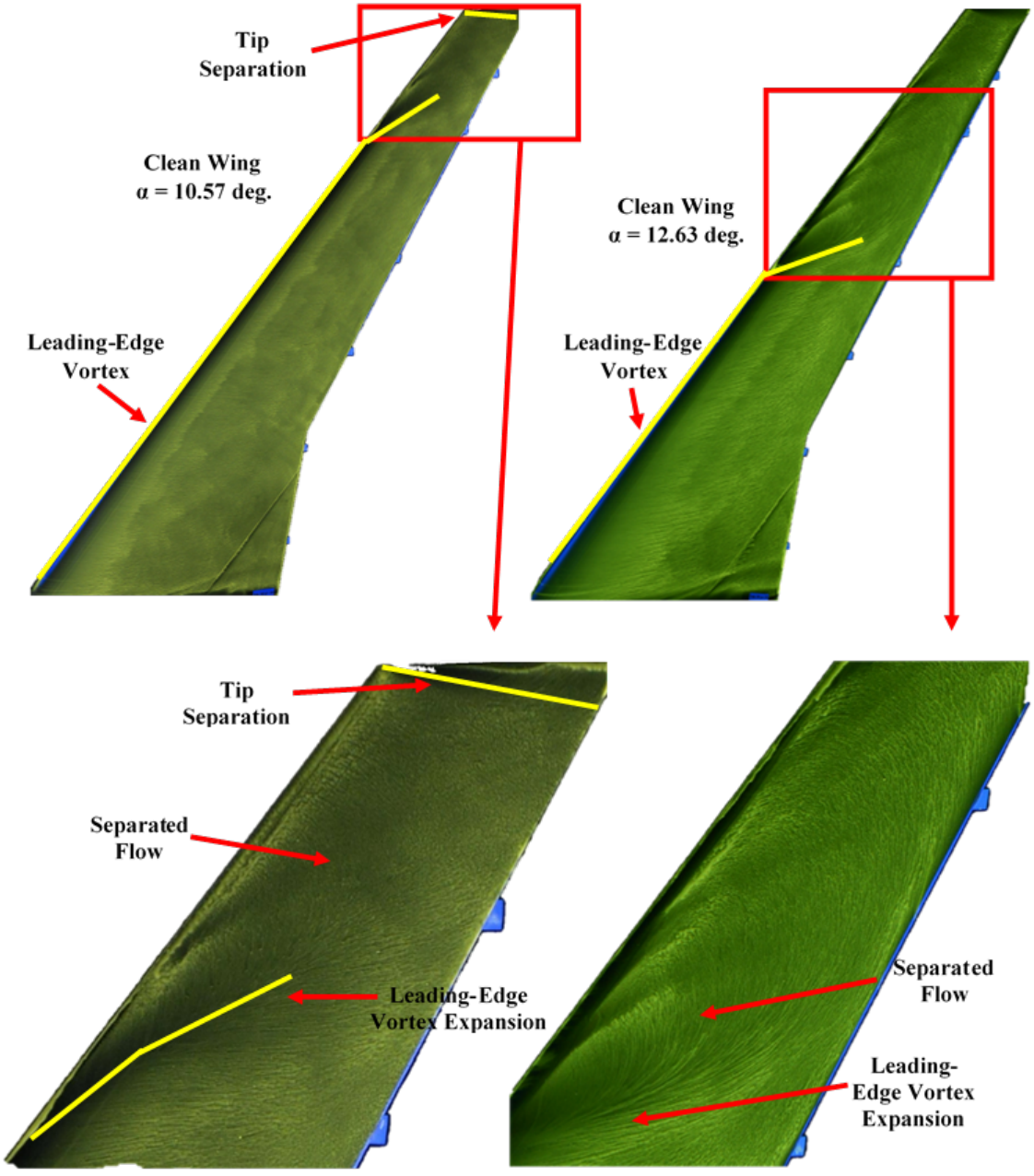

Figure 4.10: Oil flow visualization imagery is shown for the clean wing for $\alpha = 10.57°$ and $12.63°$, $Re = 1.6 \times 10^6$, $M = 0.17$.

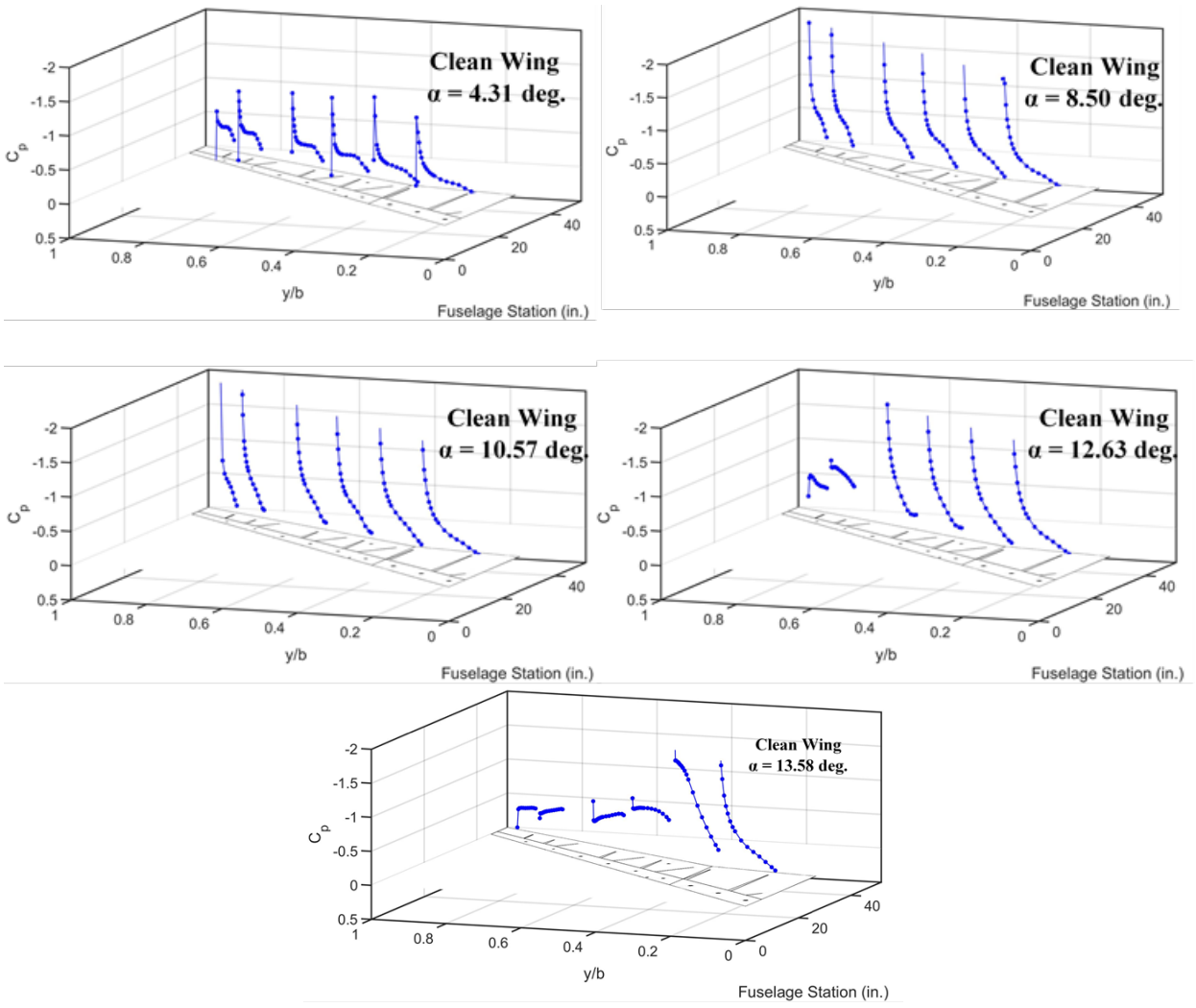

Figure 4.11: Surface pressure coefficient data is shown for the upper surface of the clean wing for $\alpha =$ 4.31°, 8.50°, 10.57°, 12.63°, and 13.58°, $Re = 1.6 \times 10^6$, $M = 0.17$.

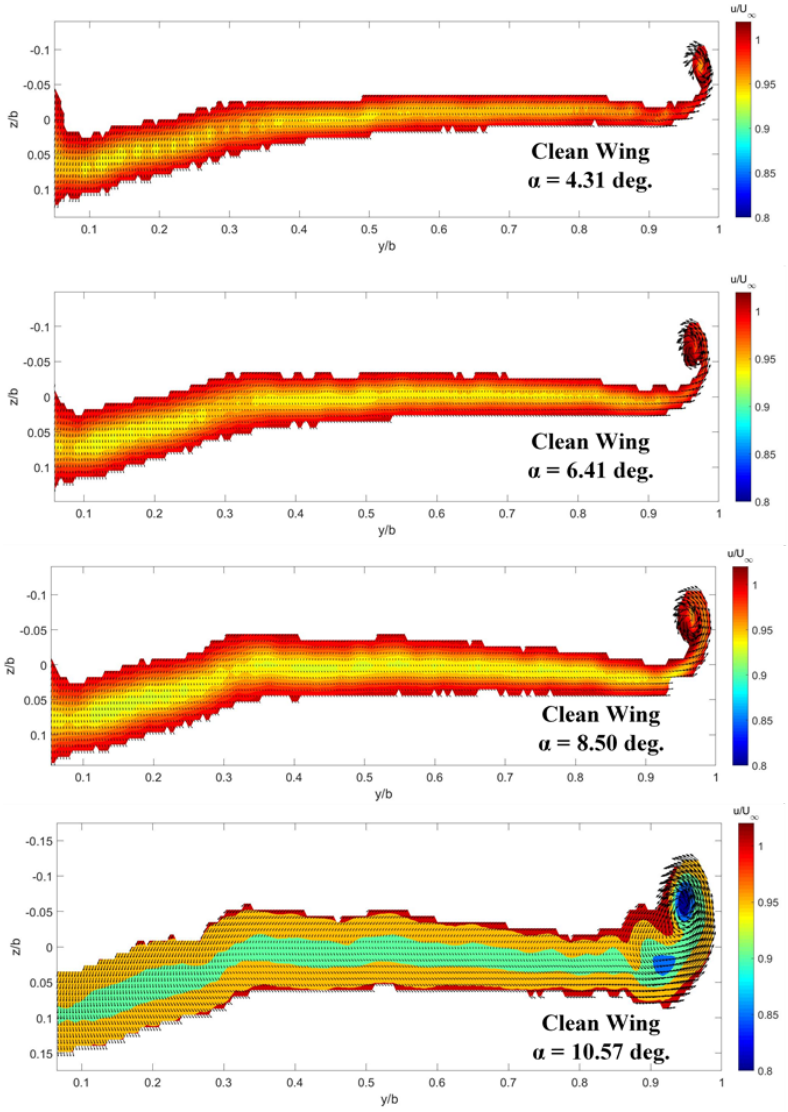

Figure 4.12: Streamwise velocity deficit in the wake plane is shown for the clean wing for $\alpha = \ 4.31°,\ 6.41°,\ 8.50°$, and $10.57°$, $Re = 1.6 \times 10^6$, $M = 0.17$.

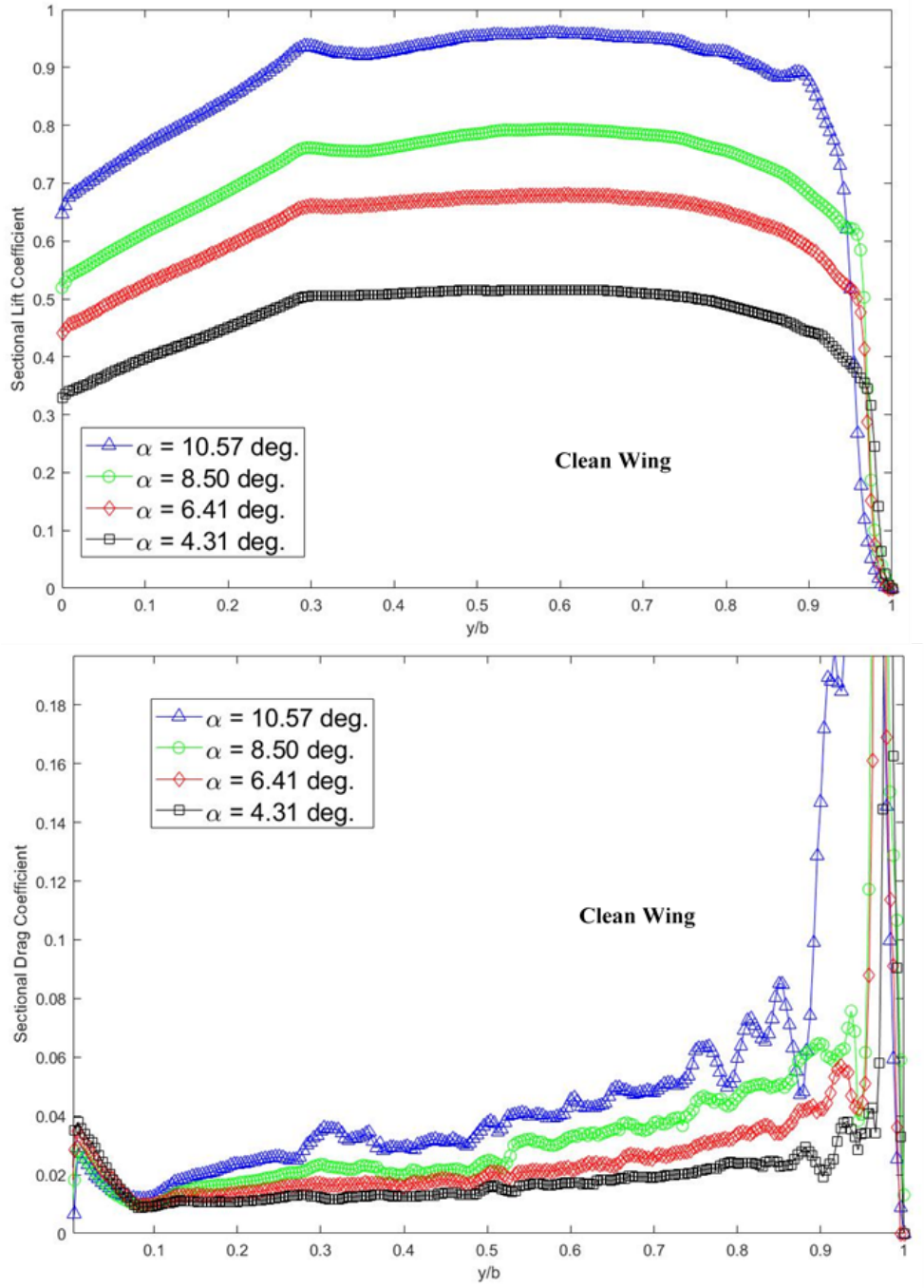

Figure 4.13: Sectional lift coefficient (top) and sectional drag coefficient (bottom) are plotted versus span for the clean wing for $\alpha = 4.31°,\ 6.41°,\ 8.50°$, and $10.57°$, $Re = 1.6 \times 10^6$, $M = 0.17$.

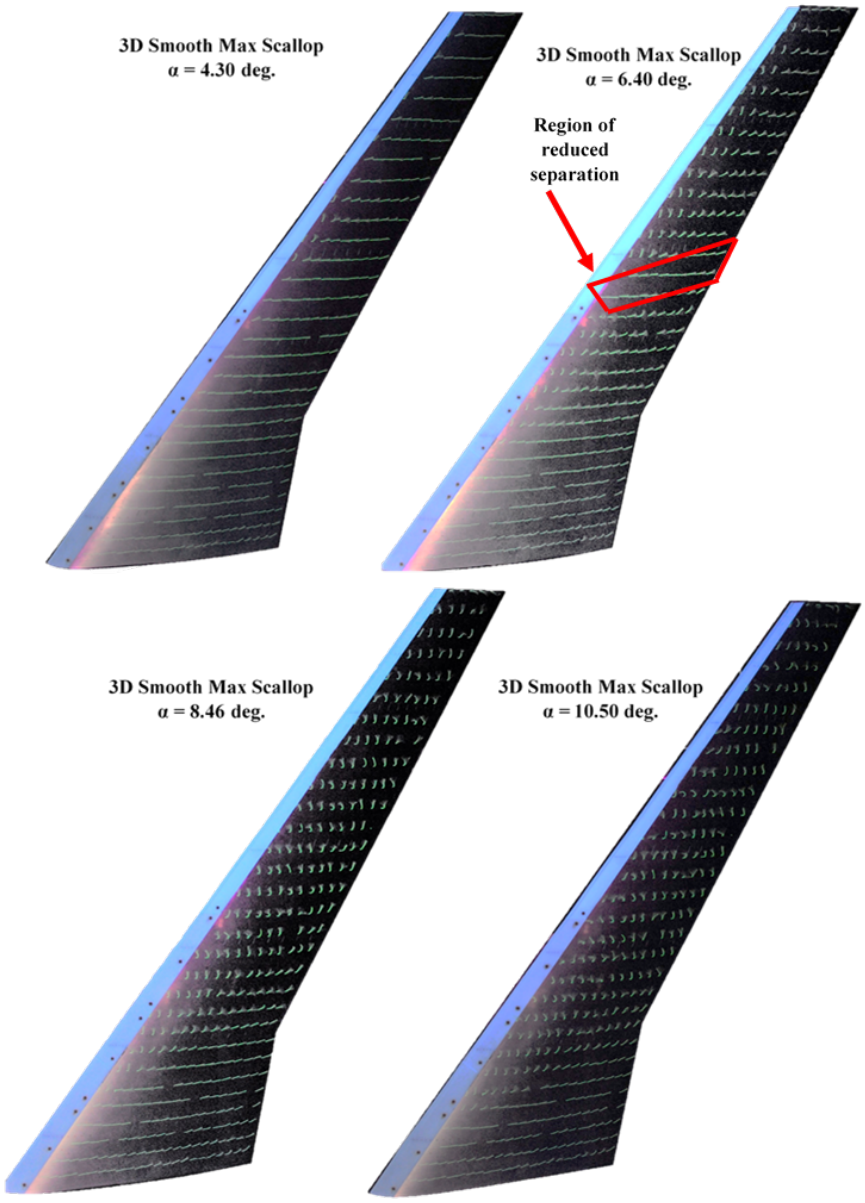

Figure 4.14: Mini-tuft imagery is shown for the 3D smooth maximum scallop ice shape for $\alpha =$ 4.30°, 6.40°, 8.46°, and 10.50°, $Re = 1.6 \times 10^6$, $M = 0.17$.

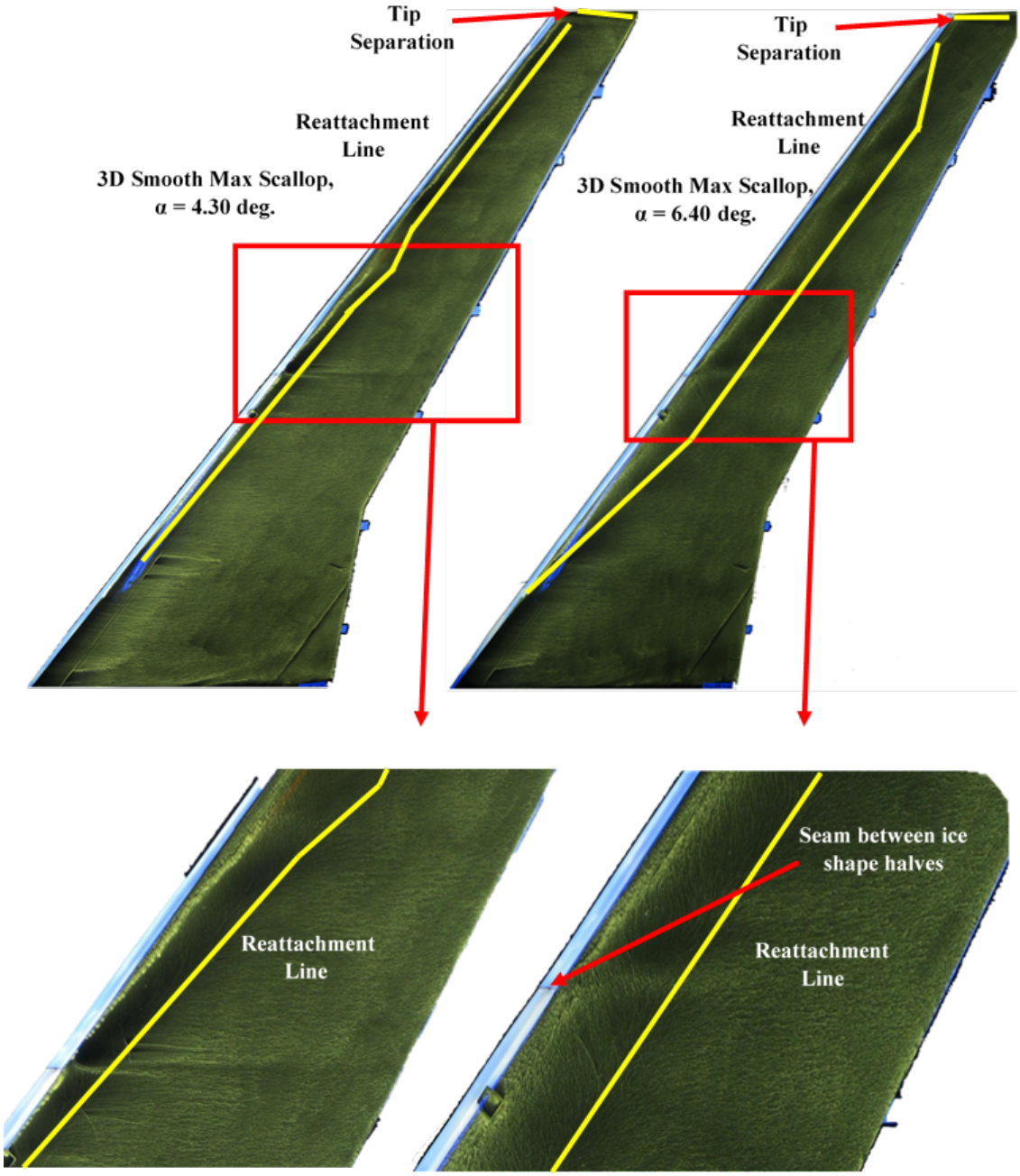

Figure 4.15: Oil flow visualization for the 3D smooth maximum scallop shape for $\alpha =$ 4.30° and 6.40°, $Re = 1.6 \times 10^6$, $M = 0.17$.

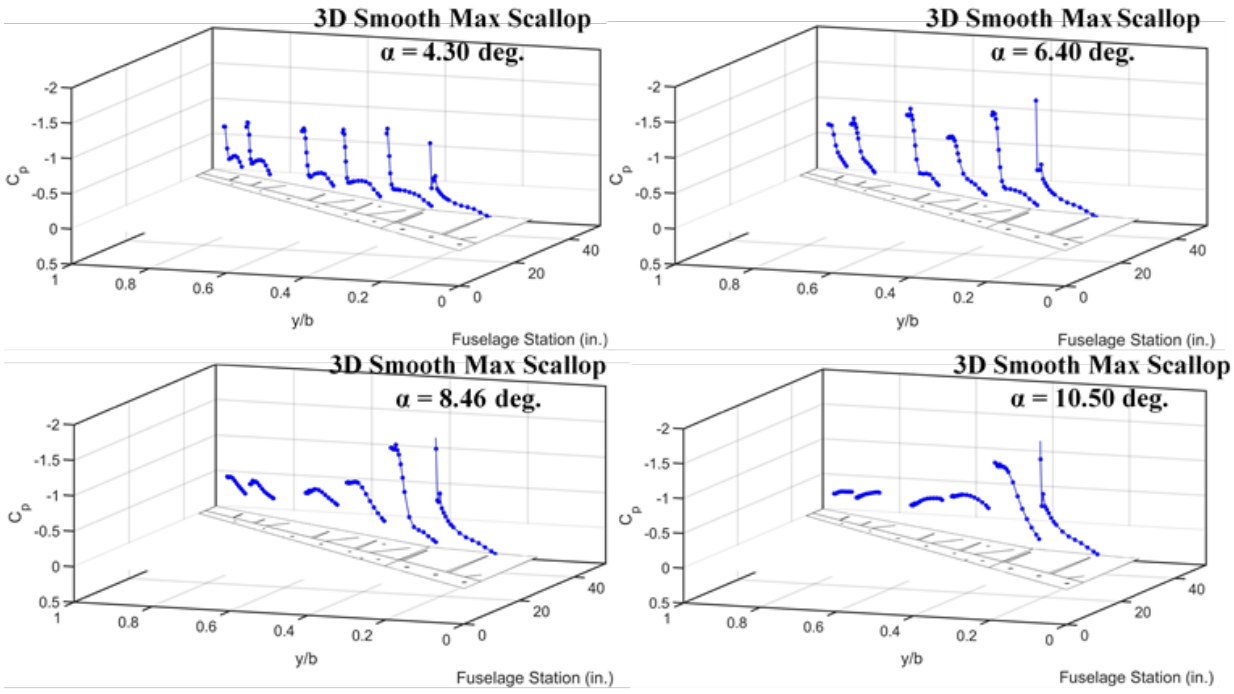

Figure 4.16: Surface pressure data for the upper surface of the wing for the 3D smooth maximum scallop shape for $\alpha =$ 4.30°, 6.40°, 8.46°, and 10.50°, $Re = 1.6 \times 10^6$, $M = 0.17$.

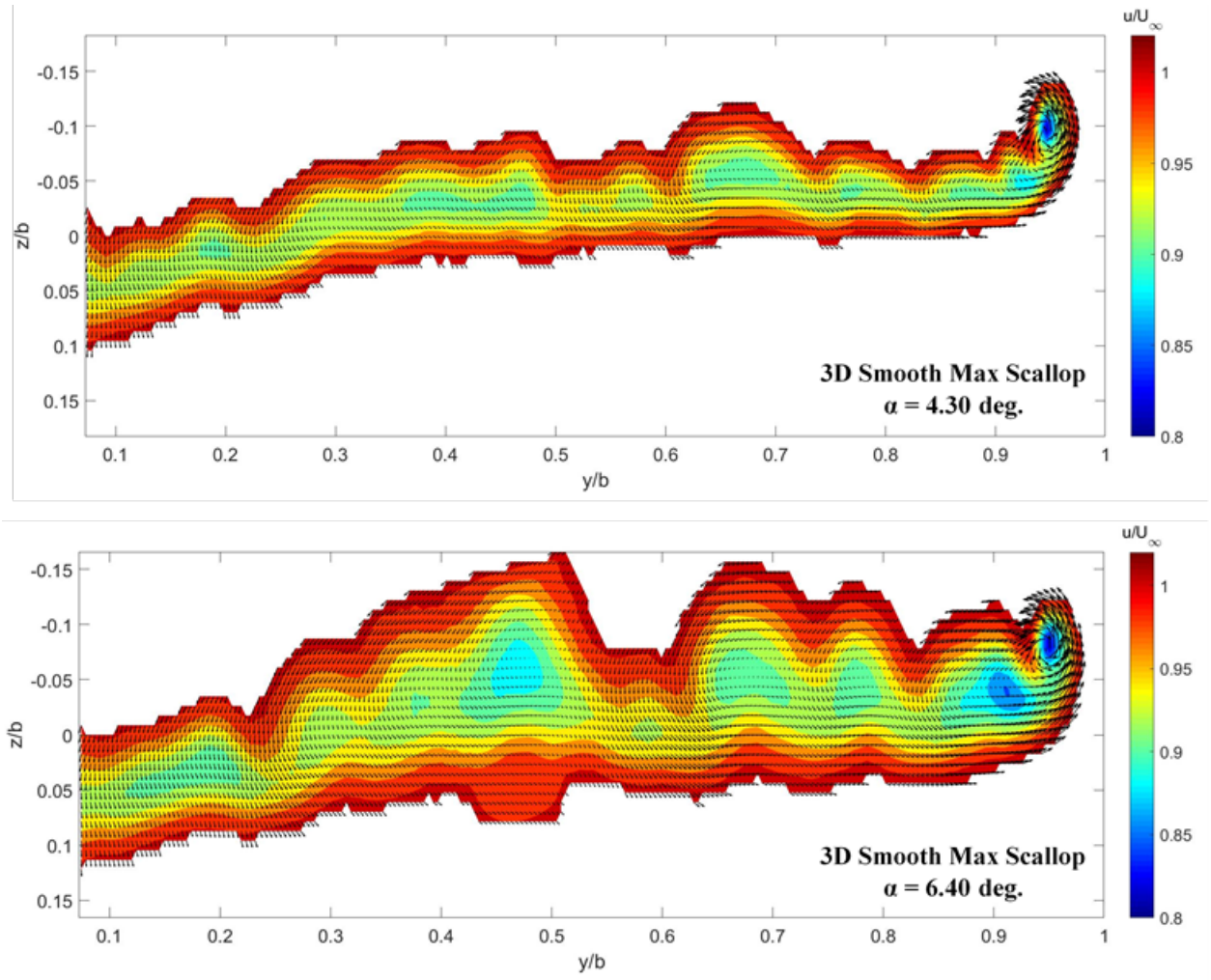

Figure 4.17: Streamwise velocity deficit data for the 3D smooth maximum scallop shape for $\alpha = 4.30°$ and $6.40°$, $Re = 1.6 \times 10^6$, $M = 0.17$.

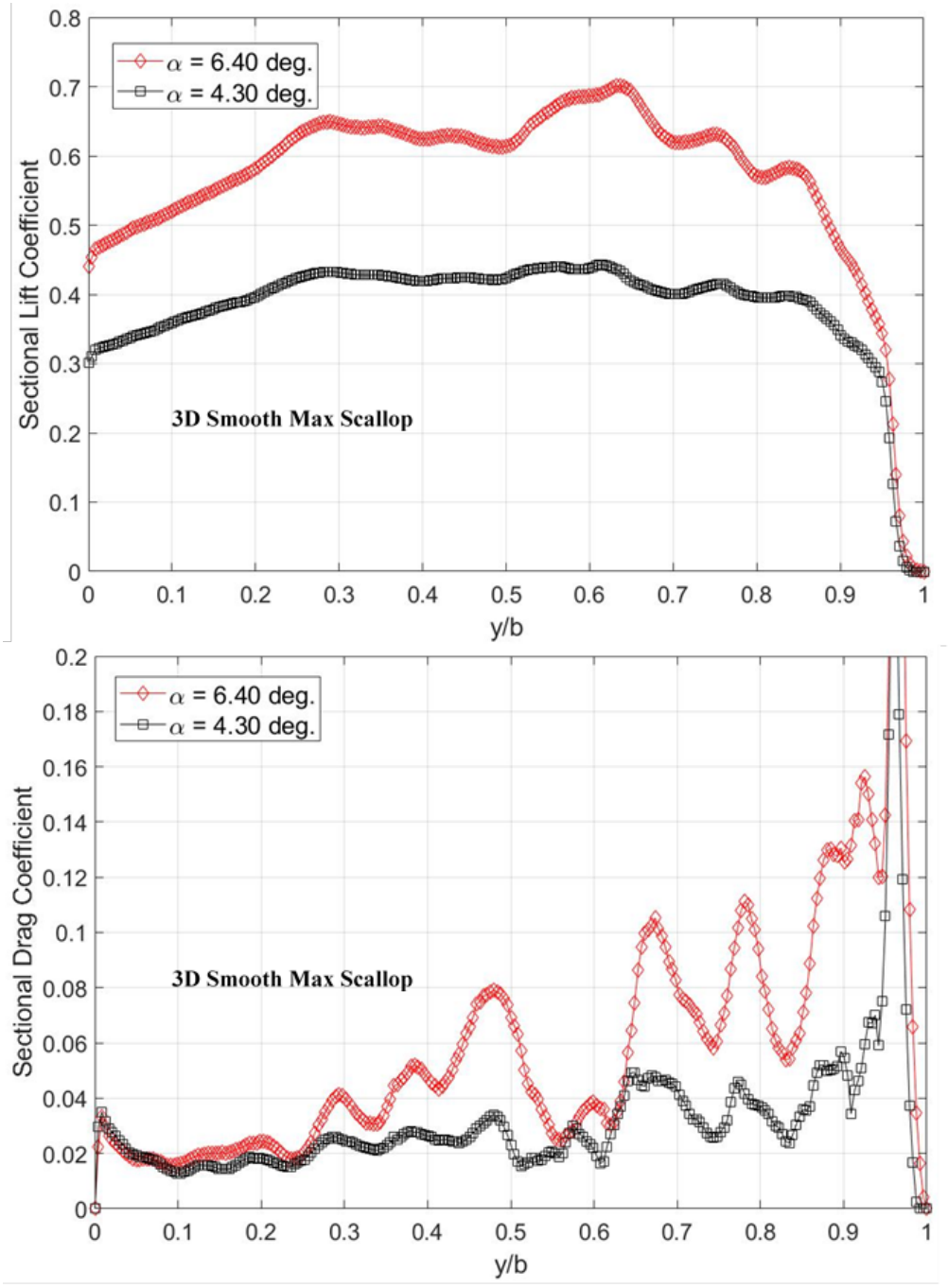

Figure 4.18: Sectional lift coefficient (top) and sectional drag coefficient (bottom) are plotted versus span for the 3D smooth maximum scallop shape for $\alpha = \ 4.30°$ and $6.40°$, $Re = 1.6 \times 10^6$, $M = 0.17$.

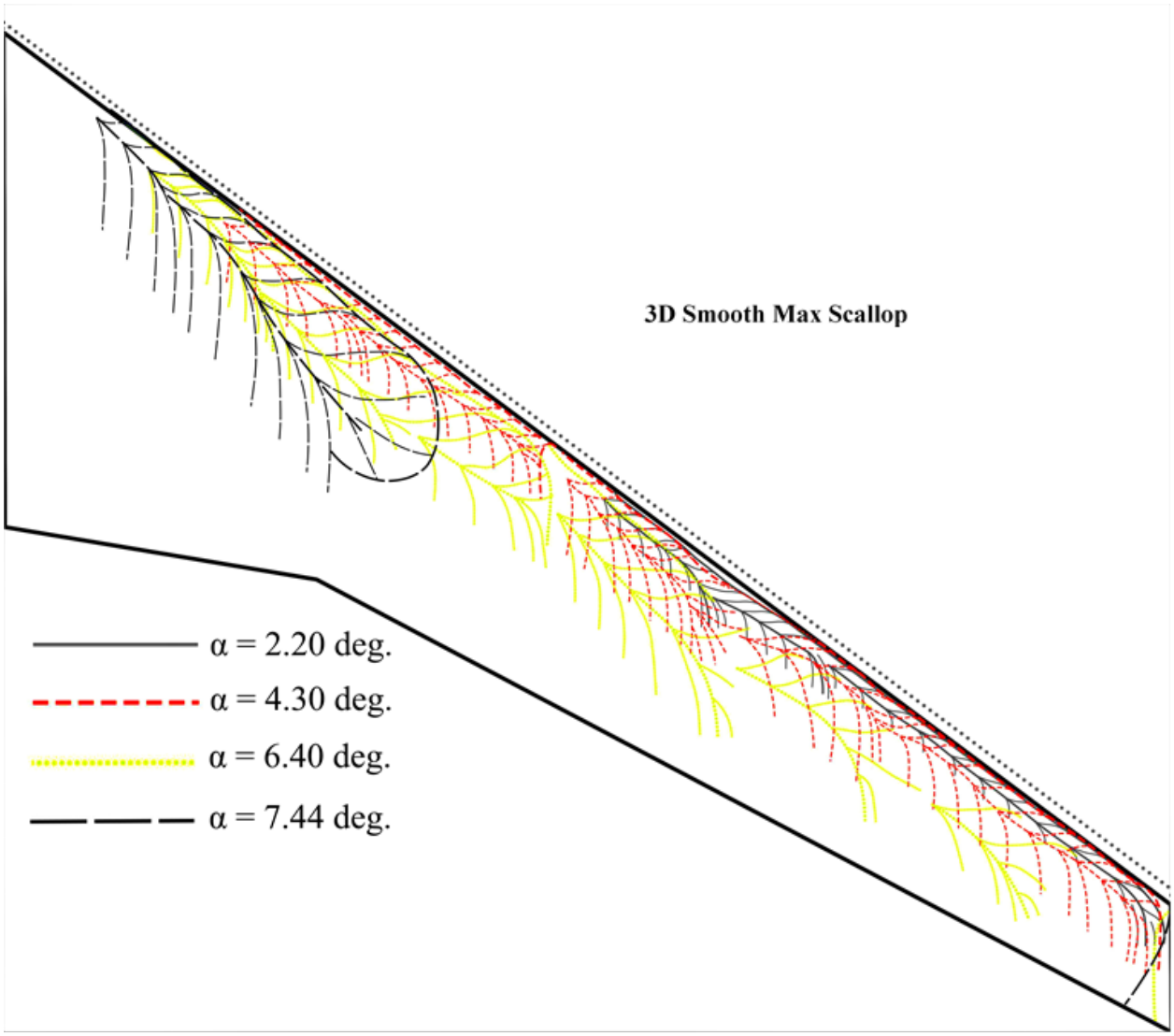

Figure 4.19: A composite image showing the growth of the leading-edge vortices for the 3D smooth maximum scallop shape for $\alpha = \ 2.20°,\ 4.30°,\ 6.40°$, and $7.44°$,$Re = 1.6 \times 10^6$, $M = 0.17$.

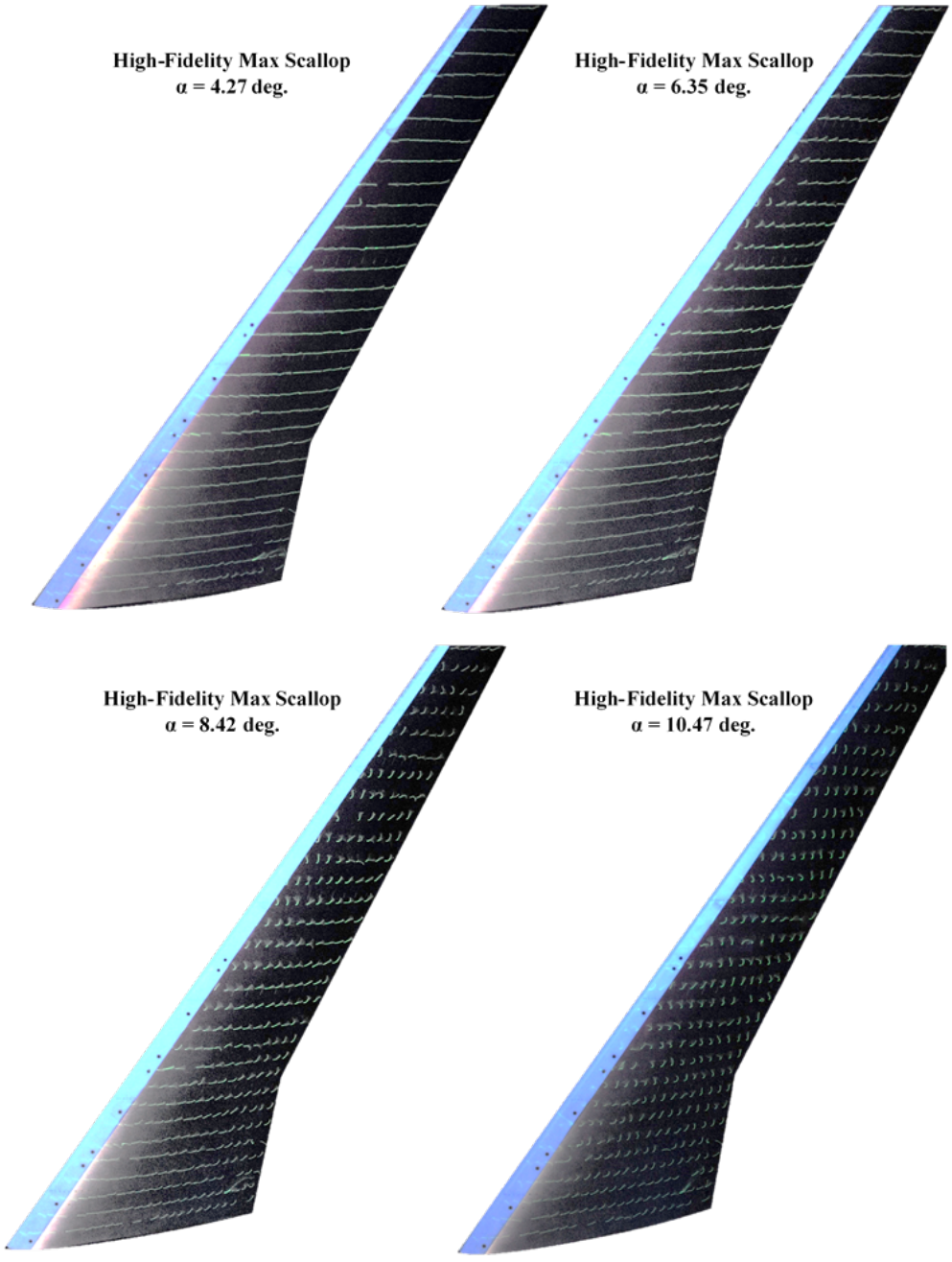

Figure 4.20: Mini-tuft imagery for the high-fidelity maximum scallop shape for $\alpha = 4.27°,\ 6.35°,\ 8.42°$, and $10.47°$, $Re = 1.6 \times 10^6$, $M = 0.17$.

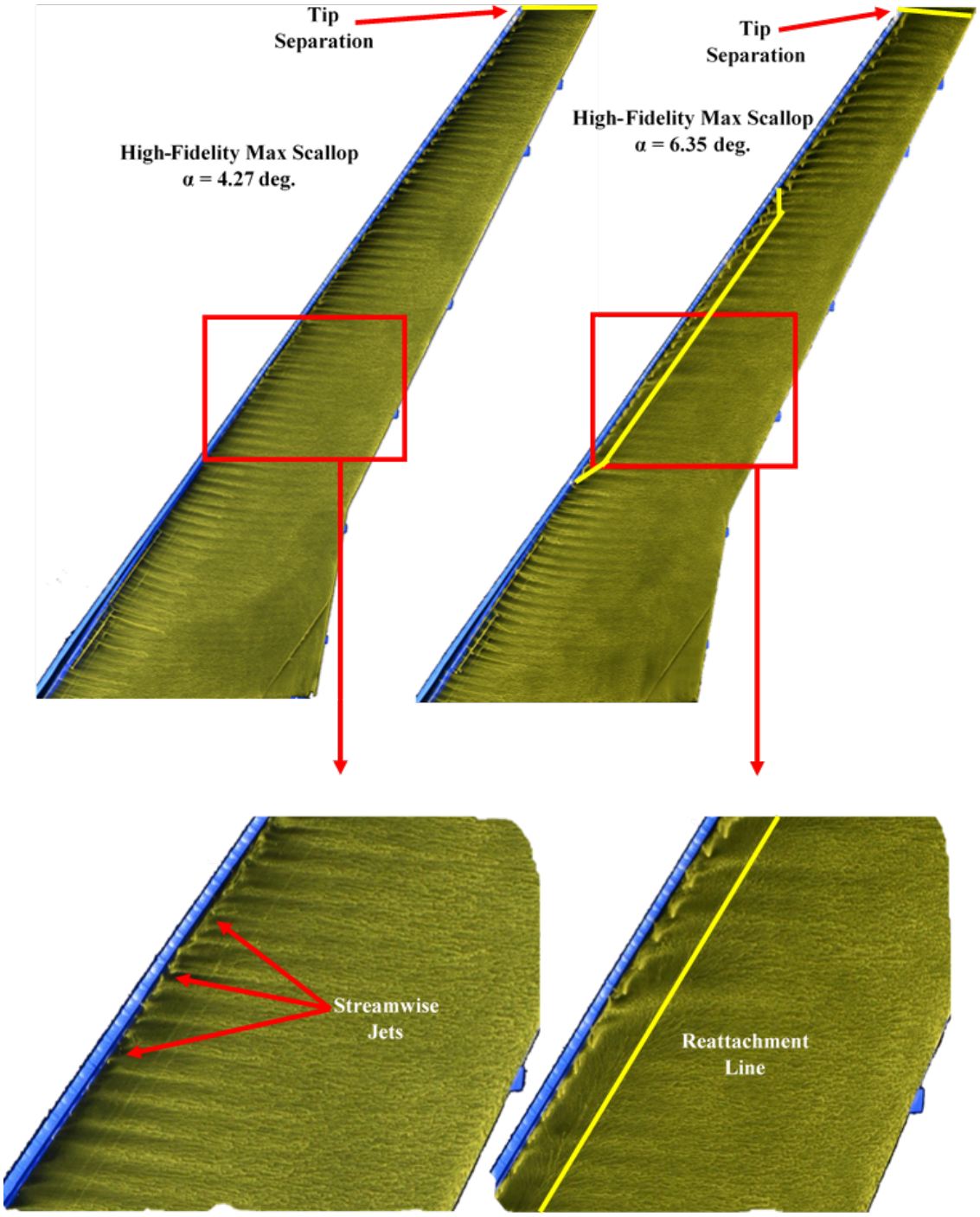

Figure 4.21: Oil flow visualization for the high-fidelity maximum scallop shape for $\alpha =$ 4.27° and 6.35°, $Re = 1.6 \times 10^6$, $M = 0.17$.

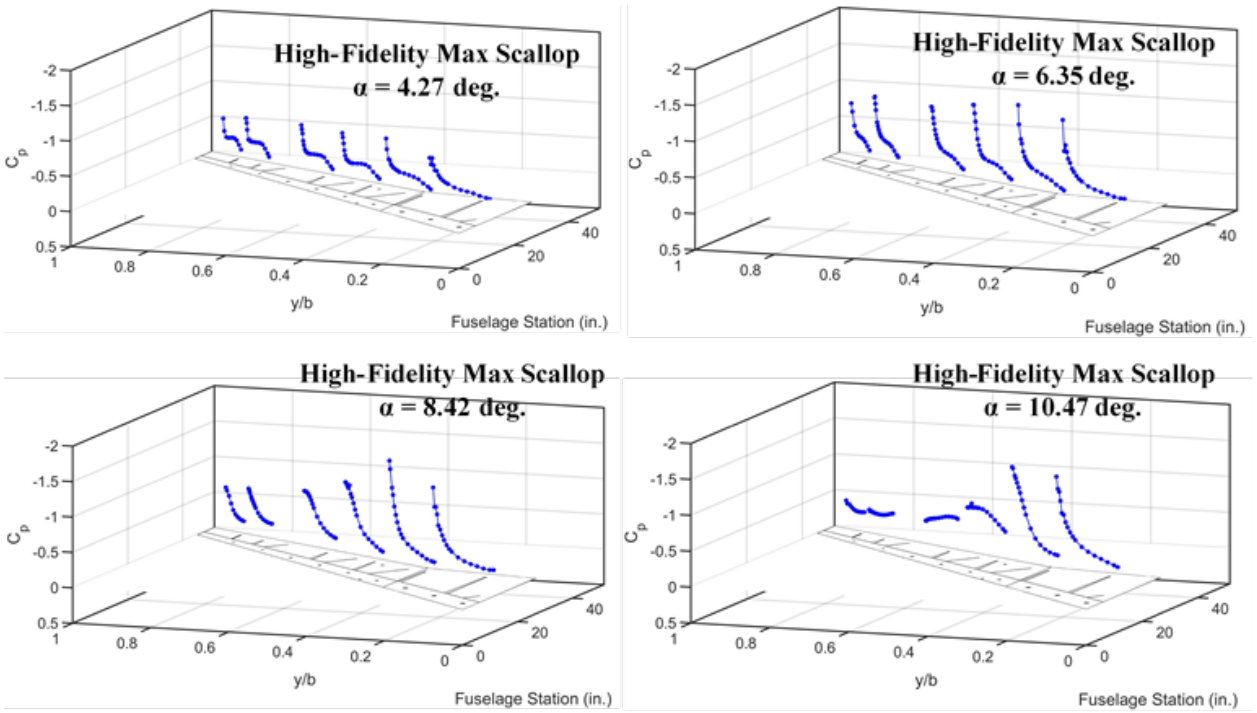

Figure 4.22: Surface pressure data for the upper surface of the wing for the high-fidelity maximum scallop shape for $\alpha = \ 4.27°,\ 6.35°,\ 8.42°$, and $10.47°$, $Re = 1.6 \times 10^6$, $M = 0.17$.

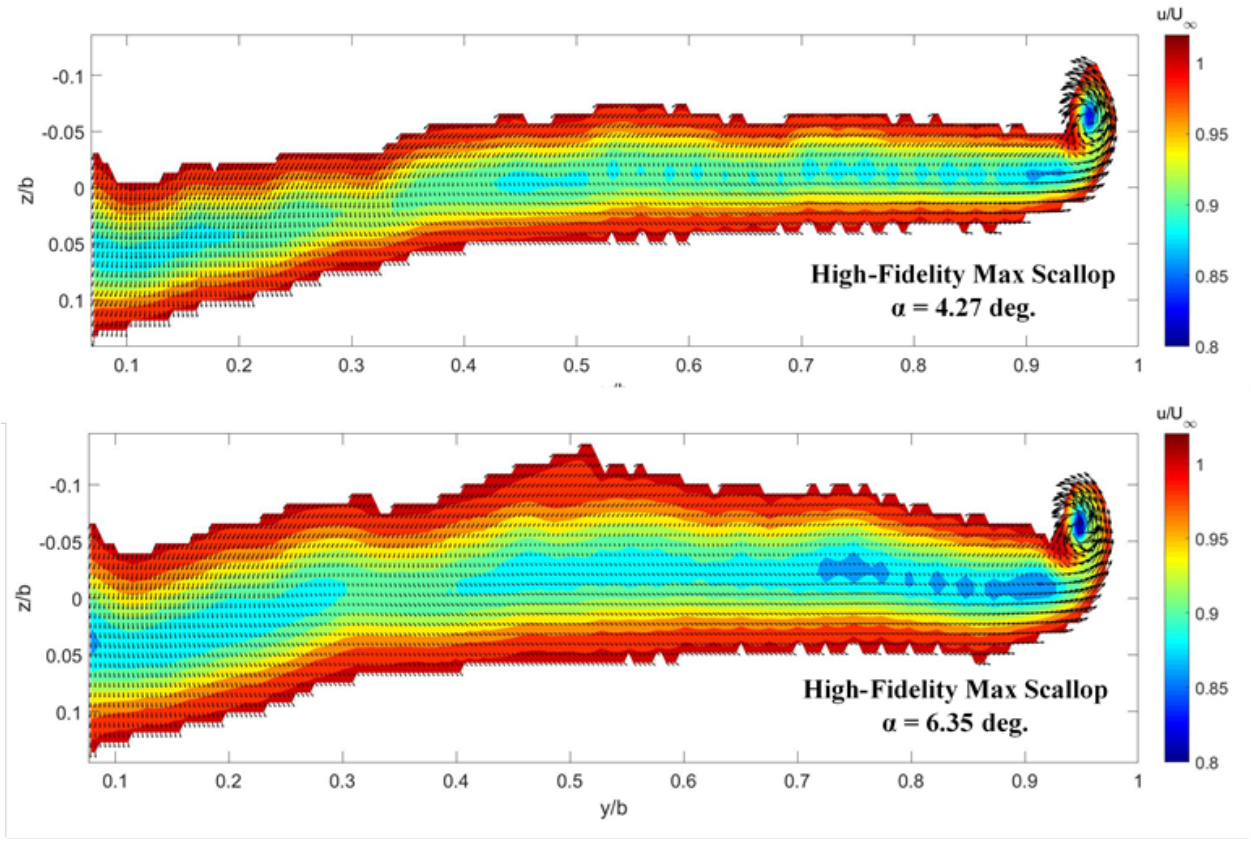

Figure 4.23: Streamwise velocity deficit data for the high-fidelity maximum scallop shape for $\alpha = \ 4.27°$ and $6.35°$, $Re = 1.6 \times 10^6$, $M = 0.17$.

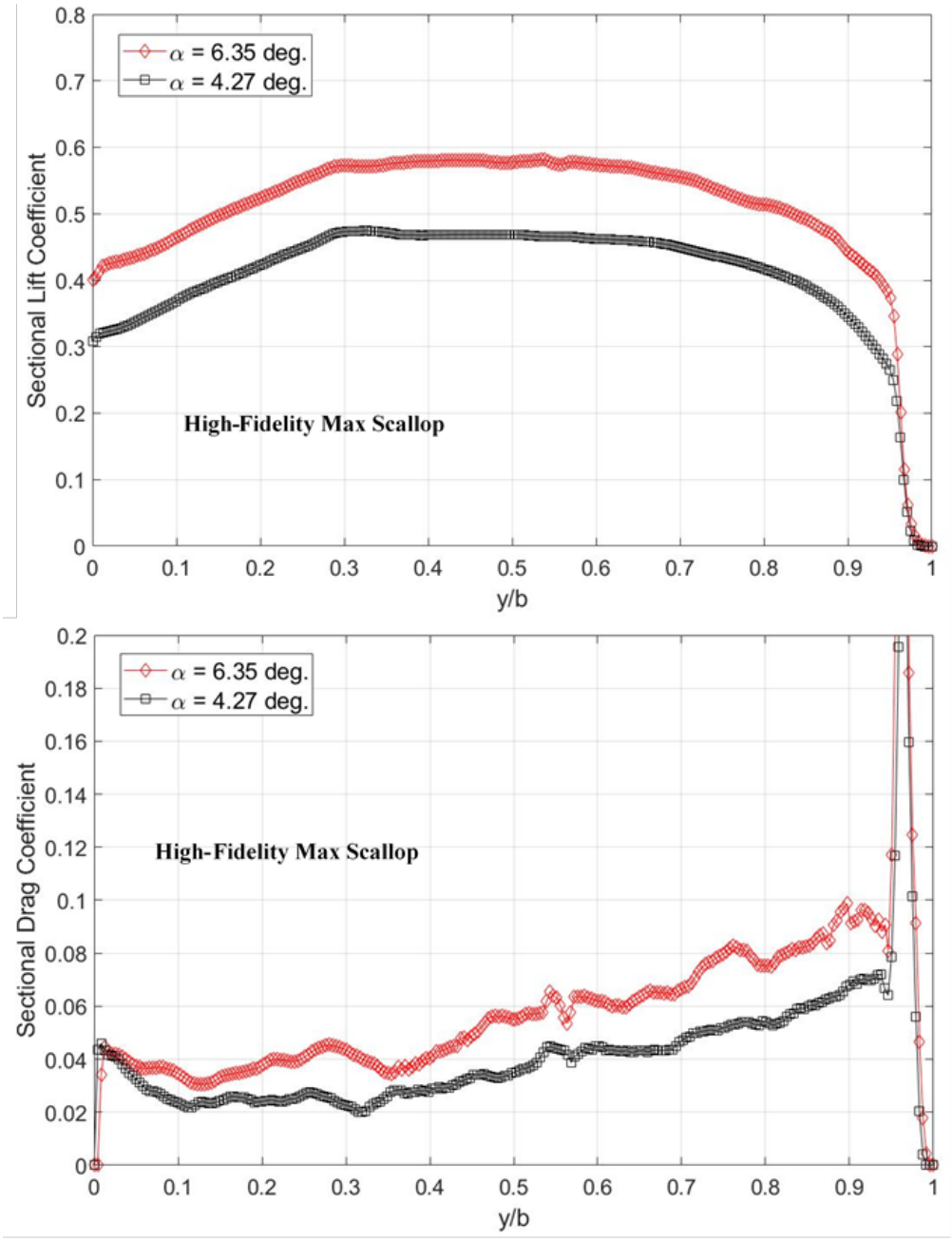

Figure 4.24: Sectional lift coefficient (top) and sectional drag coefficient (bottom) are plotted versus span for the high-fidelity maximum scallop shape for $\alpha = \ 4.27°$ and $6.35°$, $Re = 1.6 \times 10^6$, $M = 0.17$.

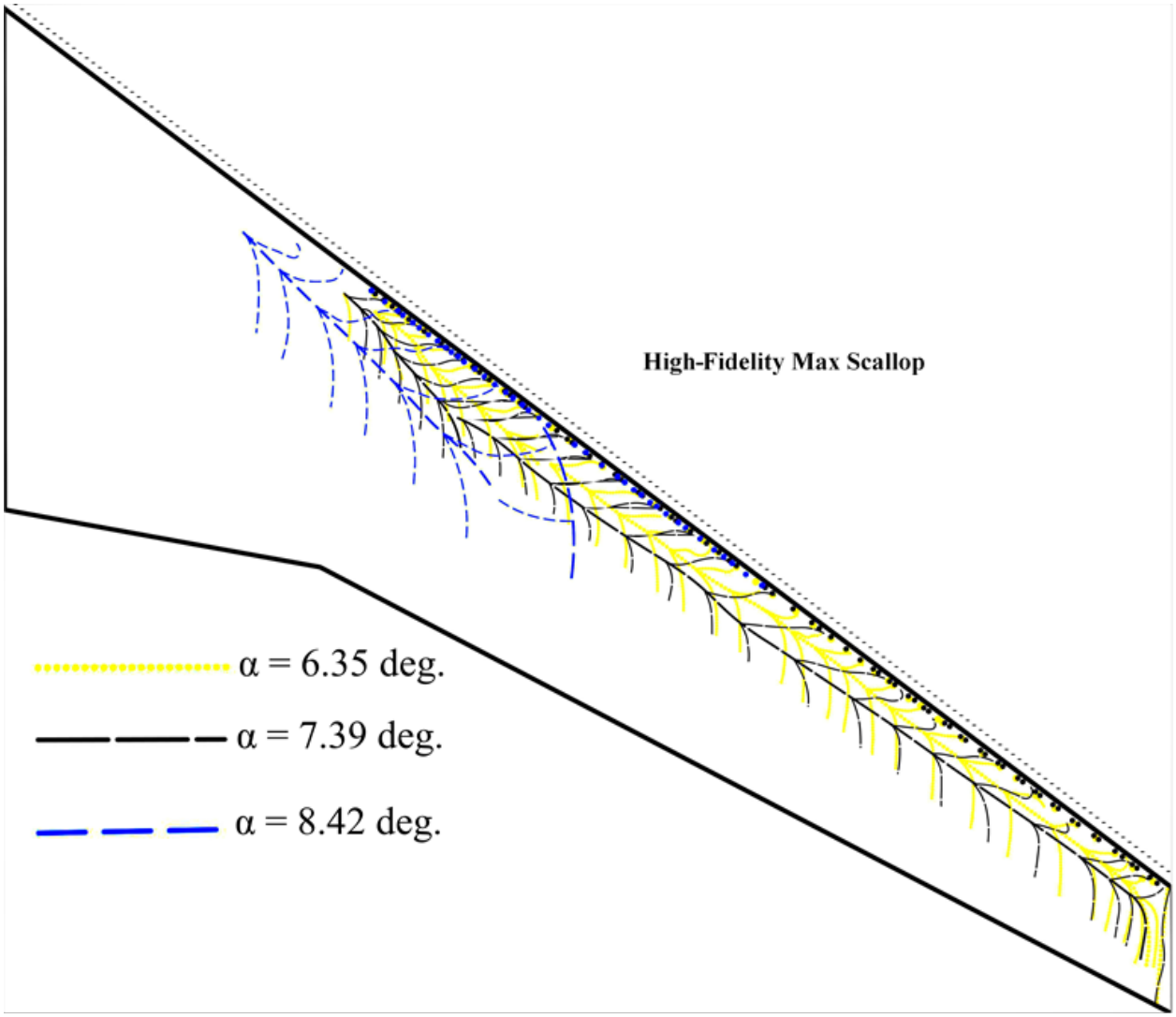

Figure 4.25: A composite image showing the growth of the leading-edge vortices for the high-fidelity maximum scallop shape for $\alpha = 6.35°,\ 7.39°$, and $8.42°$,$Re = 1.6 \times 10^6$, $M = 0.17$.

Chapter 5
SUMMARY, CONCLUSIONS, & RECOMMENDATIONS

5.1 Summary

In this thesis, the aerodynamics of an 8.9% CRM65 swept-wing model with a clean leading edge was studied and used as a baseline to examine the effect of two different fidelities of a scalloped ice shape. The resulting aerodynamics are highly 3D. The mechanisms that govern the aerodynamics of the clean model are the formation of a leading-edge separation bubble and leading-edge vortex and ultimately the leading-edge, tip-first stall. This flowfield is altered significantly by the leading-edge ice simulations. In the case of the 3D smooth maximum scallop ice shape, the leading-edge vortex increases in size markedly compared to the clean wing. It also causes separation to occur at a much lower α and more gradually than the clean wing. This leads to lower C_L, higher C_D, and a more nose-up C_m. The 3D smooth shape causes the wing to stall first on the outboard section, but not on the tip section, of the wing. Using the definition of usable lift of Furlong and Mchugh [11] based on the inflection point of the C_m curve, this decreases the usable lift α by approximatley 4.5° compared to the clean wing.

The high-fidelity maximum scallop shape causes a further reduction in C_L for all α and increase in C_D for α between $-6°$ and 6° than the 3D smooth ice shape. The flow separation pattern for the high-fidelity maximum scallop shape is similar to that of the 3D smooth wing, though it occurs at higher α. The separation region for α less than 8.5° is also smaller than the 3D smooth shape. The geometry of the shape, given the gaps between highly-3D scallop protuberances from the leading-edge, is thought to cause streamwise flow features to develop. These features are proposed as streamwise jets in this thesis. These jets are proposed as being responsible for the delay in leading-edge separation by re-energizing the flow over the upper

surface of the wing and by delaying leading-edge vortex formation. However, examining the spanwise geometry changes of the high-fidelity shape reveals that the gaps decrease in size relative to the size of scallops themselves near the midspan. In this region, the jets disappear at moderate α and allow a small leading-edge separation region to form. Streamwise features are seen in the wake survey suggesting that the streamwise jet features are influencing the flowfield downstream of the wing.

5.2 Conclusions

The observations summarized above lead to several conclusions:

1. The clean wing experienced an aggressive, tip-first stall, which was not seen for the wing with the different fidelities of the maximum scallop ice shape.

2. Leading-edge vortex diffusion near the tip and spanwise flow over the upper surface of the wing causes the tip to stall prior to the rest of the wing. Due to a boundary-layer suction effect created by the spanwise flow on the upper surface of the wing, there is little-to-no separation at the root of the wing. This remains true for the iced leading-edge cases.

3. The clean wing had a small, relatively strong leading-edge vortex at lower α, while the iced cases tend to have much larger, seemingly weaker leading-edge vortices. The size of the leading-edge vortex varies greatly between the two fidelities of the maximum scallop ice shape.

4. The 3D smooth ice shape caused nonlinear variations in C_L, increased C_D, and created a nose-up C_m compared to the clean wing. This is due to the large amounts of separation that occured over the wing at moderate α though the onset of this separation was much more gradual than for the clean wing. This also led to a decrease in maximum usable lift α of approximately 4.5° compared to the clean wing.

5. The high-fidelity shape generated streamwise flow features that repeat spanwise downstream of the ice simulation due to flow through the gaps in the shape. These jets are proposed to alter the aerodynamics compared to the 3D smooth shape by re-energizing the flow and delaying flow separation near the leading-edge.

6. The variation in the scallop shape resulting from the interpolation process used to generate it is possibly seen in the aerodynamics near the midspan of the wing, where the ratio of scallop width to gap width in the shape is increased. This variation, which is more extreme than the variation in the 3D smooth shape, could affect the formation of the leading-edge vortex by preventing the streamwise flow features from forming over the high-fidelity shape.

7. The high-fidelity shape experienced large amounts of separated flow at similar α to that of the 3D smooth shape, and thus much sooner than the clean wing. The changes in aerodynamic performance caused by the high-fidelity shape are more nonlinear in C_L than the 3D smooth shape, evidenced by a more nonlinear $\frac{\delta C_L}{\delta \alpha}$ for the high-fidelity shape. Changes in the aerodynamics of the high-fidelity shape are still gradual compared to the clean wing.

8. Both of the scalloped ice shapes showed some sign of trailing-edge separation, which is likely why they experience an earlier but more gradual degradation in aerodynamic performance compared to the clean wing.

9. The 3D smooth ice shape tested was non-conservative in its aerodynamic penalties as compared to the high-fidelity shape.

5.3 Recommendations

These results and conclusions lead to recommendations for extending this research:

1. More information is needed to fully understand the effect of scallop ice shape gaps on aerodynamics and before these data can be extrapolated to a more general result. Artificial ice geometry wind tunnel tests that varies the gap size and spacing are planned over a range of Re and M combinations to improve our understanding of the phenomena observed in these tests. This analysis should be revisited after that data is collected.

2. Improved measurements and visualization could improve our understanding of the streamwise features seen in the high-fidelity case and how it impacts the flowfield and resulting iced swept-wing aerodynamics.

   (a) Off-body flow visualization could be utilized to observe more closely the jet features and their interaction with and effect on the overall flow.

   (b) Pressure taps on the ice shape itself such that the pressure coefficient on the leading edge of the wing can be measured with an ice shape attached would be very useful. Increasing the resolution of pressure taps over the upper surface of the wing may also help quantify the nature of the observed flow features, such as the leading-edge vortices and streamwise jets.

   (c) More spatial fidelity in the wake survey technique would aid in understanding the smaller features in the flow, such as the potential vortices that manifest at the wake plane. This would yield a better understanding of the flowfield over the wing itself. This could be coupled with performing wake survey measurements at multiple streamwise planes, allowing for a study of the evolution of the wake and flowfield.

   (d) There are unsteady effects in the wake of the wing that are unaccounted for with the use of a standard five-hole probe. Data collection with a fast-response five-hole probe is planned and should be used to quantify and visualize as best as possible unsteadiness in the wake of the wing, as this would aid in the understanding of the unsteadiness over the surface of the wing.

Appendix A
WAKE SURVEY BACKGROUND

This appendix will briefly cover the background of the wake survey system, including equation derivation, data collection, and data reduction. The wake survey system can provide a quantitative visualization of the wake of an object. Studying these wakes in detail can provide meaningful insight into the aerodynamics occurring over a body. Note that while this overview is brief, more detailed derviations and information can be found in Betz [35], Maskell [36], Diebold [37, 45], and Lum [41].

A.1 Derivation of Wake Survey Equations

The wake survey equations that express the aerodynamic forces over a body based on the pressure and velocity measurements in its wake are derived via a control volume analysis made with several assumptions in mind. This analysis was developed by Betz [35] and Maskell [36], and was summarized by Diebold [37]. This analysis is briefly reviewed here for convenience. The control volume considered is shown in Fig. A.1. The assumptions used are as follows:

1. The upstream plane (S_1) is located far enough upstream so as not to be influenced by the model.

2. Wake survey data are measured at a single transverse plane (S_2).

3. The flow at the wake survey is steady and incompressible.

4. No suction or blowing through the walls.

5. The tunnel has a uniform effective cross section.

6. Turbulent stresses are negligible.

This control volume analysis yields the following results for drag and lift:

$$D = \iint_{S_1} (P + \rho U_\infty^2 \, dy \, dz - \iint_{S_2} (P + \rho u^2) \, dy \, dz \tag{A.1}$$

$$L = - \iint_{S_2} (P - P_\infty) n_z + \rho (w(U_\infty + u) n_x + wv n_y + w^2 n_z) \, dy \, dz \tag{A.2}$$

where u, v, and w are the flow velocities in the x, y, and z directions and n_x, n_y, and n_z represent the unit vectors for the coordinate system. Note that lift is the force taken in the z-direction defined in Fig. A.1.

These equations can be reduced to integrals that are only taken over the wake region. This is beneficial as it reduces the amount of data that needs to be taken to derive the forces. For the drag equation, the reductions involve the use of a perturbation velocity, u', an artificial velocity, u^*, and the wake blockage velocity, u_b. They are defined as

$$u' = u^* - U_\infty \tag{A.3}$$

$$u^{*2} = u^2 + \frac{2}{\rho}(P_{t,\infty} - P_t) \tag{A.4}$$

$$u_b = \frac{1}{S_2} \iint_W (u^* - u) \, dy \, dz \tag{A.5}$$

where the region W now refers to only the wake region in the S_2 plane. The final piece necessary to reduce the drag equation involves the use of the streamwise vorticity, ξ, and the transverse stream function, ψ. These are defined as

$$\xi = \frac{\delta w}{\delta y} - \frac{\delta v}{\delta z} \tag{A.6}$$

$$-\xi = \frac{\delta^2 \psi}{\delta y^2} + \frac{\delta^2 \psi}{\delta z^2} \tag{A.7}$$

with the stream function being subject to the boundary condition at the tunnel walls of

$$\psi = 0 \tag{A.8}$$

Equations A.3 to A.8 are used to reduce Eq. A.1 to a wake integral. In this process, given in more detail by Diebold [37], *u'* disappears and the final drag result is given as

$$D = \iint_W ((P_{t\infty} - P_t) + \frac{\rho}{2}(u - u^*)(u + u^* - 2(U_\infty + u_b)))\, dy\, dz + \frac{\rho}{2} \iint_W \psi\xi\, dy\, dz \tag{A.9}$$

The first integral in Eq. A.9 is considered the profile drag while the second integral is the induced drag.

The lift integral can be similarly reduced to an area of just the wake region behind the model. Two more definitions are rquired to reduce the lift integral. They are the perturbation pressure, Δp, and the pressure defined in terms of this perturbation pressure.

$$\Delta p = -\rho u U_\infty \tag{A.10}$$

$$P = P_\infty + \Delta p \tag{A.11}$$

The terms in Eq. A.2 that are a product of the perturbations u, v, and w are dropped, as these are negligible compared to others. Using the definitions given in Eq. A.10 and Eq. A.11, the resulting equation is written as

$$L = \rho U_\infty \iint_{S_2} u n_z - w n_x\, dy\, dz \tag{A.12}$$

Using a series of vector identities, this integral can be rewritten as

$$L = \rho U_\infty \iint_{S_2} y\xi\, dy\, dz \tag{A.13}$$

Note that because the vorticity is ideally zero outside of the wake, this integral can be taken over the wake region W

$$L = \rho U_\infty \iint_W y\xi \, dy \, dz \tag{A.14}$$

Equation A.14 represents the lift generated by a 3D body as calculated using wake measurements. Thus, both Eq. A.9 and Eq. A.14 represent the necessary measurements to do a steady-state wake survey analysis.

A.2 Wake Survey System Methodology

This section will describe the background methodology of collecting data using the wake survey system.

A.2.1 Coordinate Frames

The coordinate system and dimensions associated with the traverse arm is shown in Fig. A.2. Coordinate frames that are associated with the probe are shown in Fig. A.3. These various coordinate frames are defined and summarized in Table A.1. Note that F_p is defined by the probe manufacturer and is somewhat unconventional. To combat this, one can define a coordinate system, F_b, that is consistent with standard flight dynamics conventions [46].

A.2.2 Probe Mount and Design

The probe mount and associated fairing was designed to minimize aerodynamic load on the traverse system. The fairing was designed to minimize the upstream aerodynamic effect of the probe holder body on the measurements taken at the tip of the probes.

The probe holder has a laser locator embedded near the top of the mount. The laser locator was used to more accurately obtain the position of the probe tips in the test section. This system is described in more detail in Appendix Once the probes and fairing are installed, the geometry of the probe is scanned using a Leica T-Scan 5 [47] handheld scanner. This yields precise measurements of the relative location of the probe tips with respect to the laser locator, $\overline{r}_{i/T}$.

The probe pose is completely characterized by 4 parameters.

1. $\overline{r}^{TS}_{L/TS}$ = position of the laser locator w.r.t. the test section origin

2. $\phi_{T/L} = \theta_{SA}$ = the angle of the strut

3. $\overline{r}^{T}_{i/T}$ = the location of the 3 probe tips with respect to the laser locator ($i = 1, 2, 3$)

4. $\overline{r}^{TS}_{SA/TS}$ = location of the swing arm origin w.r.t. the origin of the test section (fixed and constant)

$\overline{r}^{TS}_{SA/TS}$ is constant and known to be $(-127.8120 \;\; 0 \;\; -43.078)^T$ inches. Furthermore, the probe locations are also constant and measured at the start of the test as show in Fig. A.4. Precise values for these measurements are summarized in Table A.2.

Thus, there are practically only two unknowns, $\overline{r}^{TS}_{L/TS}$ and $\phi_{T/L} = \theta_{SA}$ that must be measured or computed for subsequent calculations. When storing information about the orientation of the wake survey system, it is sufficient to obtain these four parameters and then derive other desired quantities. For example, if one thinks of the F_T as the "body frame" and F_L to be the "NED frame" [46] , the rotation matrix to go from F_L to F_T is given by

$$C_{T/L}(\phi_{T/L}) = \begin{pmatrix} 1 & 0 & 0 \\ 0 & \cos(\phi_{T/L}) & \sin(\phi_{T/L}) \\ 0 & -\sin(\phi_{T/L}) & \cos(\phi_{T/L}) \end{pmatrix} \tag{A.15}$$

The probe will measure velocities in the F_T coordinate frame. We can then rotate these to the laser frame

$$\overline{V}^{L} = C_{T/L}(\phi_{T/L})^T \overline{V}^{T} \tag{A.16}$$

Probe Position Expressed in Test Section Frame

For the positions of the probes, we would like to express vectors in F_{TS}. We note that since F_L and F_{TS} are oriented the same and only are different by a translation, we can write

$$\overline{r}^{TS}_{i/TS} = \overline{r}^{TS}_{L/TS} + C_{L/T}(\phi_{T/L})\overline{r}^{T}_{i/T} \tag{A.17}$$

Note that $\overline{r}^{TS}_{L/TS} = \overline{r}^{TS}_{T/TS}$ since F_L and F_T have the same origin so we can use whichever is more convenient in the formulation of Eq. A.17.

Set Probe Pose Using Single Measurement

Eq. A.17 allows one to compute $\overline{r}^{TS}_{i/TS}$ if given the pose of the probe ($\phi_{T/L}$ and $\overline{r}^{TS}_{L/TS} = \overline{r}^{TS}_{T/TS}$). The reverse problem can also be solved. In other words, if we are given $\overline{r}^{TS}_{i,TS}$ for one of the probes, we can determine the probe pose of $\phi_{T/L}$ and $\overline{r}^{TS}_{L/TS}$. Note that we do not need to solve for $\overline{r}^{T}_{i/T}$ because we assume this is constant (the probes are fixed in the traverse frame and do not change). From Fig. A.2 we can write $\overline{r}^{TS}_{i/SA} = \overline{r}^{TS}_{i/TS} - \overline{r}^{TS}_{SA/TS}$. The swing arm angle can now be computed using the 2^{nd} and 3^{rd} components of the $\overline{r}^{TS}_{i/SA}$ vector.

$$\phi_{T/L} = \text{atan2}(-\overline{r}^{TS}_{i/SA}(2), \overline{r}^{TS}_{i/SA}(3)) \tag{A.18}$$

In Eq. A.18, atan2 is assumed to accept the opposite side as the first argument and the adjacent side as the second argument.

Once $\phi_{T/L}$ is know, the last parameter characterizing the wake survey system is computed as

$$\overline{r}^{TS}_{L/TS} = \overline{r}^{TS}_{i/TS} - C_{L/T}(\phi_{T/L})\overline{r}^{T}_{i/T} \tag{A.19}$$

A.2.3 Probe Calibration

Each probe is a straight, 5-hole probe manufactured and calibrated by Aeroprobe[48]. Probe 1, 2, and 3 have serial numbers of 11062C, 15207-1, and 15207-2, respectively.

The probes are calibrated by the manufacturer for Mach 0.18. Results of the calibration are used to generate calibration lookup tables for α, β, C_{pt}, and C_{ps} based on a sector interpolant method. Specifics of this sector interpolant method were developed and documented by Diebold et. al. [37].

A representative result of this calibration for a single probe is shown in Fig. A.5. As can be seen, this method produces results that are accurate to within $\pm 2°$ in angularity for the range of angles. For lower angles of incidence (less than approximately 43°), the method has less than 0.5° of error in flow angularity.

A.2.4 Leica Position System

Both R_{SA} and θ_{SA} are measured by a motor encoder on the traverse system. A first-order-accurate position of the probes can be obtained using a simple polar coordinate system model of the traverse system. However, once the strut is subjected to aerodynamic loads, it will deform and deflect, thereby moving the location of the probes to an unknown position. To combat this problem, a Leica Absolute Tracker AT901 [49] laser tracking system was used to measure the absolute position of the laser locator in the test section. Before the test, this system was Aligned and calibrated with respect to landmark locations in the tunnel.

Once the desired locations of the 3 probes are computed for the entire trajectory, the point L_S that corresponds to these positions can be computed. L_S is the point of reference for the WSU traverse control system and is obtained by projecting the origin of the laser locator onto the strut by moving in the direction of y_{SA} as shown in Fig. A.6.

Note that is is not necessary to compute the point $\overline{r}^{TS}_{LS/TS}$ as only the radial extension and angle of the arm, R_SA and θ_{SA} are needed to control the position of the arm. From vector geometry, we can first obtain the location of the laser tracker with respect to F_{SA} origin and expressed in F_{SA}

$$\overline{r}^{SA}_{L/SA} = C_{T/L}(\phi_{T/L})\overline{r}^{TS}_{L/TS} - C_{T/L}(\phi_{T/L}(\phi_{T/L})\overline{r}^{TS}_{SA/TS} \tag{A.20}$$

From Fig. A.6, we see that the traverse arm radial extension is simply the z component of $\overline{r}_{L/SA}$ when expressed in F_{SA}.

$$R_{SA} = |\overline{r}^{SA}_{L/SA}(3)| \tag{A.21}$$

The algorithm is shown below

1. Determine desired position of one of the probes, $\overline{r}^{TS}_{i/TS}$
2. Set the pose of the probe to be consistent with this position
   (a) Compute $\phi_{T/L}$ via Eq. A.18
   (b) Compute $\overline{r}^{TS}_{L/TS}$ via Eq. A.19
3. Obtain equivalent traverse swing arm angle as $\theta_{SA} = \phi_{T/L}$
4. Obtain equivalent traverse swing arm radius via Eq. A.21

This value of R_{SA} and θ_{SA} can then be used by the WSU traverse positioning system to move the probe to the desired location.

A.3 Data Reduction

This section describes the collection and reduction of the data acquired by the wake survey system.

Data collected by the wake survey system were not acquired on a rectangular grid. An example of a data collection path is shown in Fig. A.8. However, the wake integrals in Eq. A.9 and Eq. A.14 are most easily performed using numerical integration on a rectangular grid. Therefore, the data were interpolated onto a rectangular grid using the scatteredInterpolant function in MATLAB.

Due to the large spanwise length of the wake, the wake survey physically took place as two individual runs. As shown in Fig. A.9, the wake survey rake had an upper and lower

position for data collection. Thus, both sets of data (the inboard and outboard run) had to be combined to form the full wake data set. Some data overlapped between the two individual runs, but as one set of data was configured to have a finer spatial resolution in the overlap region. Thus, the coarser data was removed prior to data reduction.

Before data could be integrated, the boundary of the wake was identified. In theory, the integrands of the wake integrals should be zero outside of the wake itself. This occurs mathematically as $P_{t\infty} - P_t$ and ξ are ideally zero outside of the wake. Therefore, integrating over the entire measurement plane should yield the same result as integrating over just the wake region. However, due to experimental error, this is not true. Thus, the edge of the wake had to be found so the numerical integration can be performed over just the area of the wake to avoid introducing erroneous forces due to the measurement error outside the wake. Identification of the wake was done by looking at the total pressure coefficient, C_{pt}, defined as $\frac{P_t}{q_\infty}$, at each point in the flow. In the wake, there is a pressure loss associated with drag; in the freestream, there is no pressure loss. Any point in the flow with a total pressure coefficient equal to or greater than one (possible due to slight measurement inaccuracies) are considered the freestream. The wake integrands in these regions were set to zero, ensuring the only components contributing to integration were in the wake of the model. An example of the data before and after this process is shown in Fig. A.10 and Fig. A.11. A small region near y/b = 0.08 and z/b = -0.05 shows a total pressure coefficient slightly lower than one. This data was assumed to be experimental error and was removed heuristically prior to executing the previously described wake finding algorithm.

Both ξ and the ψ had to be calculated before integration could occur. To calculate vorticity, the numerical derivatives of the v and w components of velocity were found using a second-order central differencing method. Then, vorticity was found directly from Eq. A.6.

Calculating stream function was more complex. The computational domain had to be extended from the rectangular data region to the tunnel walls to ensure that the boundary condition given by Eq. A.8 was met. This is possible because ξ is zero outside of the wake, and from Eq. A.7, this sets the forcing function to zero as well. From here, the successive

over-relaxation method was used to calculate the stream function iteratively. The successive over-relaxation method is an offshoot of the Gauss-Seidel iterative method that leads to faster convergence of a numerical solution. The successive over-relaxation parameter was chosen by trial.

Integration was performed using the numerical trapezoidal method in both dimensions of the wake. This resulted in a single value for lift, induced drag, and profile drag. To find sectional induced drag coefficients and sectional profile drag coefficients, Eq. A.9 was used, but only a single integration was performed in the direction normal to the wing at each given spanwise location, resulting in a spanwise distribution. Sectional lift coefficient was found via classical wing theory and involved finding the spanwise circulation distribution from the spanwise vortex strength distribution. The local vorticity strength, γ, was calculated by taking the integral of the vorticity perpendicular to the surface of the wing at a given spanwise location. The circulation distribution was then found as

$$\Gamma = \int_0^{y_{ws}} \gamma dy_{ws} \tag{A.22}$$

Using spanwise circulation and chord distribution, the sectional lift coefficient is found

$$c_l = \frac{2\Gamma}{cU_\infty} \tag{A.23}$$

where c represents the chord at a given spanwise location.

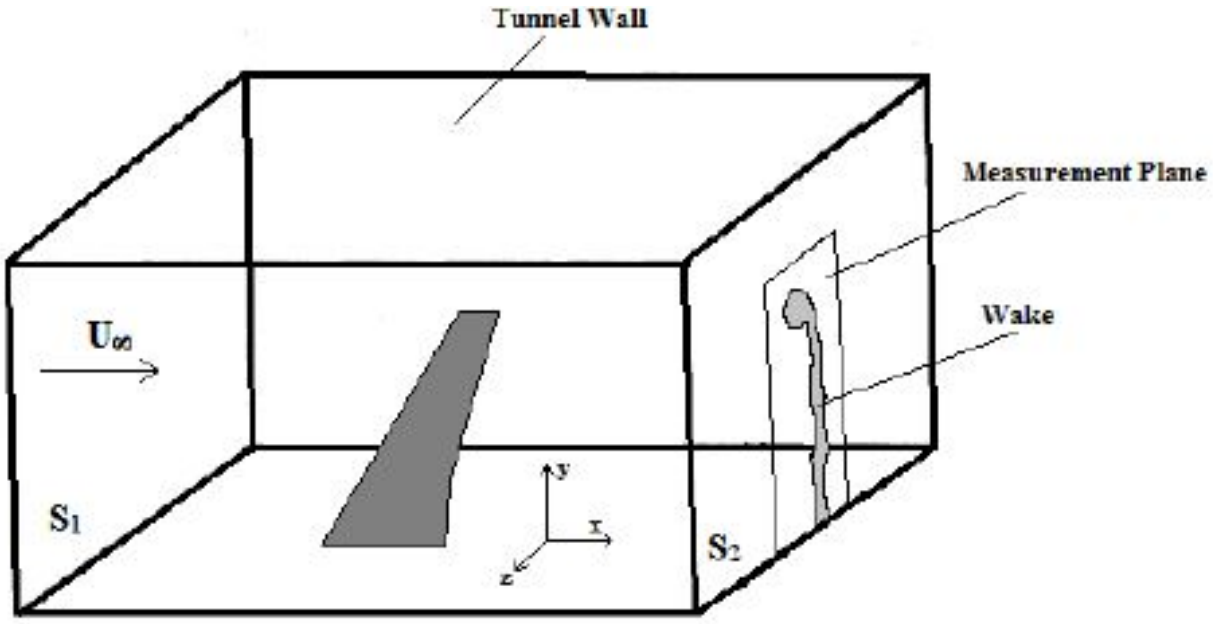

Figure A.1: The control volume used to derive the wake survey equations. Adapted from Diebold [37].

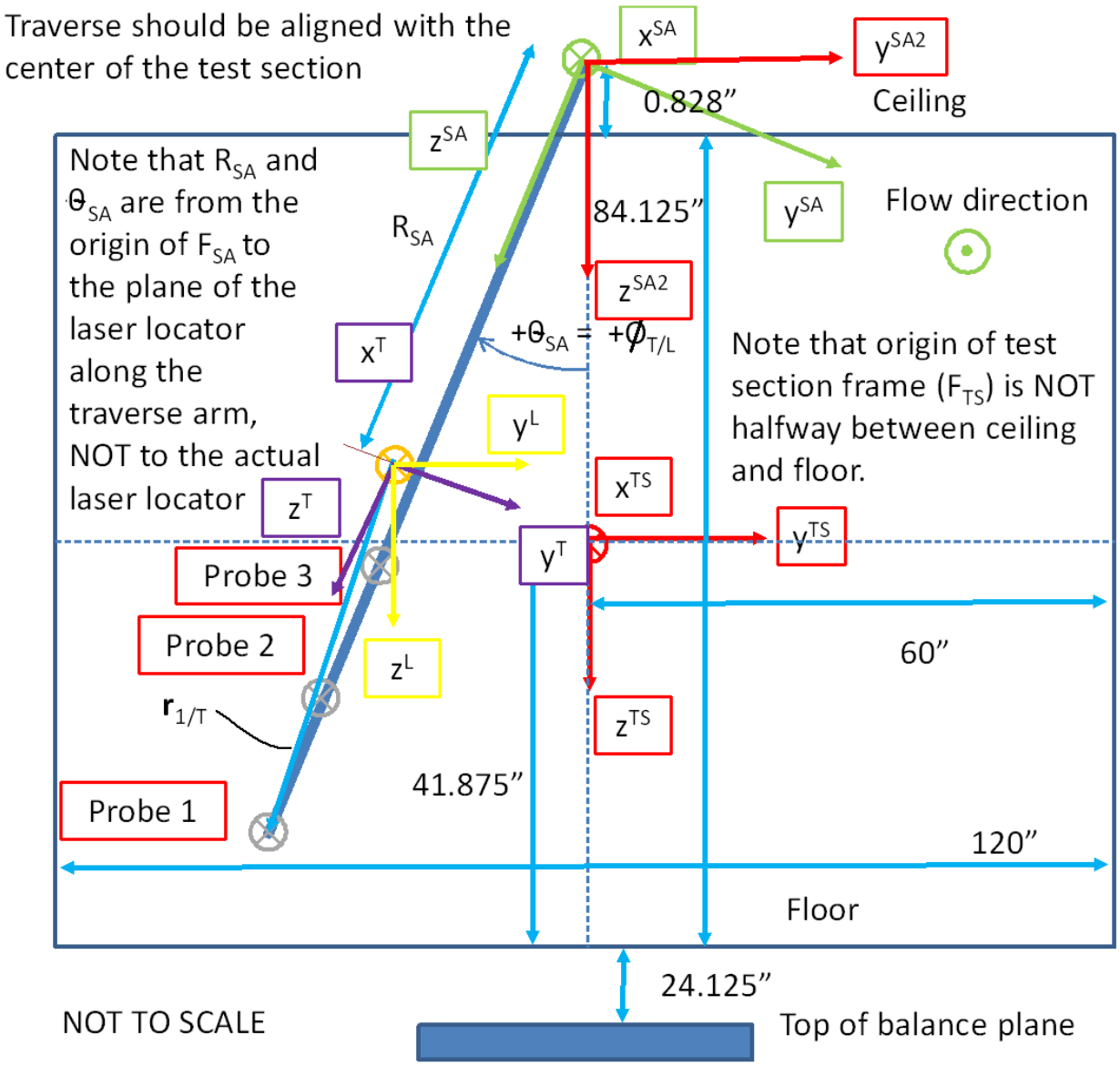

Figure A.2: Coordinate frames associated with the traverse arm. View is from the diffuser looking towards the bellmouth of the test section.

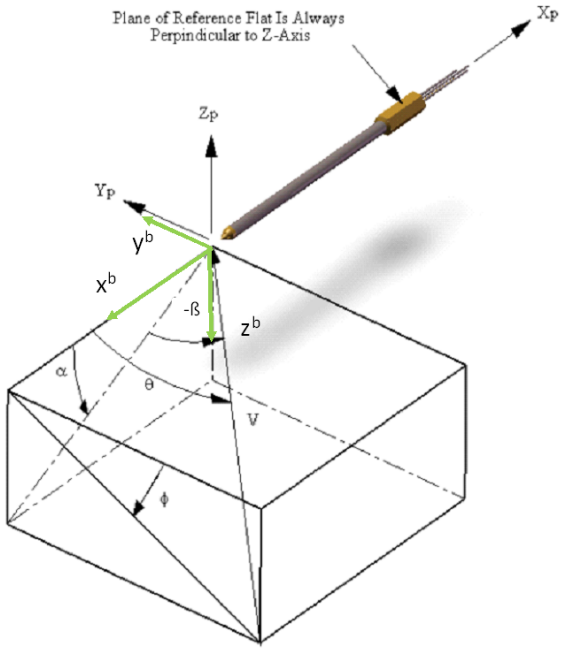

Figure A.3: Coordinate frames associated with the probe. Note that $-\beta$ is shown in the picture.

Figure A.4: Obtaining precise measurements of the location of the tips with respect to the laser locator.

Table A.1: Coordinate frame definitions associated with wake survey system. RHS denotes this axis is creates a right handed coordinate system relative to the other specified axes.

Frame	**Comment**	**Origin**	**+x**	**+y**	**+z**
F_{TS}	Test section frame	Plane of bellmouth and as shown in Fig. A.2	From diffuser to bellmouth	RHS	From ceiling to floor
F_T	Traverse frame	Center of laser locator as shown in Fig. A.7	From probe holder back to front (against flow)	RHS	From laser pointer locator towards bottom of holder
F_L	Laser locator frame	Same origin as F_T	Aligned with x^{TS}	Aligned with y^{TS}	Aligned with z^{TS}
F_{SA}	Swing arm frame	Center of rotation point of swing arm system, shown in Fig. A.2	Aligned with x_T	Aligned with y^T	Aligned with z^T
F_{SA2}	Swing arm frame 2	Same origin as F_{SA}	Aligned with x_{TS}	Aligned with y^{TS}	Aligned with z^{TS}
F_p	Probe frame defined by Aeroprobe	Tip of probe as shown in Fig. A.3	Aligned with probe major axis from front to back	Out right side of probe	Up through top of probe
F_b	Probe frame consistent with flight dynamics conventions	Same origin as F_p	Aligned with probe major axis from back to front	Out right side of probe	Down through bottom of probe

Table A.2: Measured location of probe tips with respect to laser locator as measured by the Leica T-Scan 5.

Probe	x^T **(inches)**	y^T **(inches)**	z^T **(inches)**
1	11.6695	0.7356	10.6766
2	11.7219	0.7293	7.6559
3	11.7040	0.7380	4.6592

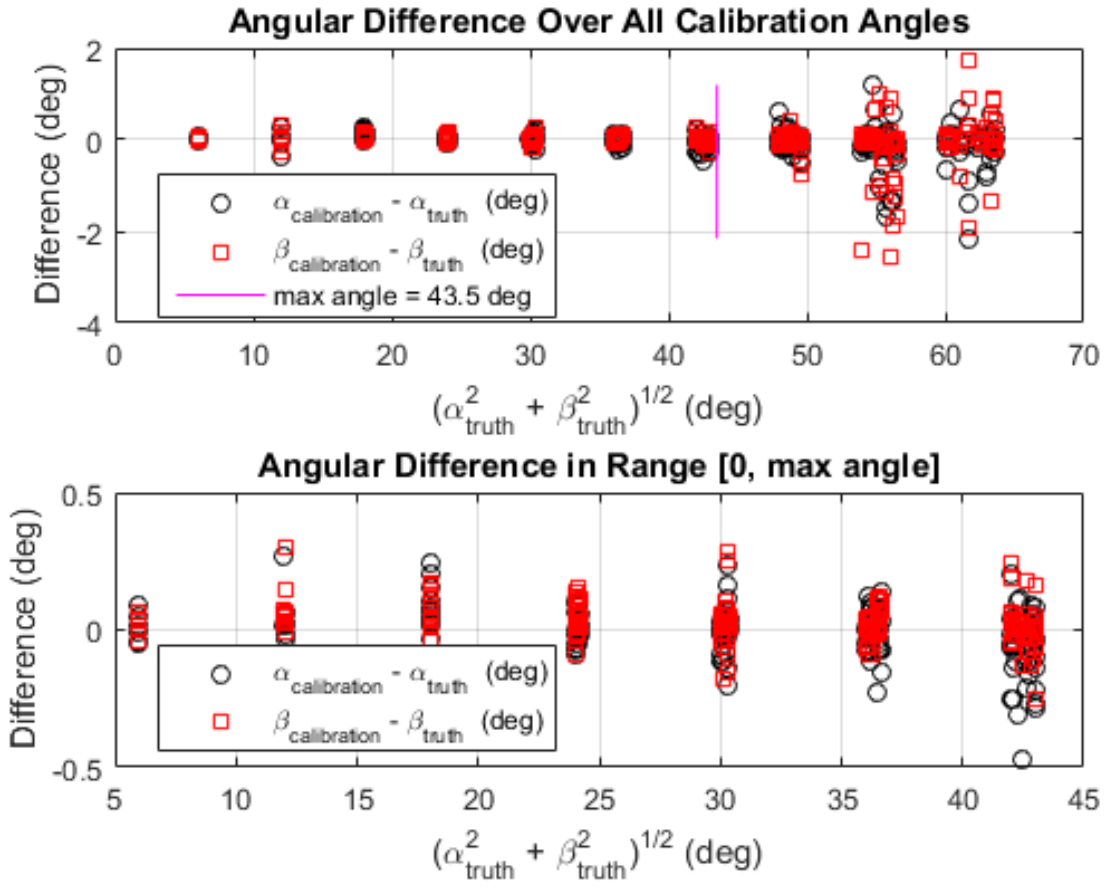

Figure A.5: Difference between calibrated and interpolated angularity for probe 3.

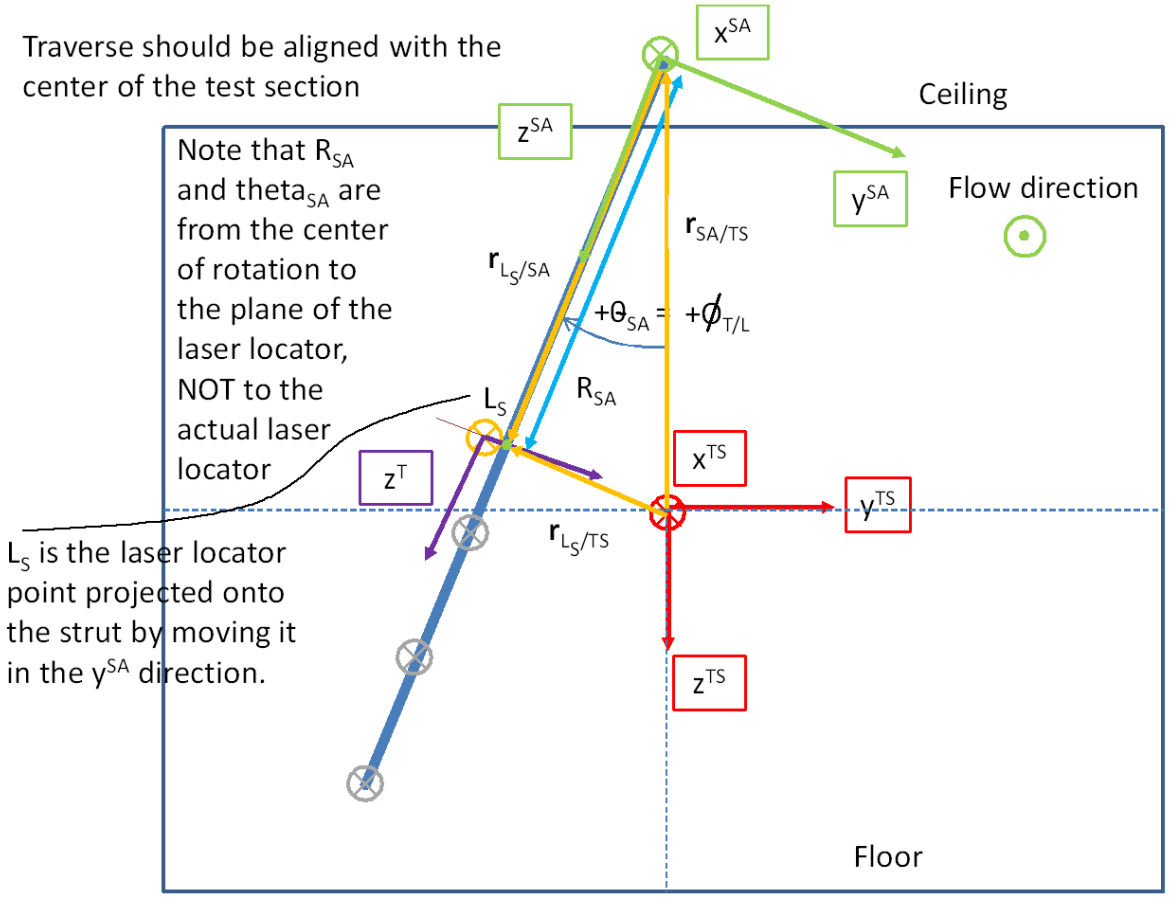

Figure A.6: Note that point L_S is not the location of the laser locator but rather this point projected onto the strut.

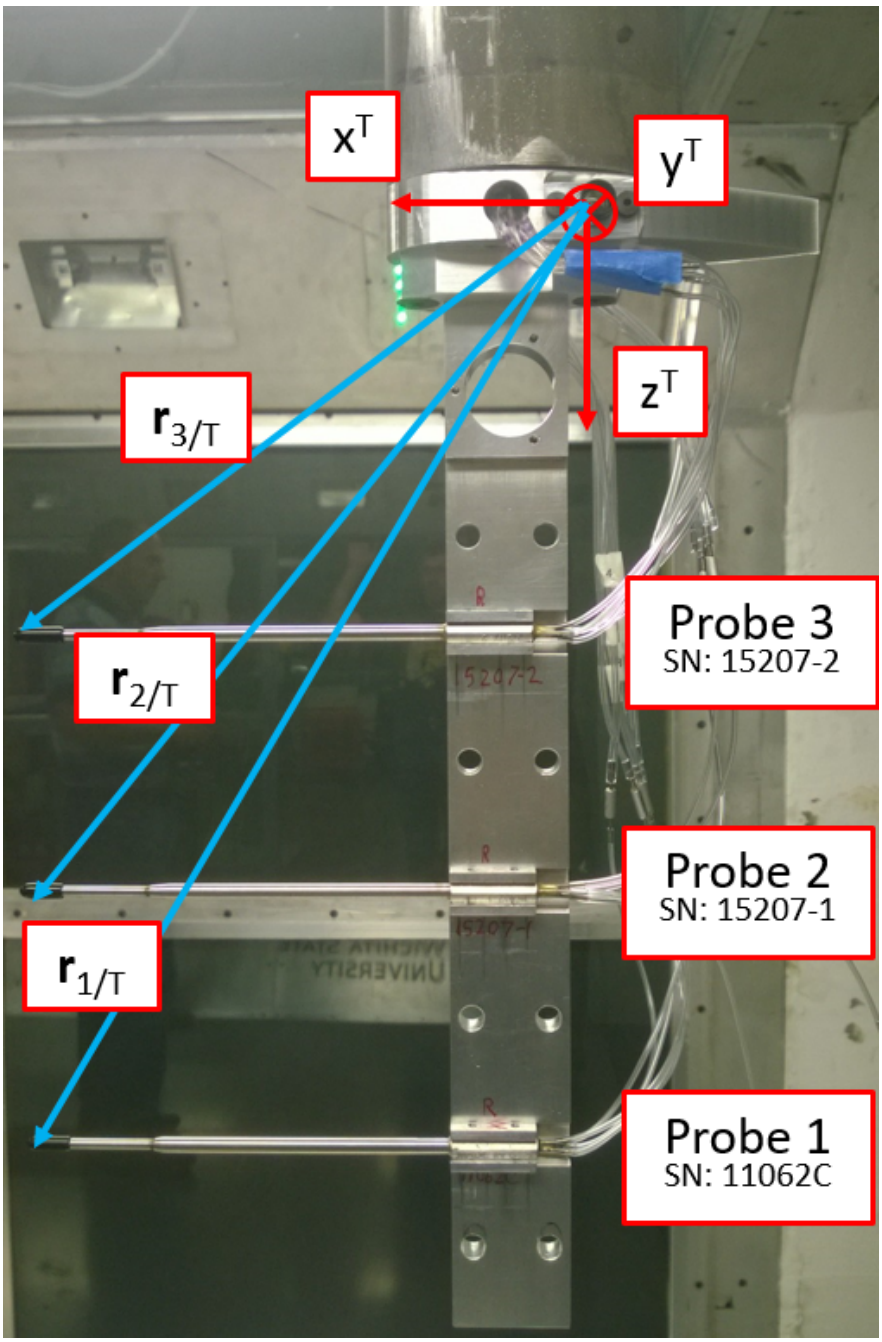

Figure A.7: This image shows the probe numbering scheme used.

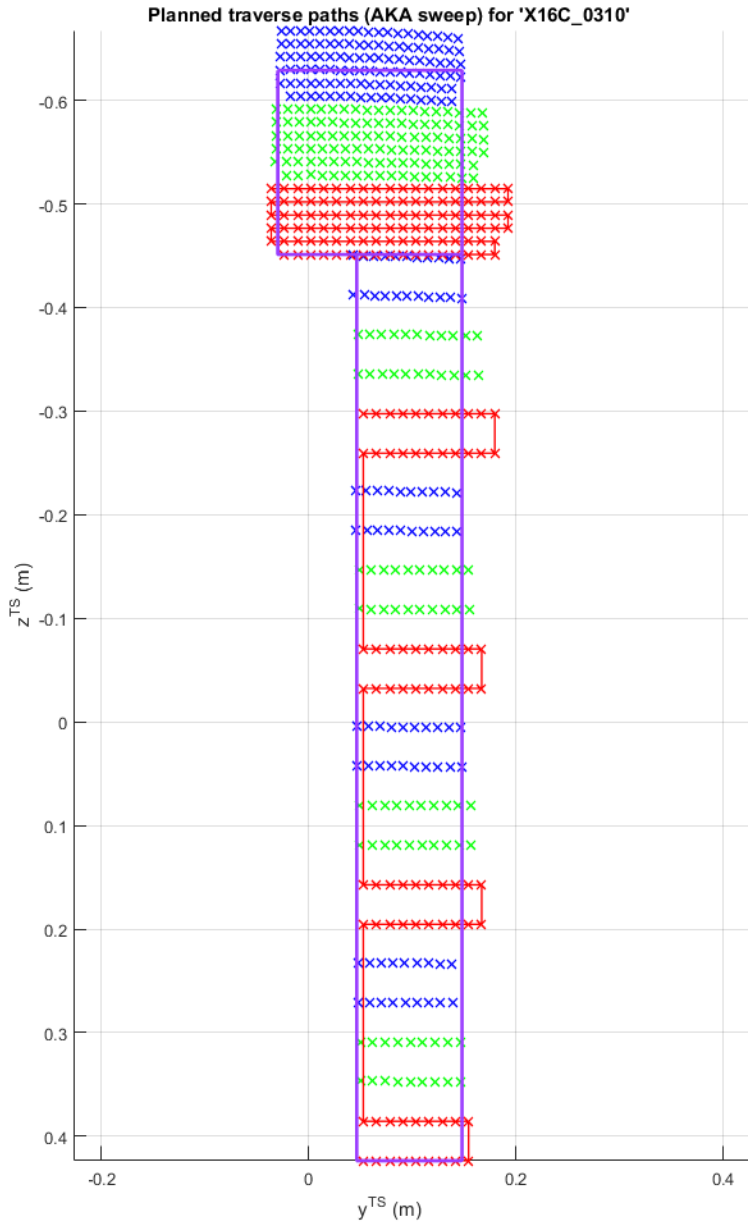

Figure A.8: This image shows the path taken by the 3 probes of the wake survey system to collect data in the wake survey plane.

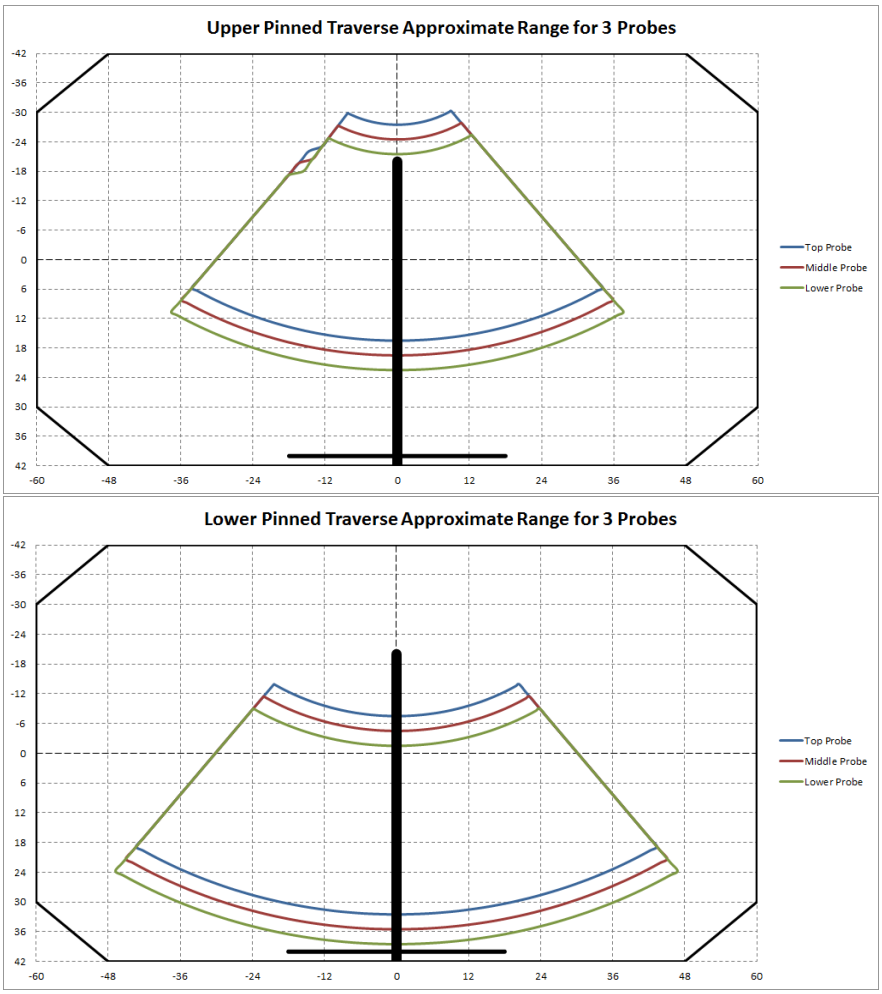

Figure A.9: These images show the coverage of the wake survey probe array in both upper- and lower-pinned configurations.

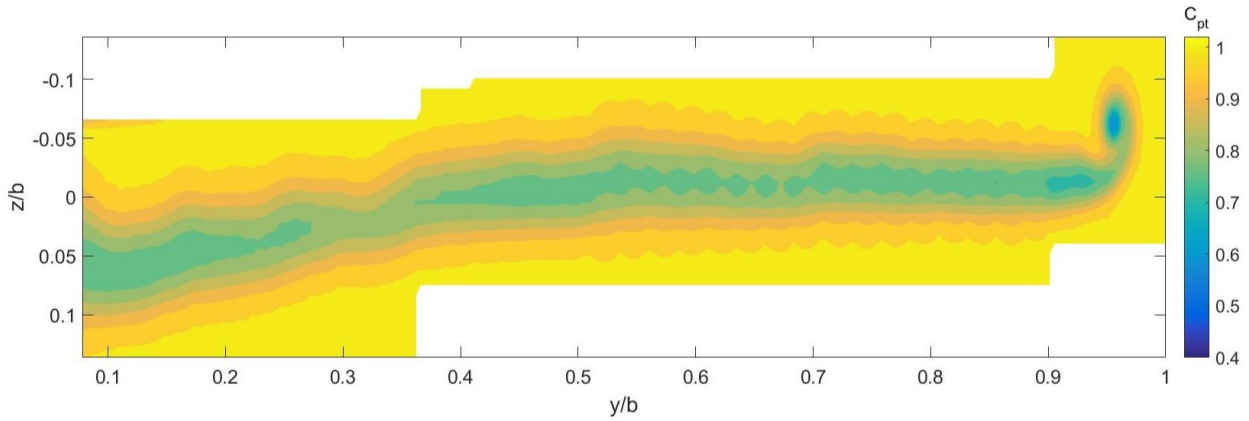

Figure A.10: An example of a contour of C_{pt} before the edge of the wake is found. The configuration shown is the maximum scallop ice shape at $\alpha = 4.27°$, $Re = 1.6 \times 10^6$, and $M = 0.17$. Notice that data is acquired over outside of the border of the wake.

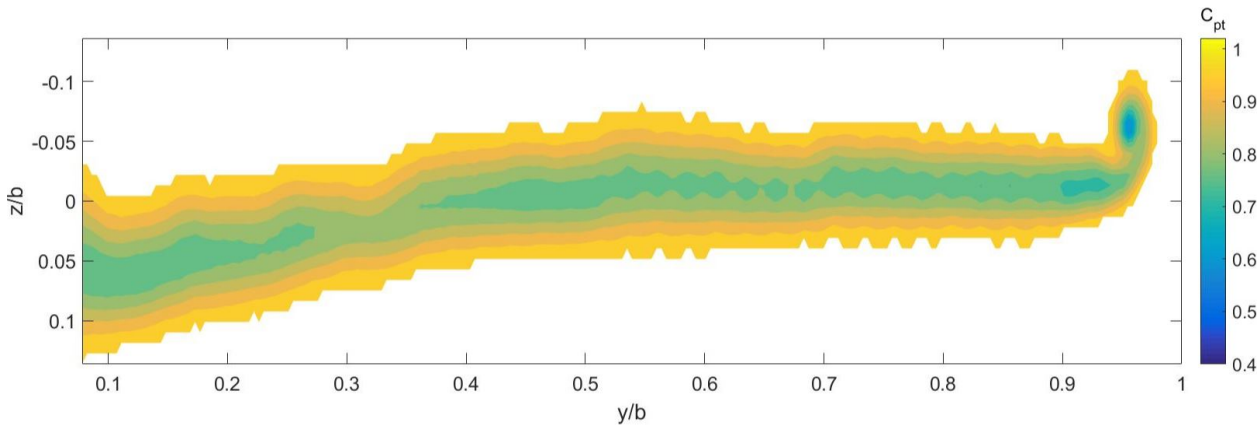

Figure A.11: An example of a contour of C_{pt} after the edge of the wake is found. The configuration shown is the maximum scallop ice shape at $\alpha = 4.27°$, $Re = 1.6 \times 10^6$, and $M = 0.17$.

Appendix B

FAST-RESPONSE FIVE-HOLE PROBE OVERVIEW

One of the recommendations resulting from this study is the use of a fast-response five-hole probe (hereafter referred to as a FR5HP) to account for unsteady effects that occur in the wake of a body. The FR5HP takes similar measurements to a standard-response five-hole probe (Std5HP), but does so at a much higher frequency response. This allows for some analysis into time-dependent phenomena. In this appendix, the advantages of the FR5HP and work done using this probe will be reviewed.

B.1 Five-Hole Probe Theory

A Std5HP measures five pressures at the port locations on its tip at a single point in the flow. An image showing a five-hole probe tip as well as a schematic of the port numbering is shown in Fig. B.1. Using the data reduction technique developed by Treaster and Yocum [50], a relationship between the pressures at each of these ports and different coefficients can be defined

$$C_\alpha = \frac{P_4 - P_5}{P_1 - P_{avg}} \tag{B.1}$$

$$C_\beta = \frac{P_2 - P_3}{P_1 - P_{avg}} \tag{B.2}$$

$$C_{pt} = \frac{P_1 - P_{total}}{P_1 - P_{avg}} \tag{B.3}$$

$$C_{ps} = \frac{P_{avg} - P_{static}}{P_1 - P_{avg}} \tag{B.4}$$

where C_α, C_β, C_{pt}, and C_{ps} are the pitch coefficient, yaw coefficient, total pressure coefficient, and static pressure coefficient, respectively. P_{avg} is the average pressure of ports 2 through 5. A calibration dataset must be used to determine the pitch and yaw coefficients defined in Eq. B.1 and Eq. B.2. The calibration data is then used to determine α, β, C_{pt}, and C_{ps}. The dimensional total and static pressures can be found by rearranging Eqs. B.3 and B.4.

$$P_t = P_1 - C_{pt}(P_1 - P_{avg}) \tag{B.5}$$

$$P_s = P_{avg} - C_{ps}(P_1 - P_{avg}) \tag{B.6}$$

Finally, the total velocity magnitude, V_t, and its components U, V, and W can be found as

$$V_t = \sqrt{\frac{2}{\rho}(P_t - P_s)} \tag{B.7}$$

$$U = V_t \cos(\alpha) \sin(\beta) \tag{B.8}$$

$$V = V_t \sin(\beta) \tag{B.9}$$

$$W = V_t \sin(\alpha) \cos(\beta) \tag{B.10}$$

The equations described in this section allow for a five-hole probe to measure flow accurately over an angular range of $\pm 30°$, thoug using sectoring techniques adapted from seven-hole probe theory, this range can be increased up to approximately $\pm 65°$. This technique is summarized by Diebold [38] and will not be covered here.

B.2 Advantages of the FR5HP

The design of a Std5HP is indicative of its limitations. The orifices on the front of the Std5HP are connected to pressure transducers through a long section of plastic tubing. Due to its length, this tubing has the effect of damping higher frequency pressure fluctuations. These fluctuations are the result of flow turbulence and are thus common. A FR5HP places the high-frequency pressure transducer as close to the probe tips as possible, reducing the amount of tubing and minimizing the damping effect. An image of this difference is shown in Fig. B.2.

Equations A.9 and A.14 were derived under the assumption that turbulent stresses are negligible. In general, though these stresses can be small, they are non-zero. Thus, for a true representation of the aerodynamic forces as derived rom the wake survey, these stresses must be taken into account. Deriving the wake survey equations without neglecting turbulent stresses yields the same equation for lift, but the drag equation becomes

$$D = \iint_W ((P_{t\infty} - \overline{P_t}) + \frac{\rho}{2}(\overline{u} - \overline{u^*})(\overline{u} + \overline{u^*} - 2(U_\infty + \overline{u_b}))) \, dy \, dz + \frac{\rho}{2} \iint_W \overline{\psi\xi} - \iint_W \rho \overline{u'^2} \, dy \, dz \quad \text{(B.11)}$$

where $\overline{u'}$ represents the time-average value of the velocity fluctuation u' and all other variables are now time-averaged as well. This term is called the Reynolds stress term. Note that because the turbulence outside of the wake is ideally zero, the final integral in Eq. B.11 is also an integral over the wake region. Though the lift equation does not change, the effect of turbulence on the vorticity measurement has not been quantified. Given that the vorticity depends on transverse velocity, there is most likely some effect of turbulent velocity fluctuations on the vorticity and by extension the calculated lift.

It should be noted that the use of the wake survey system is not a replacement for a traditional force balance. That is, though improvements can be made in the aerodynamic performance values derived from the wake survey system, the value of the wake survey system lies moreso in the ability to derive spanwise force distributions that cannot be derived from other data collection methods. Capturing high-frequency data in the wake also allows for

some quantitative measure of wake unsteadiness. This allows for further insight into the flow structures that exist on the wing surface.

B.3 Summary of Work Completed and Proposed

To that end, some work has been completed in preparation of using the FR5HP in wake survey studies. Extensive work was done by Diebold [38] to quanitfy the effects of turbulence on a Std5HP using a FR5HP. That study found that turbulence-induced errors for $\overline{C_{pt}}$, $\overline{C_{ps}}$, and $\frac{\overline{U}}{U_\infty}$ were -13%, -25%, and +8%, respectively. It was also found that while errors in $\overline{C_{pt}}$ were increased by axial fluctuations in the flow, errors in $\overline{C_{ps}}$ were not. Errors for both pressure coefficients were decreased by transverse fluctuations.

An extension of Diebold's work was proposed. This extension would examine the unsteadiness and turbulent length scales in the wake of an iced swept wing using a FR5HP. The probe used in this study was a fast-response five-hole probe from Aeroprobe, serial number 14273-1. This probe was used at the University of Washington 3×3 ft. Low Speed Wind Tunnel to develop a procedure to measure turbulent kinetic energy as well as turbulent length scale. This wind tunnel is capable of speeds up to 125 MPH (56 m/s). An image of the probe installed in the wind tunnel is shown in Fig. B.3.

B.4 FR5HP System Specifications and Operation

The probe is connected through a series of wires and small modules to transmit the data collected by the sensors to the data acquisition device. The necessary components for FR5HP use are given in Table B.1. A basic connection diagram is shown in Fig. B.4. Note that a separate power supply is used to provide power to the FR5HP, the Analog Transmission Unit (ATU), and the Inline Interface Module (INT), and that the A/D board receives power from a laptop running the data acquisition software.

The A/D board is an MCC DAQ USB-1808 board capable of producing 18-bit signals. It is an eight-channel (16 single-ended channels) board, capable of sampling up to 50 kilosamples per second per channel simultaneously. As the FR5HP is capable of outputting data at a

rate of approximately 3.5 kHz, the A/D board is more than capable of capturing all of the data output by the probe.

Each pressure port of the FR5HP is conected to an Endevco 8507C piezoresistive pressure transducer, capable of sensing ±1 psig and outputting data at up to 5 kHz maximum, but is generally used in the range of 3 kHz to 3.5 kHz. Note that the input voltage to these transducers is 10V minimum, but 15V to 18V is recommended.

The data-acquisition software was built with MATLAB with the Data Acquisition Toolbox. Note that version 2017a and 2017b are used, as these are the earliest versions that support an input from the USB-1808 board.

Operation of the FR5HP is simple. After connecting all components as per Fig. B.4, 15V is supplied to the ATU, INT, and FR5HP. These components are allowed to warm up for several minutes. Data is output continuously from the FR5HP and is collected as desired from the data acquisition software. Though there are five data channels used for data acquisition from the probe, a sixth channel may be used on the USB-1808 board to act as a trigger channel. This allows for condition-specific triggering of data acquisition.

B.5 Turbulence Calculations

Turbulent length scale and turbulence intensity calculations were done via a procedure described by Camp and Shin [51]. This procedure is summarized here. Take the time-dependent velocity, u, at some point in a flow. The Reynolds decomposition of this velocity is given as

$$u = \overline{u} + u' \tag{B.12}$$

where $\overline{u}$ is the time-averaged velocity at the given point and u' is the velocity fluctuation at that point. The turbulence intensity for a signal with N points is given as the root-mean-square of the velocity fluctuation divided by the time-averaged velocity.

$$T.I. = \frac{\sqrt{\frac{1}{N}\sum_{i=1}^{N}(u_i')^2}}{\overline{u}} \tag{B.13}$$

The turbulent length scale puts a spatial dimension on the turbulent flow. It can considered to be an average of the size of the eddies in the flow and is calculated using the autocorrelation function (ACF) of the velocity signal u. Camp and Shin [51] recommend removing the largest-amplitude parts of frequency spectrum such that the turbulent fluctuations are the only component of the signal being considered.

$$ACF(\tau) = \frac{\frac{1}{\Delta T}\int_0^{\Delta T} u(t)u(t+\tau)dt}{\frac{1}{\Delta T}\int_0^{\Delta T} u^2(t) \quad dt} \tag{B.14}$$

where ΔT is large compared to the period of the lowest frequency component of the signal with significant amplitude and τ is the time lag of the ACF. To calculate the integral length scale, the ACF is integrated.

$$IntegralLengthScale = \overline{u}\int_0^{\infty} ACF(\tau)d\tau \tag{B.15}$$

In practice, based on the Wiener–Khinchin theorem, the power spectrum of the signal can be used to find the ACF, and thus Eq. B.14 is not used. This theorem states that for a well-behaved stationary random process, the Fourier transform of the ACF is equal to the power spectrum. A flowchart showing the data reduction methodology, along with an example signal, is shown in Fig. B.5. This shows an example signal, as well as the removal of the large-amplitude components of the signal, leaving just the turbulent fluctuations. Note that this is a clean exmaple in that there is an obvious, large oscillatory signal with added fluctuations. This is not exemplary of a real-world case and is used as illustration for the data reduction methodology.

B.6 Results from the 3 x 3 Low Speed Tunnel

The 3×3 Low Speed Tunnel at the University of Washington provided some preliminary results for turbulent length scale and turbulence intensity. An image of the FR5HP installed

in the tunnel is shown in Fig. B.3. The results of both turbulent length scale and turbulence intensity versus freestream velocity are shown in Fig. B.6. Turbulent length scale varies from 0.008 m to 0.02 m. Generally, as Re increases, one would expect this length scale to decrease, though this trend is not seen clearly in these results. These results are influenced by the data reduction methodology in that the number of large-amplitude frequencies removed from the original frequency spectrum changes the result. The results shown in Fig. B.6 were calculated by removing the 10 largest-amplitude frequencies. This value was chosen somewhat arbitrarily. Figure B.7 shows that removing frequencies has a large effect on the final answer, but that removing more than the largest five frequencies has a diminishing effect on the final result. The difference between removing 20 amplitudes and 100 amplitudes, for example, shows little change. There are some dynamics lost as the number of frequencies removed increases, thus it is prudent to choose a relatively small value to remove. Therefore, a vlue of 10 frequencies to remove was chosen.

The right plot in Fig. B.6 shows the turbulence intensity as a function of freestream velocity. As u_∞ increases, the turbulence intensity decreases. This makes sense, given that the velocity fluctuations are small while the average velocity will increase with u_∞.

B.7 Recommendations for Future FR5HP Work

The FR5HP will be used to gather data in the wake of a swept wing with simulated leading-edge ice. Several recommendations are made here for that analysis:

1. That data should be reduced in accordance with the procedure given by Camp and Shin [51] to find turbulent length scales in the wake.

2. Some analysis should be done looking into correction of the Std5HP data using data gathered by the FR5HP, including accounting for Reynolds stress and looking into corrections for turbulence effects on the probe.

3. Velocity fluctuations in the wake should be examined to study unsteadiness in the wake.

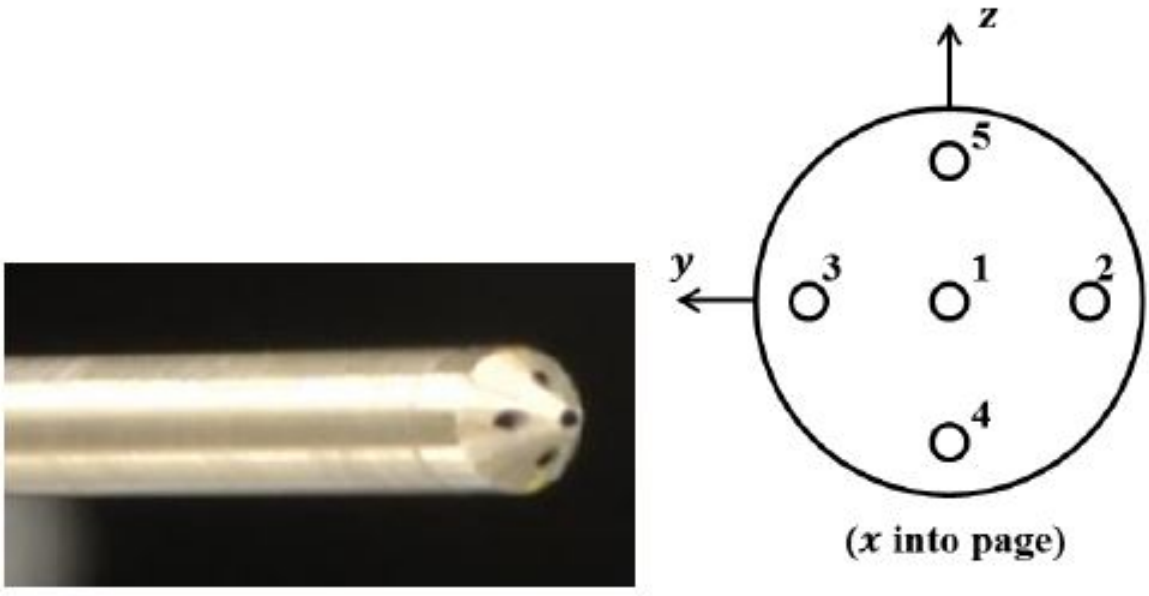

Figure B.1: The tip of a five-hole probe is shown (left) along with a schematic of the tip port numbers (right). Adapted from Diebold [38].

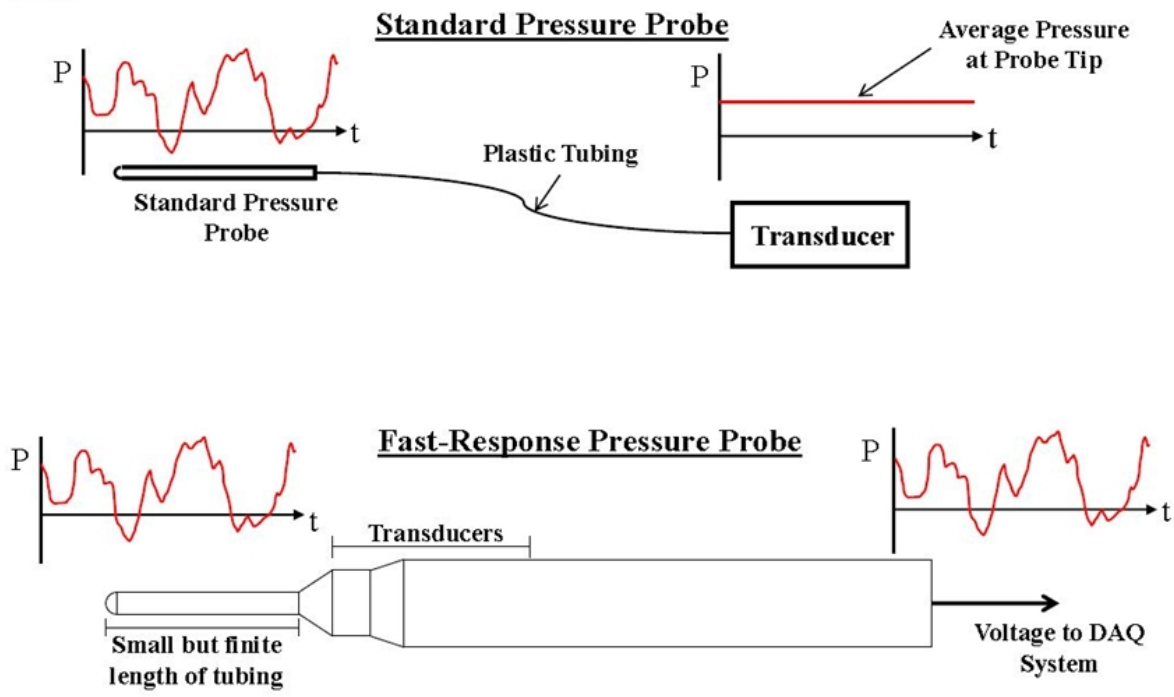

Figure B.2: The differences between a standard-response five-hole probe and a fast-response five-hole probe are shown. Adapted from Diebold [38].

Figure B.3: The FR5HP used in these studies is shown installed in the test sectino of the 3×3 ft. Low Speed Wind Tunnel at the University of Washington.

Table B.1: Parts used to acquire data from the FR5HP.

Part Name	**Serial/Model Number**	**Use**
Fast-Response 5-Hole Probe (FR5HP)	S/N: 14273-1	Acquires time-dependent flow pressures
Analog Transmission Unit (ATU)	S/N: 14273-ATU-1	Boosts signal from FR5HP to travel long distances
Inline Interface Module (INT)	S/N: 14273-INT-1	Rearranges data signals for transmission through a data acquisition system
MCC DAQ A/D Board	M/N: USB-1808	Analog-to-Digital signal conversion board
Signal Splitter	n/a	Splits signals from each pressure sensor to individual wires, transmits power from power supply to FR5HP, ATU, and INT

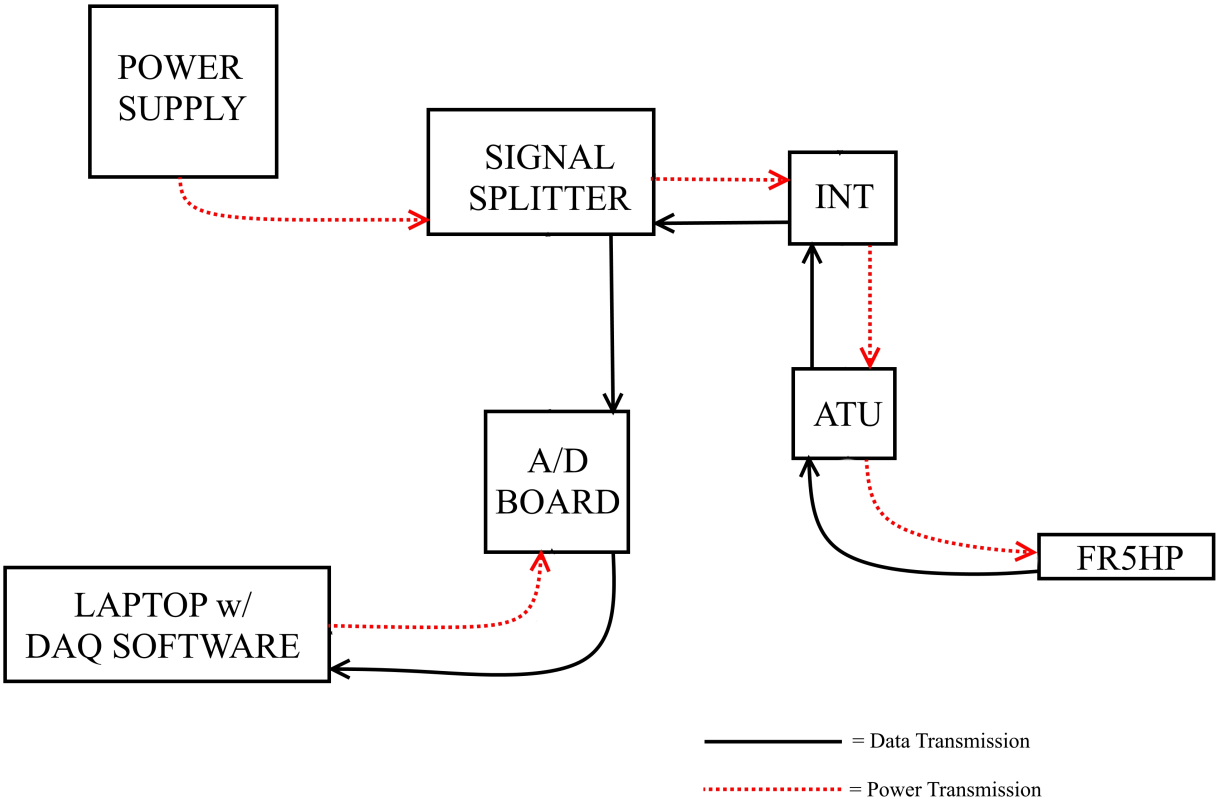

Figure B.4: A connection diagram showing the transmission of power and data through the FR5HP system.

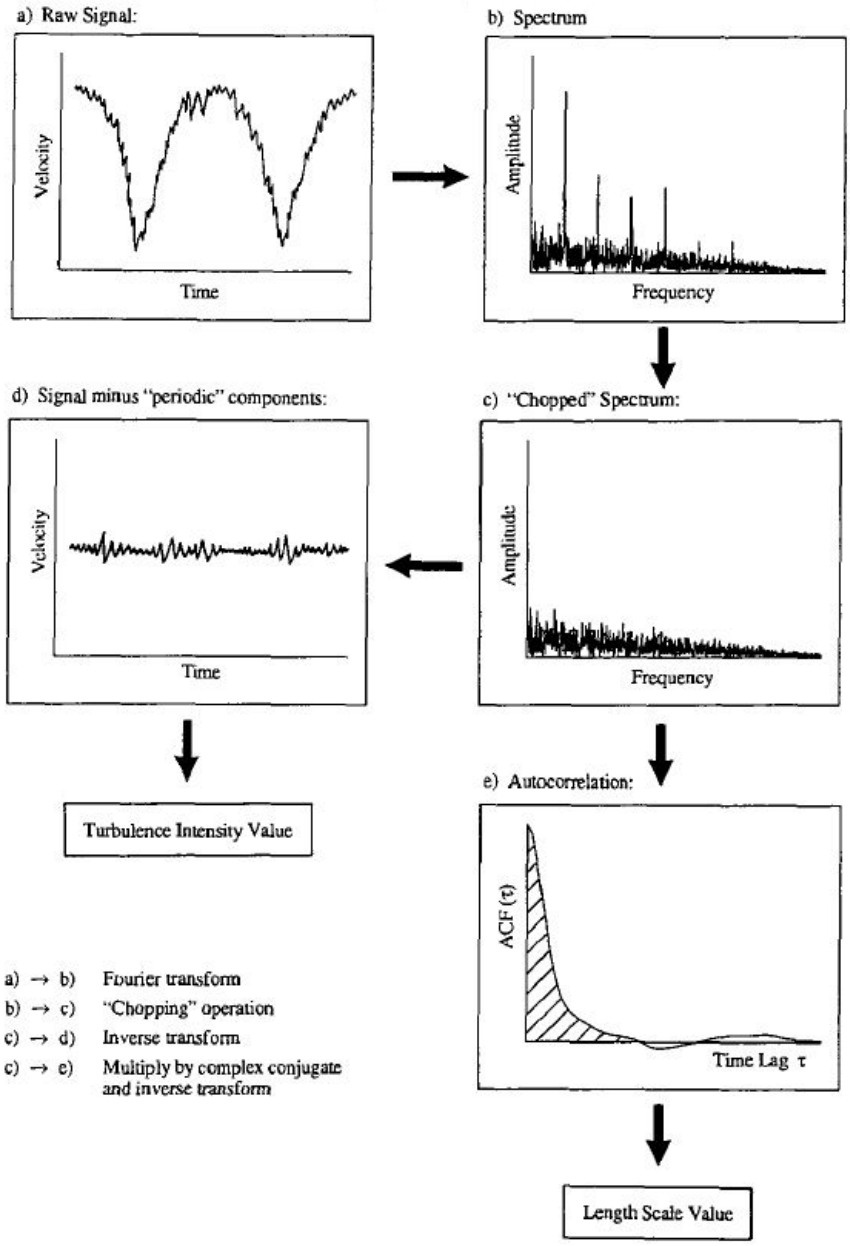

Figure B.5: A flowchart of data reduction to produce turbulent length scale and turbulence intensity is shown. Adapted from [51].

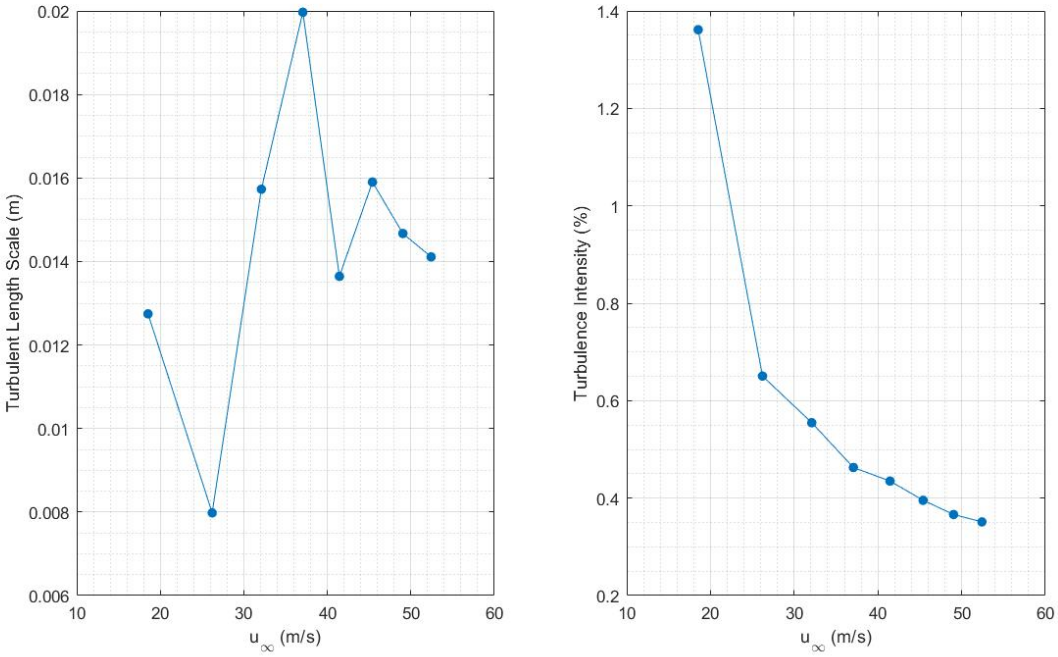

Figure B.6: Turbulent length scale (left) and turbulence intensity (right) as a function of u_∞ are shown for testing done at the Low Speed Wind Tunnel.

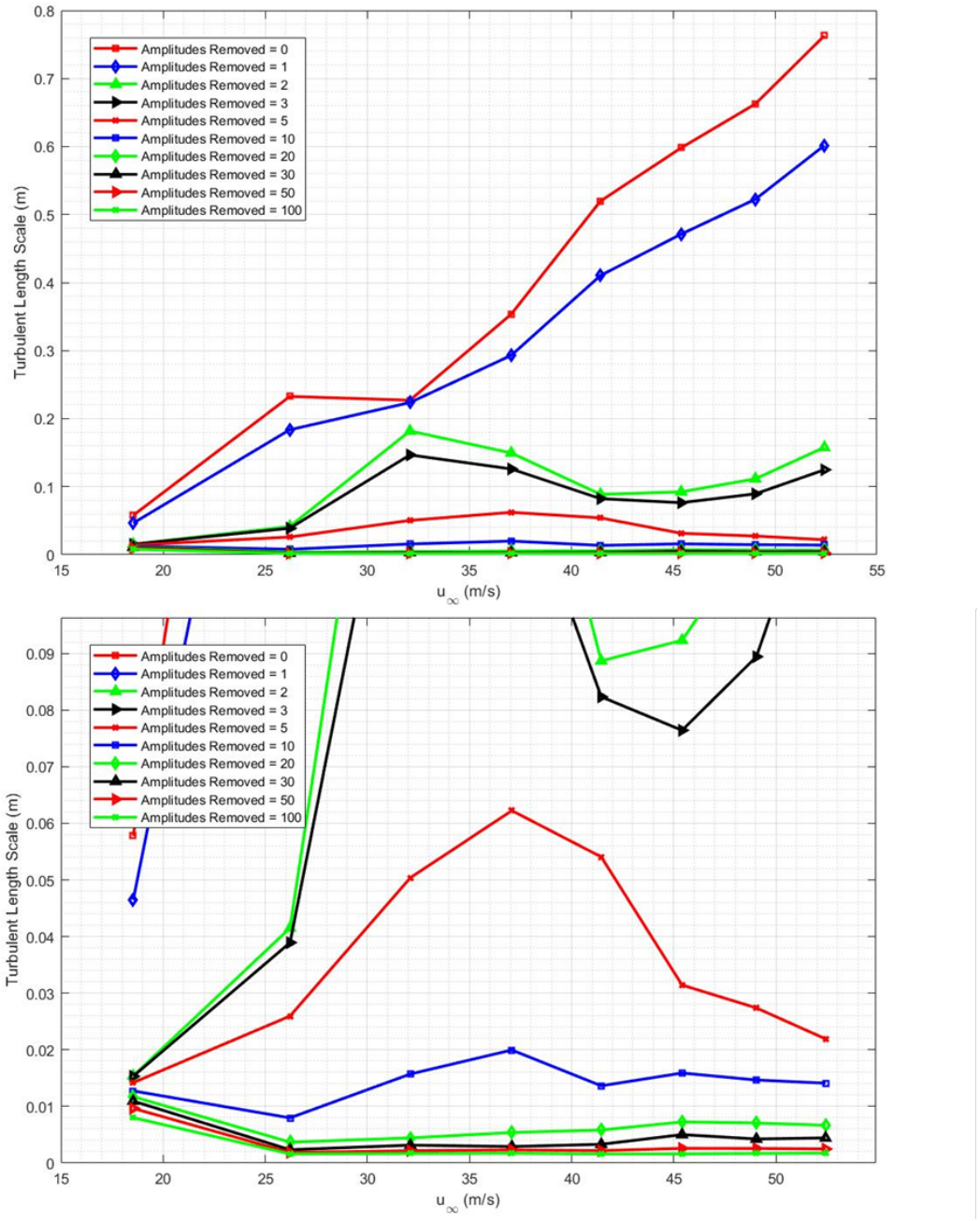

Figure B.7: The change in the turbulent length scale with increasing freestream velocity as a function of number of largest-amplitude frequencies removed.

BIBLIOGRAPHY

[1] Bragg, M. B., Broeren, A. P., and Blumenthal, L. A., "Iced-Airfoil Aerodynamics," *Progress in Aerospace Sciences*, Vol. 41, No. 5, 2005, pp. 323–362.

[2] Lynch, F. T. and Khodadoust, A., "Effects of Ice Accretion on Aircraft Aerodynamics," *Progress in Aerospace Sciences*, Vol. 37, No. 8, 2001, pp. 669–767.

[3] Broeren, A. P., Bragg, M. B., Addy, H. E., Lee, S., Moens, F., and Guffond, D., "Effect of High-Fidelity Ice Accretion Simulations on the Performance of a Full-Scale Airfoil Model," AIAA Paper 2008-434.

[4] Papadakis, M., Yeong, H.-W., Wong, S.-C., Vargas, M., and Potapczuk, M., "Aerodynamic Performance of a Swept Wing with Ice Accretions," *Proceedings of the 41st AIAA Aerospace Sciences Meeting and Exhibit*, Reno, NV, 2003.

[5] Papadakis, M., Yeong, H.-W., and Wong, S.-C., "Aerodynamic Performance of a Swept Wing with Simulated Ice Shapes," *Proceedings of the 42nd AIAA Aerospace Sciences Meeting and Exhibit*, 2004.

[6] Kerho, M. F., Bragg, M. B., and Khodadoust, A., "LDV Flowfield Measurements on a Straight and Swept Wing with a Simulated Ice Accretion," *AIAA Paper 93-0300*, 1993.

[7] Broeren, A. P., Potapczuk, M. G., Riley, J. T., Villedieu, P., Moens, F., and Bragg, M. B., "Swept-Wing Ice Accretion Characterization and Aerodynamics," *Proceedings of the 5th AIAA Atmospheric and Space Environments Conference*, San Diego, CA, June 2013.

[8] Broeren, A. P., Woodard, B. S., Diebold, J. M., and Moens, F., "Low-Reynolds Number Aerodynamics of an 8.9% Scale Semispan Swept Wing for Assessment of Icing Effects," *Proceedings of the 9th AIAA Atmospheric and Space Environments Conference*, Denver, CO, June 2017.

[9] Diebold, J. M., Monastero, M. C., and Bragg, M. B., "Aerodynamics of a Swept Wing with Ice Accretion at Low Reynolds Number," *Proceedings of the 30th AIAA Applied Aerodynamics Conference*, New Orleans, LA, June 2012.

[10] Anderson, J. D., *Introduction to Flight*, McGraw-Hill Education, 2011, pp. 381–393.

[11] Furlong, G. C. and Mchugh, J. G., "A summary and analysis of the low-speed longitudinal characteristics of swept wings at high Reynolds number," Tech. rep., NACA-TR-1339, 1957.

[12] McCullough, G. B. and Gault, D. E., "Examples of Three Representative Types of Airfoil-Section Stall At Low Speed," Tech. rep., 1951.

[13] Harper, C. W. and Maki, R. L., "A Review of the Stall Characteristics of Swept Wings," Tech. rep., 1964.

[14] Poll, D. I. A., "Spiral Vortex Flow Over a Swept-back Wing," *The Aeronautical Journal*, Vol. 90, No. 895, May 1986, pp. 185–199.

[15] Wright, W. B., *Users Manual for the Improve NASA Lewice Ice Accretion Code LEWICE3 Version 2.0*, NASA Glenn Research Center, nasa cr 1999-209409 ed., September 1999.

[16] Busch, G. T., Broeren, A. P., and Bragg, M. B., "Aerodynamic Simulation of a Horn-Ice Accretion on a Subscale Model," *Journal of Aircraft*, Vol. 45, No. 2, March 2008, pp. 604–613.

[17] Brumby, R. E., "Wing surface roughness–cause & effect," *D.C. Flight Approach*, Jan. 1979, pp. 2–7.

[18] Bowden, D. T., "Effect on pneumatic De-icers and ice formations on aerodynamic characteristics of an airfoil," Tech. rep., NACA TN 3564, Feb. 1954.

[19] Lee, S. and Bragg, M. B., "Investigation of Factors Affecting Iced-Airfoil Aerodynamics," *Journal of Aircraft*, Vol. 40, No. 3, June 2003, pp. pp. 499–508.

[20] Broeren, A. P., Addy, H. E., and Bragg, M. B., "Effect of Intercycle Ice Accretions on Airfoil Performance," *AIAA-2002-0240*, 2002.

[21] Bragg, M. B., Kerho, M. F., and Khodadoust, A., "Aerodynamics of a finite wing with simulated ice," *Proceedings of the 5th Symposium on Numerical and Physical Aspects of Aerodynamic Flows*, California State University at Long Beach, Jan. 1992.

[22] Camello, S. C., Lee, S., Lum, C. W., and Bragg, M. B., "Generation of Fullspan Leading-Edge 3D Ice Shapes for Swept-Wing Aerodynamic Testing," *Proceedings of the 8th AIAA Atmospheric and Space Environments Conference*, June 2016.

[23] Camello, S. C., *Effect of Ice Accretion Simulation Fidelity on Low-Reynolds Number Swept-Wing Aerodynamic Performance*, Master's thesis, University of Washington, Seattle, WA, 2017.

[24] Anderson, D. N., "Manual of Scaling Methods," Tech. rep., NASA CR-2004-21287, 2004.

[25] Fujiwara, G. E., Wiberg, B. D., Woodard, B. S., and Bragg, M. B., "3D Swept Hybrid Wing Design Method for Icing Wind Tunnel Tests," *Proceedings of the 6th AIAA Atmospheric and Space Environments Conference*, 2014.

[26] Lee, S., Broeren, A. P., Addy, H. E., Sills, R., and Pifer, E., "Development of 3D Ice Accretion Measurement Method," *Proceedings of the AIAA 4th Atmospheric and Space Environments Conference*, New Orleans, LA, June 2012.

[27] Woodard, B. S., Broeren, A. P., Diebold, J. M., and Bragg, M. B., "Preliminary Testing of Low-Reynolds Number Aerodynamics for a Swept Wing with Artificial Ice Roughness," Tech. rep., DOT/FAA/TC-17/48, 2017.

[28] Fujiwara, G. E. C., Bragg, M. B., Camello, S., and Lum, C. W., "Computational and Experimental Ice Accretions of Large Swept Wings in the Icing Research Tunnel," *Proceedings of the 8th AIAA Atmospheric and Space Environments Conference*, June 2016.

[29] Irani, E. and Laffen, J., "Lessons Learned during Recent Upgrade: The Rejuvenation of the Wichita State University's Walter H. Beech 7x10 foot Low Speed Wind Tunnel at the National Institute for Aviation Research," *AIAA Paper 2010-1487*, Orlando, FL, Jan. 2010.

[30] *Low-Speed Wind Tunnel Testing*, John Wiley & Sons, Inc., New York NY, 3rd ed., 1999.

[31] "Data Reduction System: Boundary Corrections," Walter H. Beech Memorial Wind Tunnel Engineering Process Description.

[32] Vassberg, J. C., DeHaan, M. A., Rivers, S. M., and Wahls, R. A., "Development of a Common Research Model for Applied CFD Validation Studies," *Proceedings of the 26th AIAA Applied Aerodynamics Conference*, Honolulu, HI, August 2008.

[33] Rivers, M. and Dittberner, A., "Experimental Investigation of the NASA Common Research Model," AIAA Paper 2010-4218, June 2010.

[34] Somos® Material Group, DSM Functional Materials, Elgin, IL, *Somos® NeXt*.

[35] Betz, A., "A Method for the Direct Determination of Wing-Section Drag," Tech. rep., 1925.

[36] Maskell, E., "Progress Towards a Method for the Measurement of the Components of the Drag of a Wing of Finite Span," Tech. rep., 1972.

[37] Diebold, J. M., *Aerodynamics of a Swept Wing with Leading-Edge Ice at Low Reynolds Number*, Master's thesis, University of Illinois at Urbana-Champaign, Urbana, Illinois, 2012.

[38] Diebold, J. M., *The Effects of Turbulence on the Measurements of Five-Hole Probes*, Ph.D. thesis, University of Illinois at Urbana-Champaign, Urbana, IL, 2017.

[39] Coleman, H. W. and Steele, W. G., *Experimentation and Uncertainty Analysis for Engineers*, Wiley-Interscience, 1989, pp. 40–118.

[40] Kline, S. and McClintock, F. A., "Describing Uncertainties in Single Sample Experiments," *Mechanical Engineering*, Vol. 75, No. 1, 1953, pp. 3–8.

[41] Lum, C. W., Diebold, J. M., Woodard, B. S., Sandhu, N., and Bragg, M. B., "The Application of a Five-Hole Probe Wake-Survey Technique to the Study of Swept Wing Icing Aerodynamics," *Proceedings of the 9th Atmospheric and Space Environments Conference*, Denver, CO, June 2017.

[42] Broeren, A. P., Lee, S., Woodard, B. S., Lum, C. W., and Smith, T. G., "Independent Effects of Reynolds and Mach Numbers on the Aerodynamics of an Iced Swept Wing," *Proceedings of the 10th AIAA Atmospheric and Space Environments Conference*, Atlanta, GA, June 2018.

[43] Lee, S., Broeren, A. P., Woodard, B. S., Lum, C. W., and Smith, T. G., "Comparison of Iced Aerodynamic Measurements on Swept Wing from Two Wind Tunnels," *Proceedings of the 10th AIAA Atmospheric and Space Environments Conference*, Atlanta, GA, June 2018.

[44] Camello, S. C., Bragg, M. B., Broeren, A. P., Lum, C. W., Woodard, B. S., and Lee, S., "Effect of Ice Shape Fidelity on Swept-Wing Aerodynamic Performance," *Proceedings of the 9th AIAA Atmospheric and Space Environments Conference*, Denver, CO, June 2017.

[45] Diebold, J. M. and Bragg, M. B., "Study of a Swept Wing with Leading-Edge Ice Using a Wake Survey Technique," *Proceedings of the 51st AIAA Aerospace Sciences Meeting*, Grapevine, TX, January 2013.

[46] Stevens, B. L. and Lewis, F. L., *Aircraft Control and Simulation*, John Wiley and Sons, Hoboken, NJ, 2nd ed., 2003.

[47] "Leica T-Scan 5," http://metrology.leica-geosystems.com/en/Leica-T-Scan-5_105434.htm, 2016, Online, accessed October 10, 2016.

[48] Aeroprobe Corporation, "Multi-hole Probes User Manual, Document Number 90001-02-UMN-02, Revision C," Tech. rep., Wichita State University, 2015.

[49] "Leica Absolute Tracker AT901," http://www.leica-geosystems.no/no/Leica-Absolute-Tracker-AT901_69047.htm, 2016, Online, accessed October 10, 2016.

[50] Treaser, A. L. and Yocum, A. M., "The Calibration and Application of Five-Hole Probes," Tech. Rep. Technical Memorandum 78-10, Naval Sea Systems Command, 1978.

[51] Camp, T. R. and Shin, H. W., "Turbulence Intensity and Length Scale Measurements in Multistage Compressors," *International Gas Turbine and Aeroengine Congress and Exposition*, ASME, The Hague, NL, June 1994.